Univ.-Prof. Dr. Gerald Badurek

TECHNISCHE UNIVERSITÄT WIEN
Vienna University of Technology

DIPLOMARBEIT

Parameter selective MR-micro-imaging of biomaterials with short T2-times using UTE pulse sequences

ausgeführt am

Zentrum für Medizinische Physik und Biomedizinische Technik
der Medizinischen Universität Wien

und

Atominstitut der Technischen Universität Wien

unter der Anleitung von

Ao. Univ.-Prof. Dr. Andreas Berg
Univ.-Prof. Dr. Gerald Badurek

durch

Christian Horn, B.Sc.
Schöffelgasse 16/4
A-1180 Wien

Wien, 2012

Kurzfassung

Die direkte Visualisierung von Substanzen mit kurzen T2-Zeiten (z.B. Plastik, Zähne) ist mit Standard Magnetresonanz (MR)-Bildgebung kaum möglich, da das Messsignal innerhalb der Detektionszeit größtenteils zerfallen ist. Das Absorptionsspektrum solcher Substanzen ist wesentlich breiter als das von Materialen mit langer T2-Zeit, was sich in einer hohen Empfindlichkeit gegenüber off-resonanter Anregung niederschlägt.

In dieser Arbeit wurde eine MR-Pulssequenz entwickelt, die auf einer existierenden Sequenz für ultrakurze Detektionszeiten (Ultra-short echo time, UTE) basiert, und mit einem off-resonanten Magnetisierungstransfer (MT) Sättigungspuls kombiniert. UTE-Pulssequenzen sind noch im Erprobungsstadium, aber die Kombination mit MT-Wichtung ist neu und verspricht einen neuartigen Bildkontrast in der Visualisierung von Hartsubstanzen.

Die Implementierung wurde an einem speziellen MR-Mikrogradientensystem realisiert, welches Teil eines Hochfeld-MR-Scanners ist. Verschiedene Teststrukturen (Phantome) und biomedizinische Proben (Sehnen, Bänder etc.) wurden unter Verwendung einer 3-dim. UTE-Sequenz mit radialer k-Raum-Abtastung untersucht. Durch einen frei konfigurierbaren, vorgeschalteten Sättigungspuls kann ein MT-Kontrast erreicht werden. Die tatsächliche Sequenz-Leistungsfähigkeit wird durch eine Reihe von Qualitätskontrollmessungen eruiert, darunter Messungen bezüglich Bildunschärfe, Auflösungsvermögen, Kantenanhebungsartefakten und MT-Kontrast-Fähigkeiten.

Durch ihre kurzen Detektionszeiten ($\mathrm{TE}_{min} = 70\,\mu\mathrm{s}$), erlaubt die UTE-Sequenz die Visualisierung von Substanzen, die für konventionelle Pulssequenzen “unsichtbar” sind. Allerdings zeigt sich auch eine große Empfindlichkeit gegenüber imperfekter Gradientenleistung. Insbesondere zeitliche Ungenauigkeiten im Schaltverhalten äußern sich in Bildartefakten in Form von Kantenanhebungen, die aus Frequenzverschiebungen des Profilsignals resultieren. Diese konnten durch den Einsatz von Korrekturwerten während der Bildrekonstruktion minimiert werden. Durch Vergleichsmessungen mit Standardsequenzen konnte eine plausible Wirksamkeit des MT-Kontrastes in der UTE-Sequenz nachgewiesen werden. Außerdem werden erste vorläufige Ergebnisse präsentiert, die einige neue Perspektiven und mögliche Anwendungen demonstrieren sollen.

Die Kombination der UTE-Sequenz mit MT-Wichtung bietet einen zusätzlichen Kontrastmechanismus innerhalb von Geweben und Materialen mit sehr kurzen T2-Zeiten. Allerdings ist das räumliche Auflösungsvermögen gegenüber Standardsequenzen stark eingeschränkt. Außerdem weist der UTE-Bildgebungsteil spezifische Bildartefakte auf, die auf zeitliche Verzögerungen im Gradientenschaltverhalten zurückzuführen sind.

Abstract

Du to a rapid decay of the magnetic resonance (MR) signal within the detection time frame, the direct visualisation of short-T2 materials (e. g. plastics, tendons, ligaments, dental tissues) is barely achievable. There absorption line shapes are much broader than long-T2 materials resulting in a great sensitivity to off-resonance excitations.

Within this thesis, a new MR-pulse sequence, based on an existing sequence using ultrashort detection times (UTE), was developed in combination with magnetisation transfer (MT) contrast featuring high-power off-resonant saturation pulses. UTE-pulse-sequences are still in an experimental stage, but the new combination with MT-weighting promise a novel image contrast visualising solid materials.

The implementation was done on a specific microimaging system installed at a high-field human MR scanner. Various phantoms and biomedical samples containing short-T2 tissues (tendons, ligaments etc.) were investigated using a 3-dimensional UTE sequence with radial k-space sampling. MT-contrast could be achieved by a preceding, fully adjustable saturation pulse. In order to evaluate the sequence performance, quality control measurements were performed regarding image blurring, edge enhancement, spatial resolution and MT-contrast capabilities.

With its short detection time ($TE_{min} = 70\,\mu s$), the UTE sequence allows the visualisation of materials remaining "invisible" by conventional MR-imaging. However, it also showed a distinct liability to imperfect gradient performance. In particular switching delays lead to edge enhancement artefacts, which are due to signal frequency shifting. This limitation could be minimised by correction terms during image reconstruction. The plausible effectiveness of MT-contrast along with the UTE sequence was verified by comparing the MT-weighted images of standard sequences to the MT-weighing in UTE-sequences. Moreover, first preliminary results are presented in order to demonstrate some perspectives and future applications.

The combination of UTE imaging and MT pulse technique provides an additional contrast within tissues with very short T2s, but the spatial resolution is highly limited compared to standard sequences. Moreover, the currently available UTE imaging part exhibits specific artefacts caused by an imperfect gradient timing performance.

Contents

Chapter 1

Introduction

Magnetic Resonance Imaging (MRI) provides a versatile tool for non-invasive investigations on the internal structure of living subjects and ex-vivo samples. Therefore it became an integral part of biomedical and actual clinical imaging today. MRI is based on the principles of nuclear magnetic resonance (NMR), which is in fact a spectroscopic technique.

Although the range of materials which can be visualised is quite large, it is anyhow limited for standard methods. The composition and morphological structure of semi-solid tissue components or implants (e.g. cornea, dermis, calcified cartilage, horn substance, teeth and plastics) cannot be imaged by standard MR methods, since the mobility of signalling molecules is highly reduced. This in turn results in a strong MR signal (line) broadening and a significant reduction of T2 times ($< 1\,\text{ms}$). Using standard pulse sequences (with detection times down to 7 ms to 10 ms), a rapid decay of the MR signal occurs making a detection nearly impossible. This tissue dependent restriction requires the application of special pulse sequences designed for the detection of ultra-short echo times (UTE). Thus, UTE imaging gives a direct access to investigations on materials and tissues which were formerly measurable only through indirect MR techniques or x-ray imaging. (cf. Robson et al., 2003).

One of this indirect MR techniques assessing motional restricted protons is the so called magnetization transfer (MT) imaging. MT imaging is clinically more established because

it is readily available on clinical scanners. MT is based on the polarisation transfer via dipolar coupling and chemical exchange between a pool of bound protons and the mobile protons associated to the tissue water (cf. Henkelman et al., 2001).

Until now, pulse sequences for very short detection times were only available on special MR microscopy systems or within research on human MR scanners with reduced spatial resolution. This thesis presents first images acquired by a specifically modified UTE pulse sequence with and without integrated MT contrast on a custom designed MR-microimaging insert for a 7T human scanner providing an additional tissue contrast.

Part I.

Theoretical Background

Chapter 2

Basic Principles of Nuclear Magnetic Resonance

This chapter gives a brief overview of the fundamental principals of nuclear magnetic resonance (NMR), which is the basis of MR imaging. The physical phenomenon NMR was independently discovered by F. Bloch and E.M. Purcell in 1946* (McRobbie et al., 2007). A much more detailed discussion can be found in lots of textbooks. The following chapter is primary based on Badurek (2010), Kuperman (2000) and de Graaf (2007).

2.1. A Short Quantum Mechanical Introduction

The phenomenon of NMR is based on the magnetic properties of atomic nuclei. These properties are related to the nuclear spin, or total angular momentum $\vec{I}$, which is the sum of the spins and orbital angular momenta of the constituent protons and neutrons. Since nuclei with an odd mass- or atomic number (i. e. an odd number of protons and/or neutrons) have a non-zero net nuclear spin, only this nuclei are accessible for NMR investigations. The nuclear spin is quantized by

$$|\vec{I}| = \hbar\sqrt{I(I+1)}, \tag{2.1}$$

* shared Nobel Prize in 1952

Nucleus	Spin I [$\hbar$]	$\frac{\gamma}{2\pi}$[MHz T^{-1}]
^{1}H	$1/2$	42.57
^{23}Na	$3/2$	11.26
^{31}P	$1/2$	17.23

Table 2.1.: Some nuclei with their spin and gyromagnetic ratio commonly used in biomedicine (Allison, 2006).

while the spin quantum number I has integral or half-integer discrete values:

$$I = 0, \frac{1}{2}, 1, \frac{3}{2}, 2, \dots \ . \tag{2.2}$$

Descriptively expressed, a rotating charge (or spinning nucleus) corresponds to a magnetic moment

$$\vec{\mu} = \gamma \vec{I} \, , \tag{2.3}$$

where γ is a specific, constant value and is called the gyromagnetic ratio. It is defined as the product of the nucleus' g-factor and the nuclear magneton μ_N in terms of the reduced Planck constant:

$$\gamma = \frac{g \cdot \mu_N}{\hbar} \ . \tag{2.4}$$

The gyromagnetic ratio for some nuclei commonly used in biomedicine is shown in Table 2.1. In an external magnetic field $\vec{B}_0 = (0, 0, B_0)$ the nuclear spin, or magnetic moment respectively, are only able to take discrete orientations relatively to $\vec{B}_0$. The number of discrete positions in an external magnetic field is governed by the given spin quantum number I and can be expressed by an additional quantum number

$$m_z = I, I-1, I-2, \dots, -I \qquad \text{and} \qquad I_z = m_z \hbar \, , \tag{2.5}$$

which results in $2I + 1$ possible values. For example, a spin-$1/2$ isotope like the hydrogen nucleus (^1_1H) has two orientations $m_z = \pm\frac{1}{2}$. In this case, the magnetic moment will align parallel or anti-parallel relative to $\vec{B}_0$. This in turn corresponds to different Zeeman

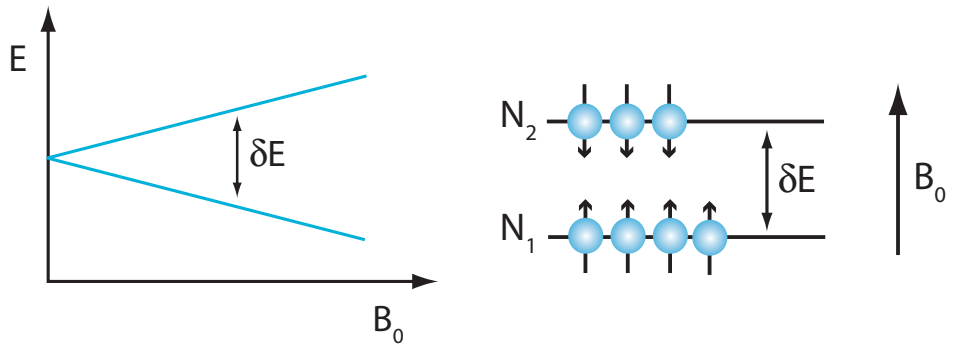

(a) (b)

Figure 2.1.: Scheme of the nuclear spin energy E for a spin-$^1/_2$ isotope as a function of the external magnetic field B_0 (a). Magnetic moments are aligned parallel (lower energy level) or anti-parallel (higher energy level) relatively to $\vec{B}_0$ (b). (cf. de Graaf, 2007)

energy levels (cf. Fig. 2.1(a)):

$$E_{\pm 1/2} = \begin{cases} -\frac{\gamma\hbar}{2} B_0 \ , & \text{if } \vec{\mu} \text{ is parallel to } \vec{B}_0 \\ +\frac{\gamma\hbar}{2} B_0 \ , & \text{if } \vec{\mu} \text{ is anti-parallel to } \vec{B}_0 \ . \end{cases} \tag{2.6}$$

Thus, the energy difference between two levels is given by: $E_m = -\gamma\hbar m_z B_0$. At the absence of an external magnetic field the different energy levels are degenerated.

Due to the thermal energy at room temperature the magnetic moments are nearly randomly aligned in the external B-field. According to the Boltzmann distribution the population ratio of two energy levels, N_1 and N_2, in thermal equilibrium at a certain temperature T is given by

$$\frac{N_2}{N_1} = \exp\left(-\frac{\delta E}{k_B T}\right), \tag{2.7}$$

where $\delta E = \gamma\hbar B_0$ is the energy difference between the levels and k_B corresponds to the Boltzmann constant (cf. Fig. 2.1(b)).
For example, at a B-field of 7 T and room temperature (293 K), the energy splitting for protons (^1H, $I = ^1/_2$) is about 1.2 µeV. In this case the occupation numbers are almost equal ($N_2/N_1 = 0.99995$). Only the tiny amount Δn of protons with a spin parallel to $\vec{B}_0$ (i. e. lower energy) excessing those with anti-parallel spin result in a net magnetisation

$$\vec{M} = \Delta n \cdot \vec{\mu} \tag{2.8}$$

and therefore are responsible for the NMR signal.

The phenomenon of NMR relies on the excitation of transitions between neighbouring Zeeman levels, which are separated by the energy δE. The irradiation of a resonant oscillating electromagnetic field perpendicular to $\vec{B}_0$ can course single nuclei to transition into a higher energy level. In this process, the corresponding frequency $\omega_0 = 2\pi\nu_0$ has to satisfy the following condition:

$$\omega_0 \;=\; \frac{\delta E}{\hbar} = \gamma B_0 \; . \tag{2.9}$$

At generally used magnetic fields (1.5 T to 7 T in human biomedicine) the resonance frequency is of the range of radio frequencies (MHz, cf. Table 2.1).

2.2. Equation of Motion in a Classical Model

The exciting radio wave frequency is identical to the Larmor frequency ω_L, which is — from a classical point of view — the frequency of precession of a single magnetic moment in a uniform B-field. It is the consequence of a torque

$$\vec{\Gamma}(t) = \frac{d\vec{I}(t)}{dt} = \vec{\mu}(t) \times \vec{B}(t) \; . \tag{2.10}$$

With Equation 2.3 one has the equation of motion

$$\frac{d\vec{\mu(t)}}{dt} = \vec{\mu}(t) \times \gamma\vec{B}(t) = \vec{\mu}(t) \times \vec{\omega_0}(t) \; . \tag{2.11}$$

Because of $\vec{M} = \sum_i \vec{\mu}_i$, Equation 2.11 can be analogous transferred into a net macroscopic magnetisation of an ensemble of free spins:

$$\frac{d\vec{M}(t)}{dt} = \vec{M}(t) \times \vec{\omega_0}(t) \; . \tag{2.12}$$

Usually $\vec{M}$ is decomposed into its spatial components, where M_z describes the direction of $\vec{B}_0$ (longitudinal) and $M_{x,y}$ are accordingly defined as its transverse components ($\vec{M}_{x,y} \perp \vec{B}_0$). Assuming the B-field is static, the solution of differential Equation 2.11 is

given by

$$\mu_x(t) = \mu_x(0)\cos\omega_0 t + \mu_y(0)\sin\omega_0 t \ , \tag{2.13}$$

$$\mu_y(t) = \mu_y(0)\cos\omega_0 t - \mu_x(0)\sin\omega_0 t \ , \tag{2.14}$$

$$\mu_z(t) = \mu_z(0) \ , \tag{2.15}$$

which describes a precession of the magnetic moment about $\vec{B}_0$ with the angular frequency $\omega_0 = \gamma B_0$.

2.3. Excitation by Radio Frequency Fields

In thermal equilibrium the spins have no phase coherence in the transversal plane while the longitudinal magnetisation vector is static. The detection of a magnetisation can only be achieved by rotating the vector of magnetisation from its steady state, in z-direction, towards or onto the transversal plane. This can be accomplished by irradiating a radio-frequency (RF) electromagnetic field perpendicular to $\vec{B}_0$ with the frequency ω. This results in an overall magnetic field

$$\vec{B}(t) = \begin{pmatrix} B_1\cos\omega t \\ B_1\sin\omega t \\ B_0 \end{pmatrix} . \tag{2.16}$$

As a suitable approach, the magnetic field can be transformed into a coordinate system rotating about $\vec{B}$, so that

$$\frac{d\vec{M}'}{dt} = \vec{M}' \times \gamma\vec{B}' \tag{2.17}$$

becomes time-independent. The prime symbol represents the rotating system, which gives an effective magnetic field:

$$\vec{B}' = \begin{pmatrix} B_1 \\ 0 \\ B_0 - \frac{\omega}{\gamma} \end{pmatrix} . \tag{2.18}$$

In the rotating frame, the magnetisation revolves this field. The third component of the effective field vanishes exactly at resonance ($\omega = \omega_0 = \gamma B_0$) and a solitary component B_1 in x-direction remains. As a consequence, the net magnetisation is flipped by an angle

$$\alpha = \gamma \int_0^{t_p} B(\tau) d\tau = \gamma B_1 t_p, \tag{2.19}$$

where t_p is the duration of an applied RF pulse. The magnetisation is flipped into the transversal plane, if $\alpha = \pi/2$. Such a pulse is called a "90°-pulse". Analogously, an $\alpha = \pi$ flip is named 180°-pulse, since the magnetisation is subsequently aligned in the opposite direction. In the laboratory frame of reference the motion of the magnetisation vector describes a spiral trajectory, which is shown in Figure 2.2.

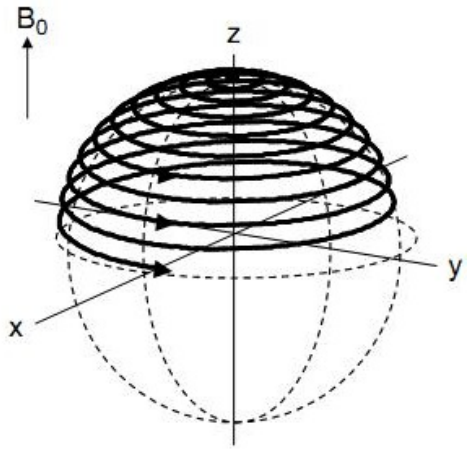

Figure 2.2.: Spiral trajectory of the net magnetisation in the laboratory frame at a 90°-excitation. The magnetic moment rotates about the static field $\vec{B}_0$ and the irradiated oscillating field $\vec{B}_1(\mathrm{t})$. As a consequence, a rotation of the magnetic moment from its steady state towards the transversal plane can be achieved (de Graaf, 2007).

2.4. Relaxation Processes

For a more precise model of motion, several processes of interaction between neighbouring nuclei and their environment have to be taken into account. These processes lead to a relaxation of nuclear magnetization after a RF-excitation (non-equilibrium state) back to the thermal equilibrium distribution M_0. In NMR there are two main relaxation mechanisms.

2.4.1. Spin-lattice Relaxation

The spin-lattice or longitudinal relaxation describes the nuclear magnetisation as it comes into thermodynamic equilibrium with its environment (or lattice). In the course of this, energy is interchanged between the spins and their surrounding (e. g. by the production or absorption of phonons in solids). That is because every transition of one energy level into another can only take place under the conservation of energy. The following equation describes the relaxation of the longitudinal magnetisation:

$$\frac{dM_z}{dt} = -\frac{M_z - M_0}{T1} \ , \tag{2.20}$$

where T1 is a constant, known as the spin-lattice relaxation time, or just T1-time. T1 is a specific property of a given material. Equation 2.20 can easily be solved by

$$M_z(t) = M_0 \left(1 - e^{-\frac{t}{T1}}\right) \ , \tag{2.21}$$

which describes an exponential rise of magnetisation M_z back to the thermal equilibrium magnetisation M_0.

2.4.2. Spin-spin Relaxation

The second, entirely uncorrelated relaxation mechanism, is called spin-spin or transversal relaxation. It is caused by dipol-dipol interactions between individual nuclei, which result in slightly different Larmor precessions and therefore in a reduction of phase coherence. The transverse magnetisation M_{xy} decays exponentially with a characteristic time constant T2 (or spin-spin relaxation time):

$$M_{xy}(t) = M_0 e^{-\frac{t}{T2}} \tag{2.22}$$

Usually, this process is superimposed by another, more technical conditioned mechanism, which is due to imperfections in the homogeneity of the external static field $\vec{B}_0$. The variation ΔB leads to an additional difference in Larmor precession and therefore to a more rapid decay of the transverse magnetisation. The corresponding time constant T2* can be expressed:

$$\frac{1}{T2*} = \frac{1}{T2} + \gamma \Delta B \ . \tag{2.23}$$

The T2* relaxation time is always shorter than the T2 time and while T1- and T2-relaxation are irreversible mechanisms, systematic or non-statistic T2* effects can be avoided by the usage of so called Spin-Echo measuring techniques (see Section 3.3.1).

2.5. Free Induction Decay and Detection

After a 90°-pulse at $t = 0$, the vector of equilibrium magnetisation M_0 is rotated into the transverse plane. Assuming the magnetisation is than given by $\vec{M}(0) = (M_0, 0, 0)^T$, the transverse magnetisation $\vec{M}_{xy}$ starts to precess about the z-axis and decays with the time constant T2* instantaneously. The longitudinal magnetisation $\vec{M}_z$ recovers simultaneously with T1:

$$M_x(t) = M_0 \cos(\omega_0 t + \phi) \cdot \exp(-t/T2^*) \tag{2.24}$$

$$M_y(t) = M_0 \sin(\omega_0 t + \phi) \cdot \exp(-t/T2^*) \tag{2.25}$$

$$M_z(t) = M_0(1 - \exp(-t/T1)) \tag{2.26}$$

The precession leads to a measurable induction signal ($U \propto dM(t)/dt$) in a coil perpendicular to $\vec{B}_0$, which decays with T2*. After a single pulse this signal is referred to as free induction decay (FID) (see Fig. 2.3).

A time-domain signal — the FID — is represented by a frequency-domain signal,

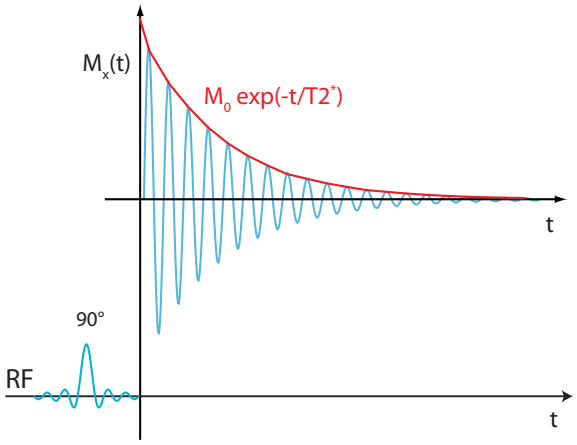

Figure 2.3.: Free induction decay (FID) of the transverse magnetisation $\vec{M}_{xy}$ following a 90° excitation pulse. The magnetization precesses at ω_0 and decays with the time constant T2*. (cf. Badurek, 2010).

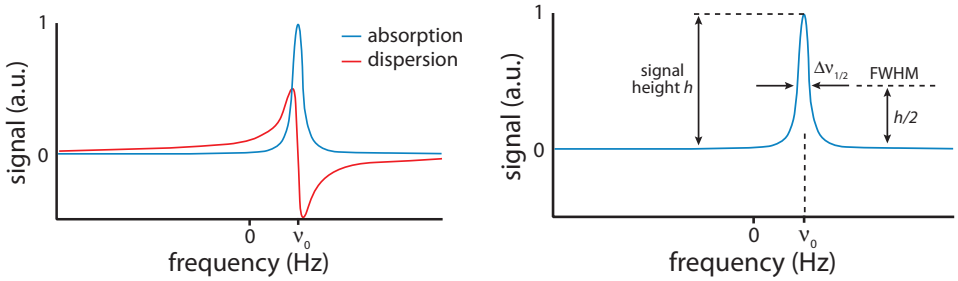

(a) (b)

Figure 2.4.: The complex Fourier transformation of an exponentially decaying FID gives rise to an absorption and dispersion component. The line width at half signal maximum (FWHM) of the absorption curve is governed by the relaxation time constant T2* (cf. de Graaf, 2007, chap. 1).

i. e. the spectrum, after a Fourier transformation (FT), which is mathematically given by

$$F(\omega) = \int_{-\infty}^{\infty} f(t)e^{-i\omega t}dt \ . \tag{2.27}$$

The FT of an acquired FID signal results in a complex frequency-domain signal (impedance):

$$F(\omega) \quad = \quad R(\omega) + iI(\omega) \tag{2.28}$$

Whereas the real part includes the absorption and the imaginary part the dispersion of the sample coil (for a phase $\phi = 0$). Both parts are shown in Figure 2.4(a). However, when $\phi \neq 0$ a mixture of absorption and dispersion signals is observed.
The full width at half maximum (FWHM) $\Delta\nu_{1/2}$ of the Lorentzian shaped absorption curve equals $(\pi T2^*)^{-1}$ (Fig. 2.4(b)).

2.6. The BPP Theory

In the model proposed by Bloembergen, Purcell and Pound in 1948, known as the BPP theory, the spin relaxation times are related to the lattice through molecular motions (Bloembergen et al., 1948). Thus relaxation effects depend on statistical fluctuations of dipole fields, which are produced e. g. by random motions of molecules in a liquid. This

fluctuations can be characterised by a correlation function

$$G(\tau) = \overline{B_{loc}(t)B_{loc}(t+\tau)}\,, \tag{2.29}$$

which describes the correlation of randomly fluctuating local fields B_{loc} within the time window τ. The Fourier transform of this function is called spectral density and is given by

$$\tilde{g}(\omega) = \int_0^\infty G(\tau)e^{-i\omega t}d\tau = \frac{\tau_c}{1+\omega^2\tau_c^2} \tag{2.30}$$

where τ_c is the time between significant fluctuations. Thus, the correlation time is a direct measure of the molecular mobility of a substance. Due to its crystalline structure, solids have a much larger correlation time ($\tau_c \cong 10^{-5}$ s) than fluids (10^{-12} s) (Vlaardingerbroek and den Boer, 2003). For a single spin-pair (assuming homonuclear dipolar coupling) the BPP theory leads to the following relationships between correlation- and relaxation time:

$$\frac{1}{T1} = C\left[\frac{\tau_c}{1+\omega^2\tau_c^2} + \frac{4\tau_c}{1+2\omega^2\tau_c^2}\right] \tag{2.31}$$

$$\frac{1}{T2} = \frac{C}{2}\left[3\tau_c + \frac{5\tau_c}{1+\omega^2\tau_c^2} + \frac{2\tau_c}{1+2\omega^2\tau_c^2}\right]\,, \tag{2.32}$$

where C is a constant factor.

As seen in Figure 2.5, the asymptotic behaviour of the relaxation time T1 is inversely proportional to the correlation time τ_c for fast fluctuations (less solid materials). The maximal relaxation rate (minimal T1 time) is obtained for nuclei, which are fluctuating with a frequency in the order of the Larmor precession frequency, i. e. for τ_c^{-1} equals approximately ω.
The spin-spin relaxation time T2 experiences a decrease for higher correlation times over the whole range of τ_c. The other way around, the line width $\Delta\omega$ of a NMR spectrum is broadened for materials with shorter T2 times, or T2* respectively:

$$\Delta\omega_{1/2} = \frac{2}{T2} \tag{2.33}$$

which is identical with the the aforementioned relation (Sec. 2.5).
In more descriptive words, the nuclear spins, which are diffusing around, will experience

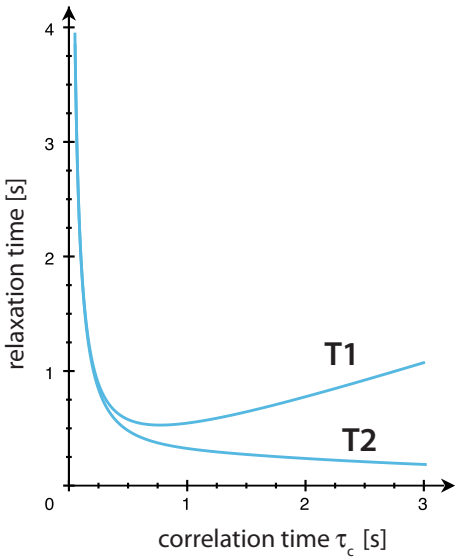

Figure 2.5.: Relaxation times T1 and T2 as a function of correlation time τ_c according to a single spin-pair model as described by the BPP-theory (Equ. 2.31-2.32). Here $C = 1$, $\omega = 1$.

different magnetic fields, sometimes higher, sometimes lower than B_0. The result is a decreased spread of field strength on time average. This implies that the de-phasing, due to various precession frequencies, is reduced and therefore T2 is greater. The phenomenon is also known as motional narrowing. For more bounded nuclei this averaging effect vanishes since the diffusion is less.

Chapter 3

Magnetic Resonance Imaging

Now we are using our understanding of the basics of NMR to discuss Magnetic Resonance Imaging (MRI) in this chapter. Beside the spectroscopy, MRI is an important application making use of the property of NMR. The proposal of MRI as a projection techniques by Paul C. Lauterbur and the further development based on Fourier transformation by Peter Mansfield was acknowledged with the Nobel prize in Medicine in 2003*.

3.1. Magnetic Field Gradients

Since the resonance frequency depends on the local magnetic field (Equ. 2.9), the key concept of MRI is to make full use of magnetic field gradients to give the resonance frequency a spatial dependency. Mathematically, a magnetic field gradient $\vec{G}$ is therefore described by:

$$\vec{G} = \left(\frac{\partial \vec{B}_0}{\partial x}, \frac{\partial \vec{B}_0}{\partial y}, \frac{\partial \vec{B}_0}{\partial z} \right)^T , \tag{3.1}$$

where x, y and z are spatial coordinates. In this case the external magnetic field is superimposed by the gradient field:

$$B(\vec{r}) = B_0 + \vec{r} \cdot \vec{G} \tag{3.2}$$

* "For their discoveries concerning magnetic resonance imaging" (Nobelprize.org, 2003).

and therefore the resonance condition (Equ. 2.9) has to be rewritten as:

$$\omega_0(\vec{r}) = \gamma B_0 + \gamma \vec{r} \cdot \vec{G} \,. \tag{3.3}$$

3.2. Spatial Encoding

3.2.1. Slice Selection

The first step to obtain 3D information is to select a certain slice within the object. This can be done by the combination of a specifically shaped RF pulse and a linear magnetic field gradient e. g. in z-direction (parallel to $\vec{B}_0$).
The slice thickness is determined by two factors, the gradient strength and the frequency bandwidth $\Delta\omega$ of the RF pulse. The stronger the gradient the thinner the excited slice. Whereas, the broader the RF bandwidth the thicker the slice. This relation is shown in Figure 3.1.

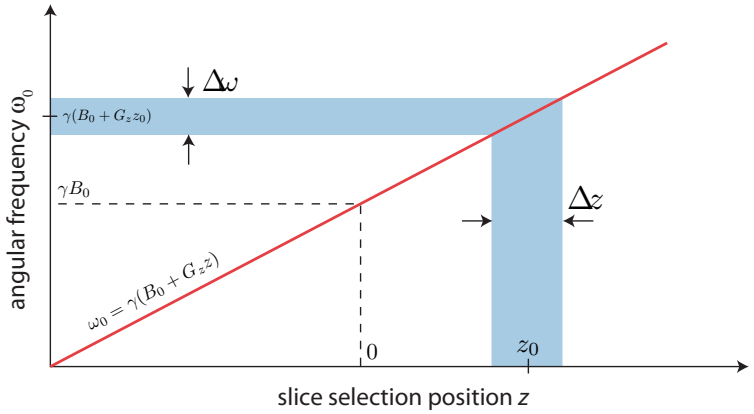

Figure 3.1.: The angular frequency ω_0 of precession as a function of slice select position along the z-axis when a gradient G_z is applied (Sec. 3.1). The slice thickness Δz depends on the gradient strength G_z and the frequency bandwidth $\Delta\omega$ (cf. Haacke et al., 1999, chap. 10).

The width of the slice is related to the shape and duration of the RF pulse via the Fourier transform of the RF pulse envelope. Thus, a sinc-pulse* in the time-domain gives a rectangular pulse in the frequency-domain. A Gaussian frequency profile remains unchanged in his shape.

* $\operatorname{sinc} x = \frac{\sin x}{x}$

3.2.2. Phase- and Frequency Encoding

After slice selection, two dimensions are left to encode within the slice plane. Frequency encoding is the process giving spatial information in one additional dimension and causes the resonance frequency to be proportional to the position of the magnetic moments (Equ. 3.3). Therefore, a linear gradient $\vec{G}(t)$ in the dedicated direction within the excited slice plane is switched on during the signal acquisition. The signal in k-space then satisfies the following relation

$$S(\vec{k}) = \int \rho(\vec{r}) \cdot e^{-i2\pi\vec{k}\cdot\vec{r}} d^3r \tag{3.4}$$

where $\rho(\vec{r})$ is the local spin density and

$$\begin{aligned} \vec{k} &= \gamma \int_0^t \vec{G}(t')dt' && (3.5)\\ &= \gamma\vec{G}t, && (3.6) \end{aligned}$$

if $\vec{G}$ is constant in time. In consequence, the FT of the FID corresponds to the one-dimensional projection of the object.

In order to obtain the residual dimension the spins in every single voxel have to be encoded properly before the signal is acquired during frequency encoding. In 2DFT imaging this is usually achieved by the application of a phase encoding gradient, which has to be switched N times in order to fill a $N \times N$-image-matrix (see Fig. 3.2). Therefore, the gradient amplitude is changed from $+G_{max}$ to $-G_{max}$ incrementally. During the active gradient, the spins precess with different frequencies, which are a function of position. After switching off the gradient, every spin gets an additional specific phase shift:

$$\phi(\vec{r}) = \gamma t_0 \vec{r} \cdot \vec{G} \; . \tag{3.7}$$

From the basic expression 3.4 of the signal in k-space, it follows immediately that the reconstruction of an image in real space can be achieved by taking the inverse FT of the sampled data:

$$s(\vec{r}) = \int S(\vec{k}) \cdot e^{i2\pi\vec{k}\cdot\vec{r}} d^3k. \tag{3.8}$$

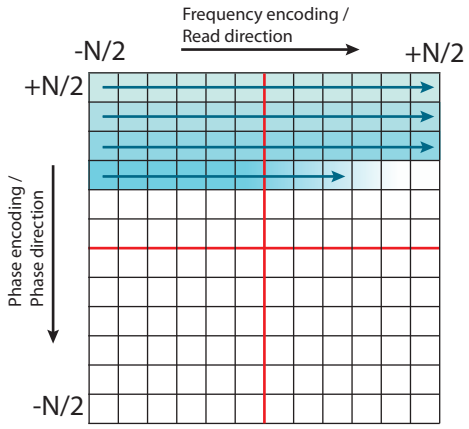

Figure 3.2.: Classical 2-dimensional FT k-space sampling: the $N \times N$-matrix is acquired line by line so that N sequence circles are required to completely fill the raw data space. (cf. Brix et al., 2008).

3.3. Important MRI Pulse Sequence Designs

This section gives a brief overview of some basic imaging techniques, which are of major significance in MRI and in particular of this work. The following basics and much greater detailed information can be found e. g. in Bernstein et al. (2004) and Haacke et al. (1999).

3.3.1. RF Spin-Echo

One of the fundamental pulsed MRI experiments is the RF spin-echo (SE) sequence. It is principally formed by a 90°-excitation pulse followed by one ore more 180°-refocusing pulses. In principle it is performed in a 2D-mode, i. e. slice-wise acquisition of single images as described in Section 3.2. Figure 3.3 shows a typical 2D SE pulse sequence diagram used for Fourier encoding. After the magnetisation is flipped into the transversal plane it begins to de-phase with the time constant T2* due to spin-spin relaxation. The application of a 180°-pulse refocuses the de-phasing spins, which produce a so called spin echo. The resulting FID can be frequency encoded and acquired by the Analog-Digital-Converter (ADC). The time from excitation pulse to the spin echo is named detection time or echo time (TE). After the repetition time (TR), a further 90°-excitation pulse is applied for the acquisition of the next line in k-space. A proper selection of TE and TR is necessary to control the amount of spin-density-, T1- or T2-contrast (or -weighting)

present in the image.
A sequence of multiple refocusing pulses in a row (multi-echo) gives the option to reconstruct multiple images with different T2-weighted (T2w) contrasts.
In order to speed up the total measurement time, a phase encoding after every subsequent 180°-pulse is possible, so that multiple k-space lines can be sampled after a single excitation, which reduces the total measurement time significantly (turbo factor). However, this turbo spin echo (TSE) method brings poorer signal-to-noise ratio (SNR, S/N) and an increased image artefact liability.

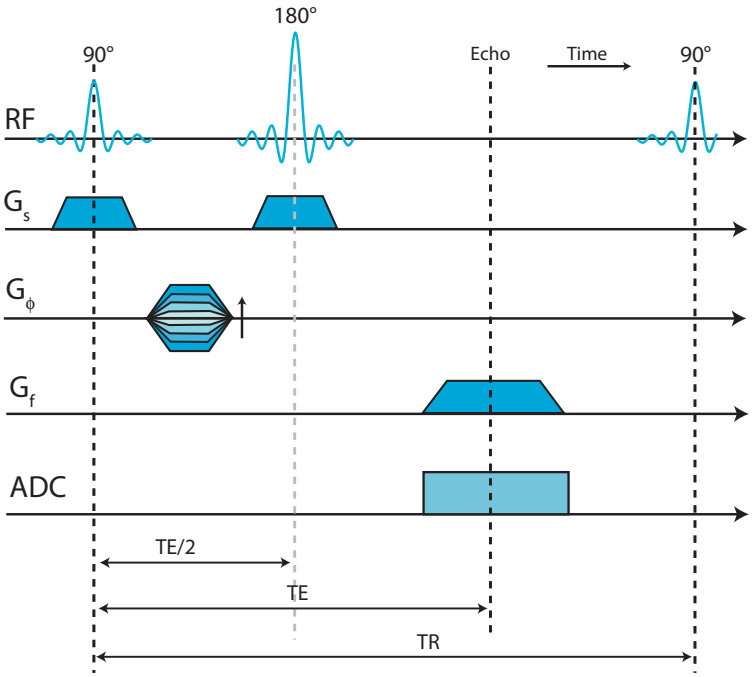

Figure 3.3.: A typical 2D spin echo pulse sequence diagram used for Fourier encoding. After the magnetisation is flipped into the transversal plane by a slice-selective 90°-pulse, the spin system gets phase-encoded. At the time TE/2, a 180°-pulse refocuses the de-phasing spins and a spin echo is produced, which gets frequency encoded and acquired by the Analog-Digital-Converter (ADC).

3.3.2. Gradient-Echo

Another method to form a spin echo is to de- and re-phase the single spins using additional, bipolar switched magnetic gradient pulses. In Figure 3.4 a sequence diagram for a conventional gradient echo (GE) pulse sequence is shown. To achieve a shorter repetition

time, usually GE sequences excites the magnetisation using low angle RF-pulses. This in turn reduces the scan time to a reasonable duration without any saturation effects. However, one has to take a loss in signal intensity, since $\alpha < 90°$. Also, the absence of a 180°-pulse makes shorter detection times in the range of 1 ms to 2 ms achievable.
After the slice selection and phase encoding gradients are turned off, for a period of time a negative gradient is applied, which leads to a de-phasing of the transverse magnetisation. Subsequently, the echo is produced due to a re-phasing read gradient.
Unlike the RF-SE sequences, this more rapid sequence design offers no compensation of local field inhomogeneities, nevertheless it became quite popular as the basis of sequences applied whenever a fast detection is necessary (cf. Zientara, 1995).

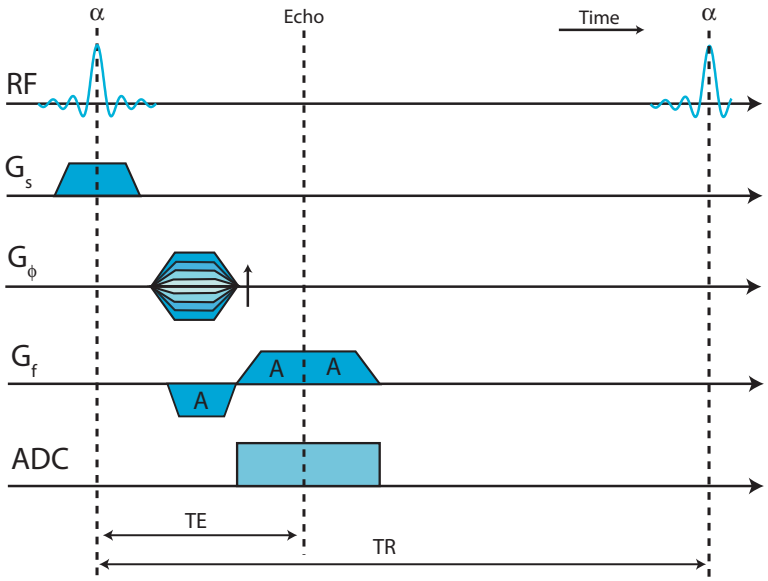

Figure 3.4.: A generic 2D gradient echo pulse sequence diagram used for Fourier encoding. The symbol A refers to the area under the gradient. To produce a spin echo exactly at TE, the defocusing lobe in read direction has got to have half the area of the read gradient. To shorten the echo time, the phase encoding gradient and the de-phase lobe of the read gradient can be switched on at the same time (cf. Haacke et al., 1999, chap. 10).

3.3.3. Preparation Methods

In some cases RF pulses are used to prepare the spin system for the ensuing measurement in such a way that additional contrasts (e. g. IR, T1ρ) can be attained (Bakshi et al., 2001; Engelhardt and Johnson, 1996), or undesired signals (like fat protons) can be

selectively suppressed (Delfaut et al., 1999). Within this work the magnetisation transfer contrast is of peculiar interest.

Magnetisation Transfer Contrast

Magnetisation Transfer Contrast (MTC) is a preparation method to selectively increase image contrast by reducing the MR signal of tightly bound protons. It was first discovered by Wolff and Balaban in 1989 as a method to suppress background tissue (Wolff and Balaban, 1989). The contrast mechanism of magnetization transfer imaging is based on exchange processes between bulk water protons and macromolecular bound protons. These protons are restricted in motion, like in cell membranes, proteins and lipid bilayers of biological tissue (Mehta et al., 1996).

As described by the BPP-theory (Sec. 2.6) a constrained mobility of protons leads to a broadening of the spectral line. In a heterogeneous material containing both pools, bulk and bound protons, the absorption spectrum corresponds to a narrow peak at the resonance frequency of liquid water superimposed by a broad background (Fig. 3.5). These much broader lineshape makes the bound pool as much as 10^6 times more sensitive to an off-resonance RF-pulse (Henkelman et al., 2001). A sufficient strong off-resonance RF-pulse gives rise to a saturation of the affected spin system. Saturation is a non-equilibrium state, where the population differences of the Zeeman levels are equalised so that the net magnetisation is zero (Badurek, 2010).
A suppression of unwanted magnetisation can also be achieved by a subsequent spoiling gradient, i. e. strong de-phasing gradient, after the excitation (Delfaut et al., 1999), or by the application of a progressive binomial RF pulse (Ropele et al., 2006).
The effect of MT pulses can be analysed with a model that assumes two pools. The first pool A contains the bulk, liquid, mobile or free protons, whereas the second pool B includes the bound, restricted or macromolecular protons (Bernstein et al., 2004). Figure 3.6 illustrates this model. In both pools exist excited and saturated spins at any time (whereby only the exited spins are accessible for MR-imaging). The time-dependent ratio is determined on the rate of longitudinal relaxation R_a or R_b (the inverse of T1), the rate of loss of magnetisation R_{rf}, due to the off-resonance irradiation, and the rate of exchange between both pools R. This simple model was interpreted quantitatively by Henkelman et al. (1993) and can be expressed as a couple of differential equations

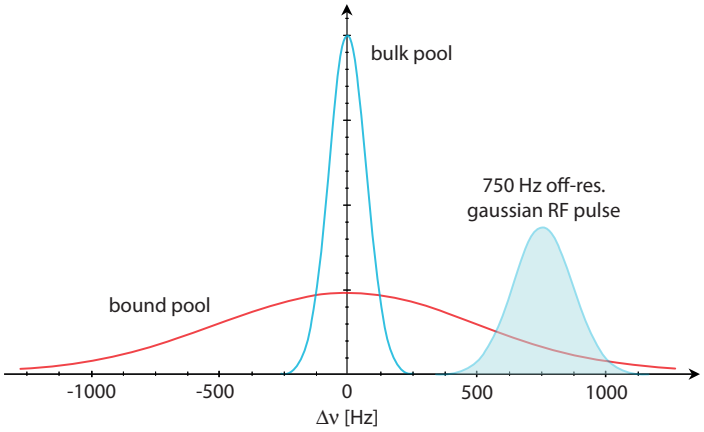

Figure 3.5.: Schematic absorption spectrum of a heterogeneous material containing both pools, bulk and bound protons. The bound protons exhibit a much broader absorption lineshape, which makes them considerable more sensitive to an off-resonance RF-pulse (cf. Henkelman et al., 2001).

describing the available longitudinal magnetisation as a function of off-resonance RF saturation. Furthermore, quantitative experimental methods allow the direct determination of the bound pool fraction (Soellinger et al., 2011).
The mechanisms which exchange magnetizations between the liquid and restricted pool including on the one hand through-space magnetic dipolar interactions (dipole–dipole coupling) between macromolecular protons and specific free protons at the boundary layer, and on the other hand direct physical or chemical exchange of protons (Ceckler et al., 2001). However, these mechanisms are distinguishable neither in the theoretical model, nor in the actual experiment.

3.4. Limitation on the Spatial Resolution

There are some physical and technical factors which are limiting the attainable resolution in MRI, such as chemical shift, molecular diffusion, magnetic field inhomogeneities and signal-to-noise-ratio (Kuhn, 1990). The spectral line width is another important limitation. With Equ. 2.33 and 3.3, the theoretical resolution is given by

$$\Delta x = \frac{2}{\gamma \cdot G_x \cdot T2^*}. \tag{3.9}$$

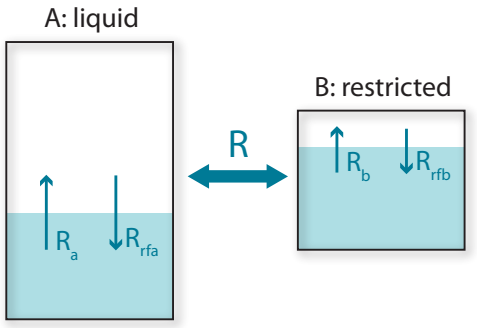

Figure 3.6.: Illustration of a two-pool model of magnetisation transfer exchange. The blue shaded area represents the saturated spins. $R_{a,b}$ is the rate of longitudinal relaxation, R_{rf} the rate of loss of magnetisation, due to the off-resonance irradiation, and R represents the rate of exchange between both pools. (cf. Henkelman et al., 1993).

One can see, that the maximal resolvable structural details are decisively dependent on the material and the gradient strength. High resolution imaging on semi-solid or solid substances requires relative strong gradients.
An additional effect of short-T2 materials is the decay of the NMR signal during acquisition. This leads to a reduced signal strength at the outer regions of k-space, i. e. higher spatial frequencies. This in turn results in a wider point spread function (PSF) and an increased blurring. To reduce this effect, it is recommendable to shorten the detection time T_{read} and keep it smaller than T2* (Parish et al., 1997). An accessible parameter to control T_{read} is the readout bandwidth $BW = T_{read}^{-1}$, so that

$$BW > \frac{1}{T2^*}. \tag{3.10}$$

The BW is restricted by the available gradient hardware.

A very fundamental limiting factor of spatial resolution is the signal-to-noise-ratio since the signal available from each voxel volume decreases as its size is reduced (Callaghan, 1991). Overall, the SNR is proportional to the voxel size V_{voxel}, and to the number of measurements, i. e. scan time, and inversely proportional to the receiver bandwidth BW:

$$\mathrm{SNR} = K \cdot V_{voxel} \cdot \sqrt{\frac{N_x N_y N_z N_{aqu}}{BW}}, \tag{3.11}$$

where $N_{x,y,z}$ is the number of encoding steps along the direction in question, N_{aqu} is the number of signal averages and K is a hardware-depending constant.
The SNR is also connected to the static field strength B_0 . Since the energy splitting of the Zeeman levels are directly proportional to B_0, the resulting population difference is larger at high values of B_0 (at a constant thermal energy). Besides this, the precession frequency of magnetisation increases with higher field strengths leading to a more rapid change of flux induced within the receiver coil (Redpath, 1998). In order to obtain higher SNR and therefore – amongst others – a higher resolution, the trend is more and more towards higher field strengths in (clinical) MRI.

3.5. Image Reconstruction

In Section 3.2.2 we saw that the standard image reconstruction in MRI is the (2D) Fourier Transformation of k-space. Practically, the data exists in a discrete form (sampled at discrete time intervals), which makes the application of the Discrete Fourier Transformation (DFT) necessary. In consequence, the continuous integration of Equation 3.8 is replaced by a summation:

$$s(\vec{r}) = \sum_j S(\vec{k}_j) \cdot e^{i2\pi \vec{k}_j \cdot \vec{r}}. \tag{3.12}$$

This task can easily be done by the Fast Fourier Transform Algorithm (FFT) if the data is sampled on a Cartesian matrix of the size $N = 2^n$ ($n \in \mathbb{N}$).

3.5.1. Non-Cartesian Reconstruction

Data acquired on a non-Cartesian grid, such as radial or spiral k-space data, can not readily be reconstructed by the DFT. To avail the benefits of the established FFT, one has to regrid the data on a Cartesian matrix. For this purpose, the most simple and fastest interpolation method is the Nearest Neighbour method (Oesterle et al., 1999). Here, the signal from every data point is added to the nearest Cartesian point.
Another method is gridding using convolution of the sampled data with a kernel whose width increases with radius k (Glover and Pauly, 1992; Schomberg and Timmer, 1995). In the case of radial sampling the reconstruction is often performed by a regridding algorithm instead of the time-honoured filtered backprojection (FBP) because of its flexibility for accommodating short-TE acquisition (Glover and Pauly, 1992). In this

connection the regridded data is correctable for a non-constant k-space velocity during the ramp-up period of the read gradient. Moreover, a FBP in three dimensions is a quite complex undertaking and is uncommon for medical imaging (Prof. N. Gurker, Vienna UT, priv. comm.).

Part II.

Materials and Methods

Chapter 4

Materials

This chapter gives an overview of the used hardware, the design and functionality of the applied pulse sequence and the individual samples of reference.

4.1. Hardware

4.1.1. The MR Scanner

All experiments were performed on a 7 T whole-body MR scanner (Magnetom 7 T, Siemens Healthcare, Erlangen, Germany) (Fig. 4.1), which went into line in 2008 at the MR Center of Excellence in Vienna (MedUniWien, 2008). The system works with a helium-cooled, super-conducting Nb-Ti magnet producing a static 7 Tesla magnetic field (Siemens AG Healthcare, 2002).
The scanner weighs 34 tons and the magnetic field is passively shielded by 270 tons of iron located around the scanner within the walls of the scanner room. Beyond a radius of a few meters outside, the magnetic field strength is less than 0.5 mT (5 Gauss), which is considered to be the safe boundary for the general public.
The magnet (without casing) has an outer diameter of 2.4 m and a length of 3.4 m. The available inner diameter of the bore is 60 cm (Siemens AG Healthcare, 2002).

The system is connected to an appropriate host computer for the measurement control, running a Windows XP operating system and the Siemens Syngo MR user interface

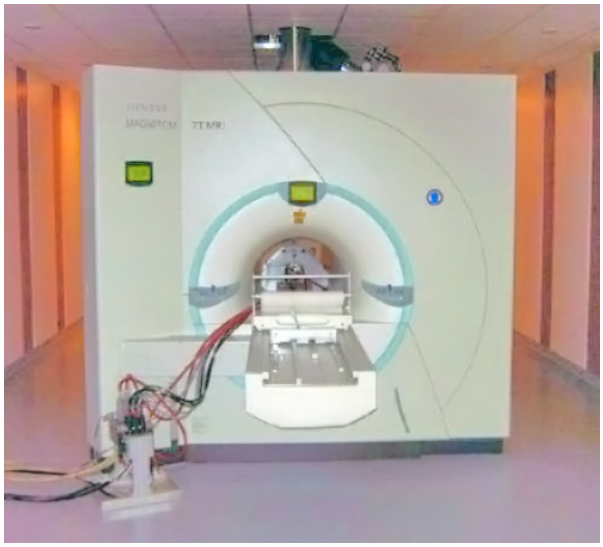

Figure 4.1.: 7 T whole-body MR scanner (Siemens Magnetom 7T) at the MR Center of Excellence in Vienna (Berg et al., 2010).

(UI) and is specifically configured for the microimaging gradient system. The image reconstruction is done separately by a second processing computer, which also stores the raw data for a period of time.

4.1.2. The Gradient Insert

The integrated whole-body magnetic gradient system* attains a gradient field strength of 31 mT m^{-1} (Siemens AG Healthcare, 2002). To achieve MR microimaging with high spatial resolution, stronger gradients are required (cf. Sec. 3.4). In combination with the whole-body MR scanner, this is allowed by a specific gradient coil insert (RRI Small Animal Gradient Coil, Resonance Research Inc., Billerica MA, USA) featuring a maximum gradient amplitude of 750 mT m^{-1} (Fig. 4.2). The inner diameter of this custom designed device is 90 mm. The gradient insert is installed in the bore of the magnet on the patient layer into the magnetic isocenter and is connected to the voltage- and current-limited whole-body gradient power amplifier (Max. 600 V/300 A). The custom interface also assures the supply of water cooling and shimming currents. A

* The gradient system is designed and financed within funds of the ÖNB-project No. 10229 (project manager A. Berg) and investments by the Center of Medical Physics and Biomedical Engineering (A. Berg, E. Moser). The installation was possible within funds of an upgrade to the 7T scanner (institute managers: S. Trattnig, E. Moser).

"Frankenstein-Switch" allows the user to switch between both gradient systems (Siemens AG Healthcare, 2010).
The gradient insert is equipped with additional Pt100 sensors in order to monitor the temperature at various position around the gradient coil. The temperature profile over time can be displayed graphically on a separate PC using an Ethernet Multimeter / Data Acquisition System (Keithley Instruments Inc., Cleveland OH, USA) and the MS Excel Add-In "ExceLINX". For reduction of vibrations due to the rapid gradient switching, an additional swivel arm can be adjusted to press against the inner wall of the bore.
Owing to technical reasons, a conversion factor of 5 for the gradient amplitude is always to be taken into account. This also leads to indicated geometric spatial distances shown by the user interface that are 5-fold smaller than reality (Siemens AG Healthcare, 2010). With this system, including highly sensitive RF coils (Sec. 4.1.3), structures of about 34 µm can be visualised using turbo spin echo sequences (Berg et al., 2010).

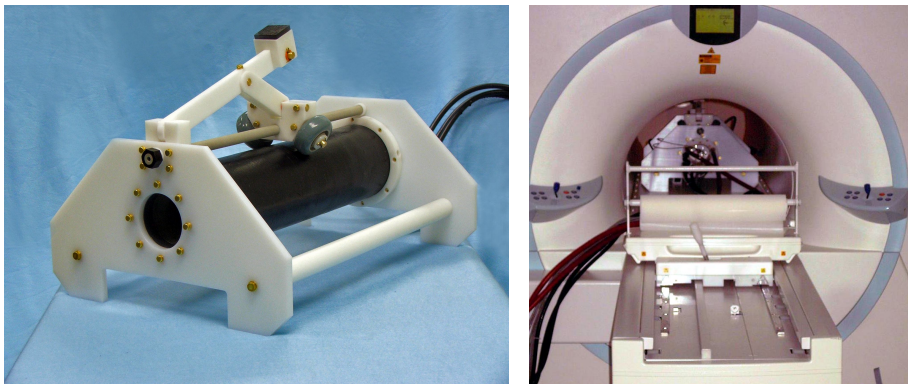

(a) (b)

Figure 4.2.: (a) Custom designed gradient insert for MR microimaging on a whole-body scanner ($G_{max} = 750\,\mathrm{mT\,m^{-1}}$, $d_{inner} = 90\,\mathrm{mm}$). (b) Gradient insert inside of the whole-body scanner. The device is positioned on the patient layer in the isocenter of the magnetic field. (Berg et al., 2011).

4.1.3. The RF coils

Two volume resonators were provided for measurements in combination with the microimaging gradient insert. A small sized ^{1}H NMR Volume Coil (V-HQ-070-00748, Rapid Biomedical GmbH, Rimpar, Germany) with an inner diameter of 19 mm was mainly used for sensitivity reasons. It is a quadrature birdcage coil and designed for RF

transmission and reception (Tx/Rx) (Rapid Biomedical GmbH, 2007).
In order to investigate larger samples or phantoms, a second resonator was available ($d = 72\,\text{mm}$). This ^{1}H NMR Volume Coil (V-HLS-070-00838-001, Rapid Biomedical GmbH, Rimpar, Germany) is a linearly polarized resonator for Tx/Rx or Tx-only operation (Rapid Biomedical GmbH, 2008).
Since both coils are not adjusted to a fixed frequency, one has to tune and match them before each measurement to adjust the impedance of each channel to $50\,\Omega$ at a ^{1}H resonance frequency of 297.18 MHz. This procedure was repeated manually after every significant change of position or type of the sample.
Some technical specifications of the used resonators are listed in Tab. 4.1.

Volume Coil	19 mm	72 mm
Max. peak power [W]	100	80
Max. peak voltage [V]	70	66
Max. cw power [W]	5	4
Ref. Amplitude [V]	6	31

Table 4.1.: Technical specifications of the used resonators.

4.2. Reference Samples

In this work, various phantoms and samples were investigated, which were adapted to the specific needs and chosen depending on the particular experiment. The following section gives a listing and explanation of all phantoms used for sequence quality control.

Short-T2 Phantoms

In order to evaluate the imaging performance on solid or semi-solid materials, two phantoms were made using a hot melt adhesive (HMA) agglutination. Hot melt adhesives are based on cross-linked polymers like polyethylene $(C_2H_4)_n$ and represent a material with restricted motional capabilities (short T2). In Figure 4.3 two phantoms are shown. In one case (a) a HMA cube (approx. $8 \times 7 \times 7$ cm^3) is placed on a Teflon holder (Polytetrafluoroethylene, $(C_2F_4)_n$). In a second phantom (b) an amount of HMA is placed

into a syringe surrounded by water. This phantom allows the measurement of a long- and short-T2 substance simultaneously side by side.

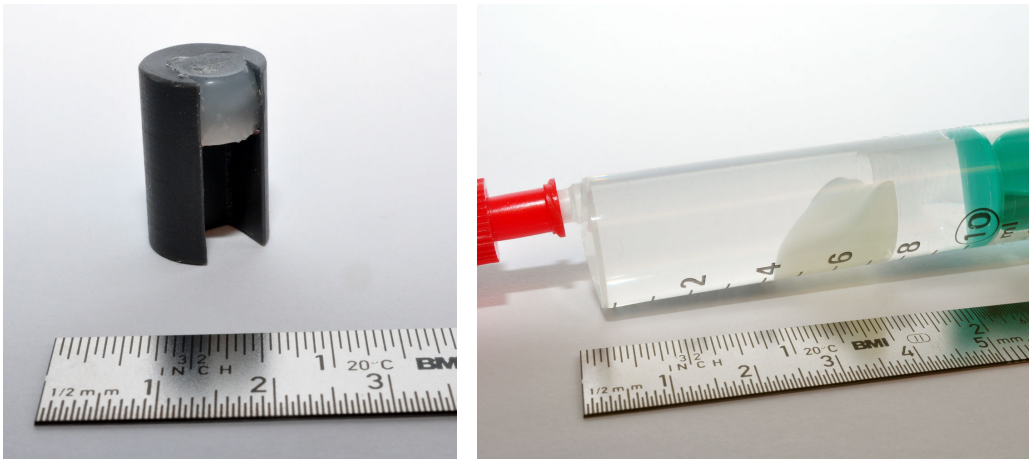

(a) (b)

Figure 4.3.: Short-T2 Phantoms: (a) Hot Melt Adhesive (HMA) cube (approx. $8 \times 7 \times 7$ cm^3) in Teflon holder. (b) HMA placed in a syringe ($d = 17$ mm) surrounded by water.

Resolution Phantoms

Two phantoms were designed to determinate the spatial resolution of the examined pulse sequence. The focus here was especially the relation between small structures and materials with short T2-times. The first phantom for this purpose is shown in Fig. 4.4(a). It consists of four relatively thin filaments (0.6 mm to 1.0 mm) of HMA stretched over a cylindrical Teflon holder. Another resolution phantom is shown in Fig. 4.4(b). Here, a syringe, filled with water, contains a glass capillary with an outer diameter of about 500 µm. Because this phantom is air filled, it can be used to determine the inverse point spread function (PSF) of the evaluated sequence in a first-order approximation.

MTC Phantoms

For validation of the MT contrast functionality, different types of samples were set up. As described in Sec. 3.3.3, an appropriate MTC phantom has to contain interacting bound and free protons (two-pool model).
Figure 4.5(a) shows one of the used cross-linked bovine serum albumin (BSA) phantoms,

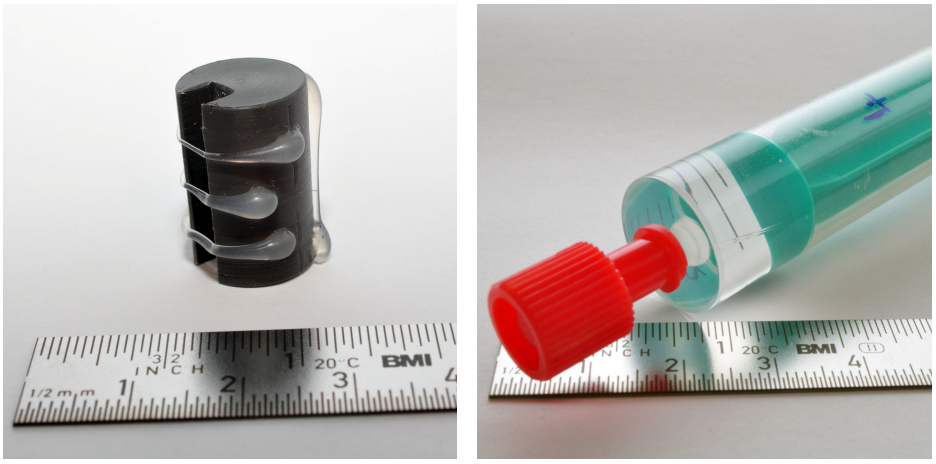

(a) (b)

Figure 4.4.: Resolution Phantoms: (a) Four HMA filaments (0.6 mm to 1.0 mm) stretched over a cylindrical Teflon holder. (b) Glass capillary (approx. 500 µm) containing air within a water filled syringe ($d = 17$ mm).

which were available in different concentrations*. For a detailed instruction of BSA sample preparation see Soellinger et al. (2011).
The second phantom (shown in Fig. 4.5(b)) encloses three different materials in water: two textile samples made of 100 % cotton and a blended fabric respectively, as well as an elderberry stem (*Sambucus nigra*).

Other Phantoms

Multi purpose samples, e. g. for general sequence performance and test measurements, were small test tubes ($d \approx 10$ mm to 12 mm, sealed air tight) filled with agar-gel (galactose polymer), or agarose (0.8 % and 1,2 %) respectively.

4.3. The Pulse Sequence

The evaluated and modified pulse sequence is a Siemens work-in-progress (WIP) sequence based on the product version of the cardiovascular sequence *a_CV* (Nielles-Vallespin et al., 2009). The WIP package provides the sequence- and reconstruction

* With kind permission of Prof. Stefan Ropele, Medical University of Graz

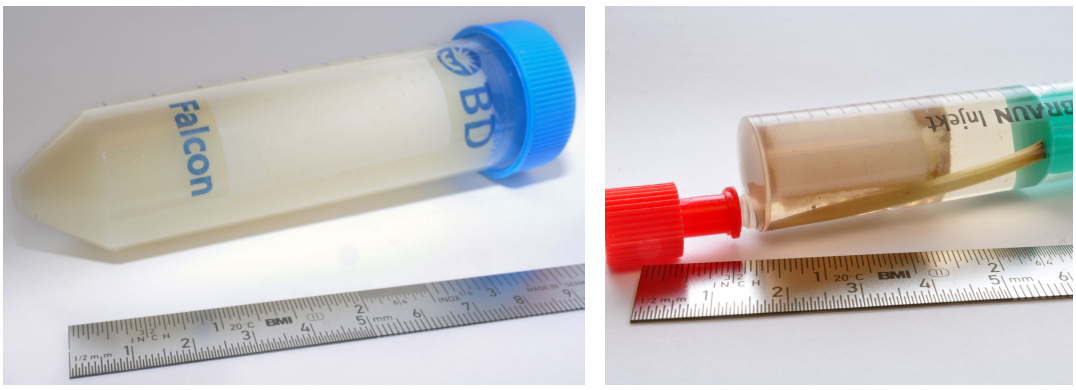

(a) (b)

Figure 4.5.: Magnetisation Transfer (MT) Phantoms: (a) One of the used cross-linked bovine serum albumin (BSA) phantoms (S. Ropele, Medical University of Graz). (b) MT phantom with three different materials in water: two textile samples made of 100 % cotton and blended fabric respectively, as well as an elderberry culm (*Sambucus nigra*).

source code and was offered to the MR-center by Siemens (L. Lauer) in cooperation between V. Juras and A. Berg within the "VIACLIC" research programme*.
The sequence was developed in the first place by Nielles-Vallespin (2004) during her doctorate for fast ^{23}Na-imaging. The timing diagram is shown in Figure 4.6. In contrast to the standard MR-sequences discussed in Sec. 3.3, this pulse sequence is designed for 3D radial imaging and samples the k-space from the centre to the surface of a sphere. The effective gradient describes a spiral-like trajectory over the surface of a sphere in N steps (Staff and Kuijlaars, 1997):

$$G_{x,n} = G \sin\theta_n \cos\phi_n \tag{4.1}$$

$$G_{y,n} = G \sin\theta_n \sin\phi_n \tag{4.2}$$

$$G_{z,n} = G \cos\theta_n \tag{4.3}$$

with the discrete polar and azimuthal angle

$$\phi_n = \left(\phi_{n-1} + \frac{3.6}{\sqrt{N(1-h_n^2)}}\right) \bmod (2\pi) \tag{4.4}$$

$$\theta_n = \arccos h_n \tag{4.5}$$

* Vienna Spots of Excellence (WWTF) – Vienna Advanced Imaging Center (VIACLIC). S. Trattnig and G. Reiter.

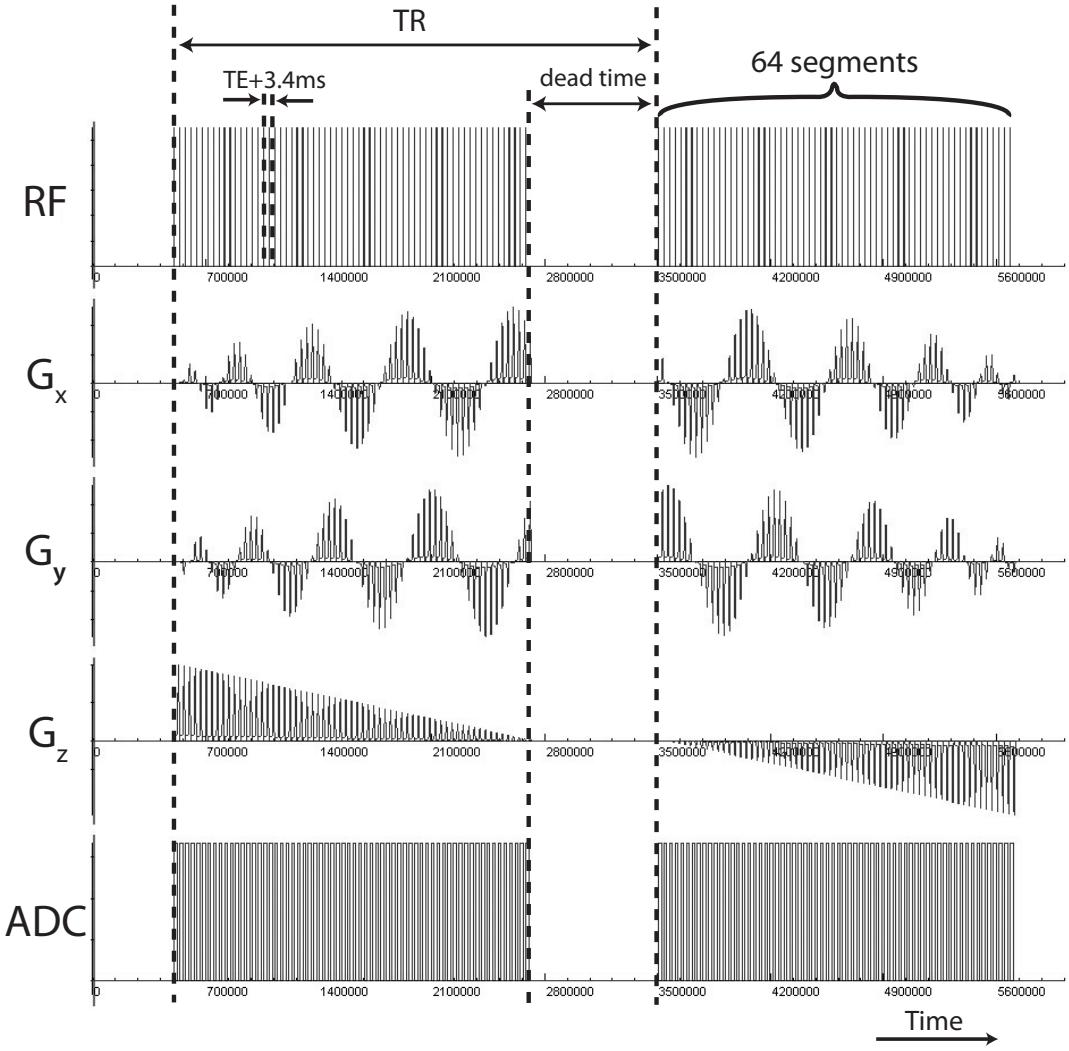

Figure 4.6.: Simulated timing diagram of *CVUTE_417*. Parameters: TR = 300 ms, TE = 70 µs, 128 Radial Profiles and 64 segments.

and

$$h_n = -1 + \frac{2n}{N} \qquad n = 1, \ldots, N \tag{4.6}$$

This model is exemplary shown in Figure 4.7.

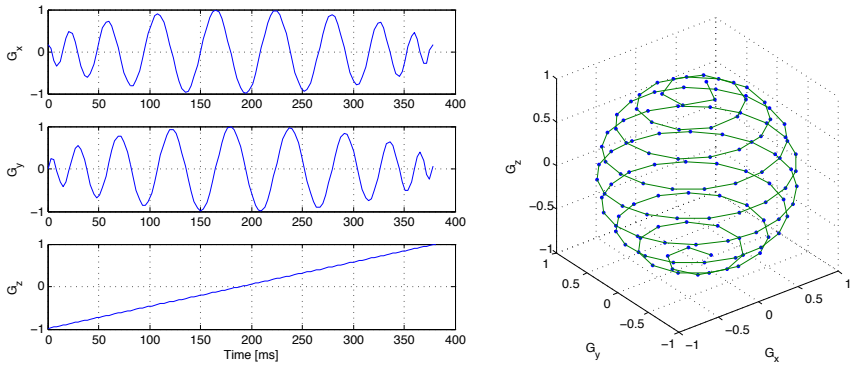

(a) (b)

Figure 4.7.: Simulation of the magnetic gradient amplitude (a) and trajectory (b) related to a 3D radial pulse sequence. The calculation is accorded to a mathematical model by Staff and Kuijlaars (1997) ($G = 1$, TR $= N \cdot 3\,\text{ms}$, $N = 128$).

Immediately after the RF-excitation (steady state excitation), the spatial information within the FID is frequency encoded and acquired during the readout gradient ramp-up time. A following spoiler gradient, modulated in the same manner as the readout gradients, destroys possible residual magnetisation (see Fig. 4.8). This results in a number N_{rad} of radial profiles (radial views) similar to a classical backprojection technique. After coverage of the full 3-dimensional k-space, the image is reconstructed by a regridding technique featuring a Kaiser-Bessel convolution kernel (see Subsec. 3.5.1).
The absence of phase-encoding or slice-selection refocusing gradients allows an ultra-short detection time, hence those types of sequences are also called ultra-short encoding (UTE) pulse sequences. The effective detection time TE is given by half of the RF pulse duration τ_{RF} and the time needed for Tx/Rx switching τ_{Delay}. The present pulse sequence achieves a minimal detection time of $70\,\mu\text{s} = 0.07\,\text{ms}$.
Different from from the usual definition of recovery time TR, here TR is the time interval, which is available for the application of n radial views (segments). The default segment number is set to $n = 64$, but can be changed by the user. The time τ_{inter} between two RF excitation pulses is given by TE and a specific constant dead time of approximately 3.4 ms. If the user chooses a TR time longer than $n \cdot \tau_{inter}$ (which is the minimal possible

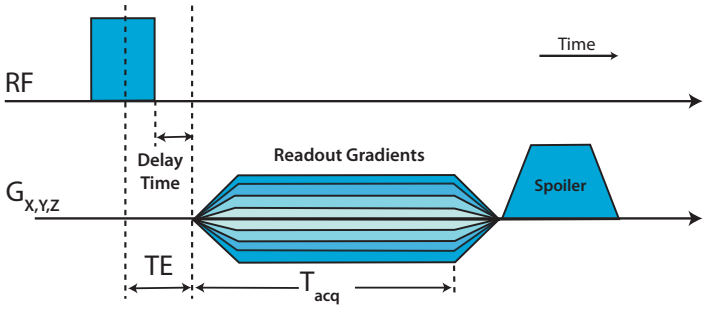

Figure 4.8.: Schematic sequence timing. After a RF pulse, the FID is frequency encoded and acquired during the readout gradient ramp-up time. A subsequent spoiler gradient destroys possible residual magnetisation. The effective detection time TE is given by half of the RF pulse duration τ_{RF} and the time needed for Tx/Rx switching τ_{Delay}. (cf. Nielles-Vallespin et al., 2007)

time), an additional dead time is added by the sequence before further profiles are measured (see Fig. 4.6). Accordingly, the resulting measurement time is given by

$$\tau_{meas} = N_{aqu} \left(\frac{N_{rad}}{n} \cdot \mathrm{TR} \right) , \tag{4.7}$$

where N_{aqu} is the number of repeating acquisitions.
However, the sequence is highly sensitive to gradient imperfections, since the sampling already begins while ramping up the readout gradients. Small timing delays (or gradient delays) can produce deviations from the expected profile position and therefore image artefacts.

Chapter 5

Methods

The following chapter focuses on the most important used methods. This includes, besides from the software-sided framework, all the modifications that were made within the sequence source code and the corresponding methods of analysis.

5.1. IDEA and ICE Programming Environments

The Integrated Development Environment for Applications (IDEA) is a Siemens programming platform allowing scientific users developing own MR pulse sequences. The used stand-alone version runs the baseline NUMARIS/4_VB15A on an emulated Microsoft XP SP3 operating system (Sun VirtualBox 3.1). The source code is written in the programming language C++ (.cpp/.h files).
The IDEA environment offers several tools for sequence developing. It combines the possibilities to compile, test, simulate and visualise the sequence. The C++ compiler is provided by MS Visual C++ 6.0.
A pulse sequence is modular designed using dynamically linked libraries. This can make the source code to a quite complex construct. Nevertheless, to run the sequence on the MR scanner, two different targets have to be built: one .dll-file for the host computer (Windows XP) and one .i86-file for the Measurement and Physiological Control Unit (MPCU).
The counterpart to the C++ sequence is the so called Image Calculation Environment (ICE), which gives a framework for raw data calculation and image reconstruction. This

can also be done at a stand-alone PC, while at the scanner, the reconstruction takes place on a separate Linux computer.
To generate input files for stand-alone ICE simulation (icesimu), the raw data (*meas.dat*) has to be exported from the data RAID manually by the TWIX user interface.
The output data produced by icesimu are .ima-files, which contains image data only while the header information is written separately. These files can not be read by common image viewers (like imageJ). To make them readable, a small batch program* was used to combine the image data with the header information resulting in a .png-file.

5.2. Building a TSE+MTC Sequence

The standard turbo spin echo sequence (TSE) by Siemens already contains an option for magnetic transfer contrast, but varying the pulse amplitude is the only degree of freedom the user has in order to manipulate the resulting image. Important parameters like frequency offset and pulse duration (and therefore frequency bandwidth) are not open to influence. The behaviour of the MTC RF pulse is determined within the "MSat" Sequence Building Block† (SBB) for different magnetic field strengths (List. 5.1).

Listing 5.1: Standard MTC pulse determined within SBBMSat.cpp line 110-127

```
110 long RF_Duration    = RFP_DURATION_MSAT;
111
112     if ( getNominalBZero() < 0.5 )
113     {
114         RF_Duration    = RFP_DURATION_MSAT * 2;
115         setFrequencyOffset(1000);
116     }
117     else if ( getNominalBZero() > 2.5 )
118     {
119         RF_Duration    = static_cast<long>(RFP_DURATION_MSAT * 1.3);
120         setFrequencyOffset(1200);
121         m_lPostTime = static_cast<long>(160 + RFP_DURATION_MSAT * 0.5);
122     }
123     else
124     {
125       RF_Duration    = RFP_DURATION_MSAT;
126       setFrequencyOffset(MSATOFFSETFREQHz);
127     }
```

For a nominal B_0-field of 7 T, the RF pulse is Gaussian shaped with a frequency offset of 1.2 kHz and a duration of 9984 µs ≈ 10 ms, because RFP_DURATION_MSAT is defined to be 7680 µs in SBBMSat.h (line 59, same directory).

* Vladimir Juras, MR Centre of Excellence, Vienna. † /n4/pkg/MrServers/MrImaging/libSBB/SBBMSat.cpp

To allow the user full control over all important parameters, an existing T1ρ-sequence was properly modified. The sequence was developed within a master thesis of a postgraduate course by Stefan Berger (2011). The resulting source code file is called "tse_mtc.cpp". A Gaussian shaped saturation pulse was placed between a prefacing spoiler gradient and the 90° rf excitation (Fig. 5.1). The voltage amplitude of this saturation pulse can be manipulated in the user interface at the System/TransmitterReciever card, while the Sequence/Special card provides all other adjustable parameters (Fig. 5.2):

Saturation Pulse Checkbox en- and disabling the saturation pulse.

Freq. Offset Off-resonant frequency offset in Hz.

Duration Duration in µs of the Gaussian shaped pulse.

Flip Angle Flip angle of the pulse. Defines the excitation pulse amplitude.

Phase Phase relative to the excitation pulse in degrees.

Gap before/after Pulse Time gap in µs before/after the pulse.

Spoiler Area Relative strength of the spoiler gradient before the saturation pulse.

Max. Peak Voltage Limitation of the maximum applied voltage for a single pulse. An exceeding leads to "ERROR_CODE_1".

All source code modifications are listed in Appendix A.1.

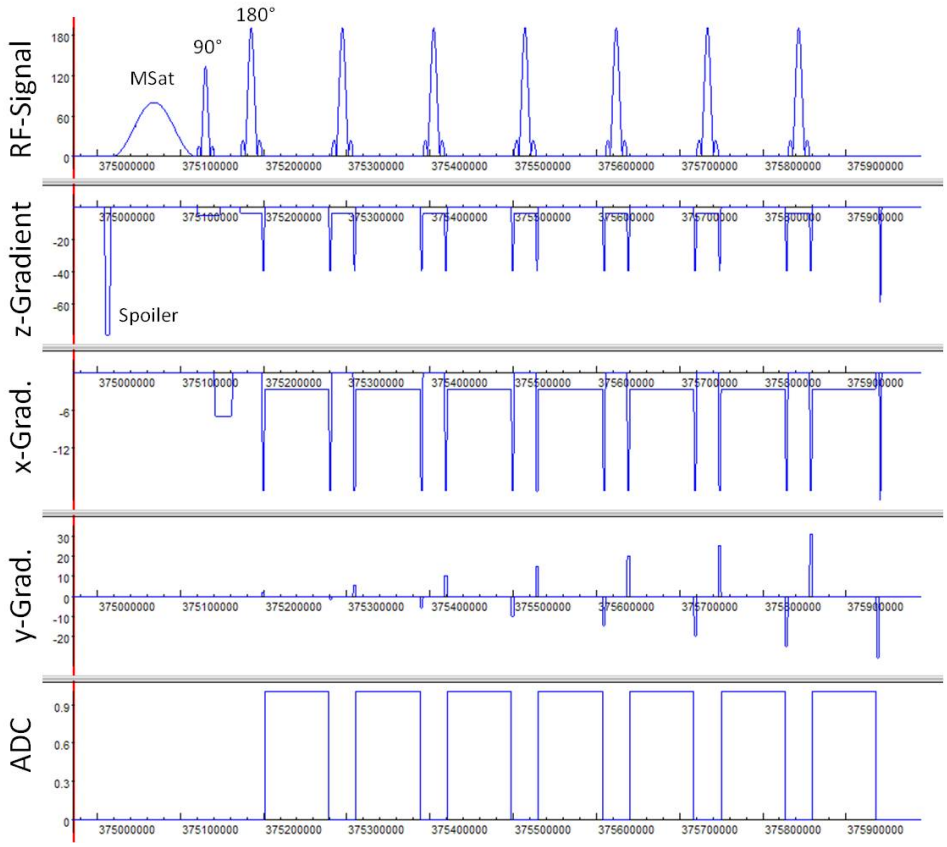

Figure 5.1.: Pulse sequence timing diagram (detail) of the modified turbo spin echo sequence ("tse_mtc"). After the saturation pulse and rf excitation, multiple 180°-rf pulses are used to continually refocus the transverse magnetisation ("turbo factor").

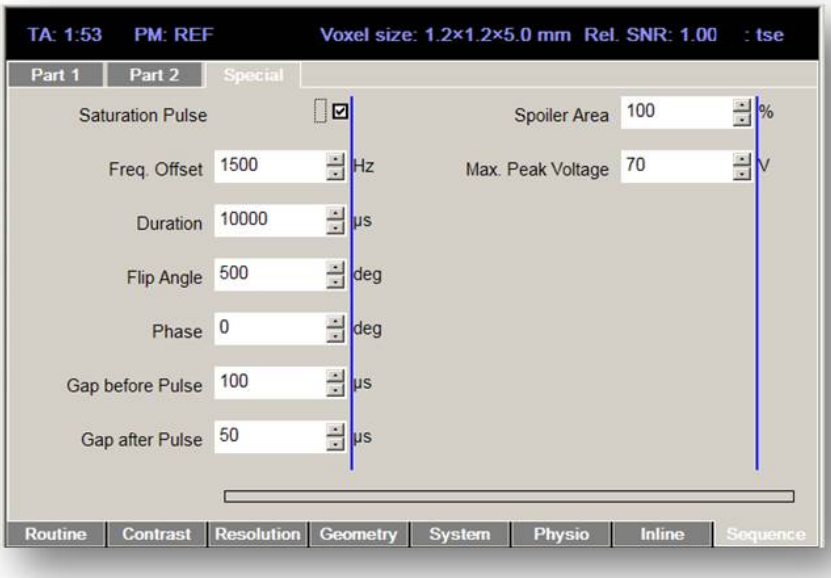

Figure 5.2.: Sequence special card of the TSE sequence with adjustable MT contrast ("tse_mtc").

5.3. Extension of the UTE Sequence

The obtained UTE source code, which is discussed in Section 4.3, was modified in order to improve the sequence performance and to extend its specifications. Hence, the chances can be structured in general extensions/improvements and the implementation of a MT spin preparation part.

5.3.1. General Changes

Initially, the sequence was limited to only 4032 radial views, which implies a severe restriction especially in spatial resolution. To avoid this limitation the following line was commented out

```
404 pSeqLim->getRadialViews().set("trufi_cv::setRadialViews", 1, 100000, 1, 64, true, 0,
        false); // Max Rad.Views default 100000
```

and replaced by

```
399 pSeqLim->setRadialViews          (1, 10000, 1, 64);
```

which enabled a maximum number of radial views of 9984 (maximum number achievable by blocks of 64 profiles). Most of the measurements were performed at this value.

Towards the end of the experimental work, the reason for the incipient limitation could be identified as a parameter "lCalcBufferSize" within the file *ReorderInfo.cpp*, which was set to 4096 by default. Increasing this value to 65536 could solve this problem (in combination with the original setting of radial views in the main cpp-file):

```
94  // TESTING
95    if (lCalcBufferSize==-1)
96    {
97        lCalcBufferSize = 65536; // default 4096
98    }
99   //TESTEND
```

Another limitation was the missing possibility to take multiple signal averages. The maximum value was raised to 20.

```
527 //TESTING
528     pSeqLim->setAverages (1, 20, 1, 1);   // Was limited to 1 average
529 //END TESTING
```

Handling various Gradient Delays

As mentioned before (Sec. 4.3), the UTE sequence is very sensitive to gradient delays. However, these delays are considered during image reconstruction. In the course of this, the sequence forwarded a specific value to the reconstruction algorithm, which depends dynamically on protocol parameters and gradient strength.
After acquisition, saved raw data can be reconstructed (icesimu) on a stand-alone PC additionally. This generates two files: an .evp-file and an .IRIS-file. Amongst others, the former contains the protocol data and the so called "WIP Memory Block", which is a work-in-progress memory slot:

```
4166 <ParamMap."sWiPMemBlock">
4167       {
4168
4169         <ParamLong."alFree">
4170         {
4171           0 1 0 0 0 0 0 0 0 0
4172           0 0 0 0 0 0 1 0 0 0
4173           0 0 0 0 0 0 0 0 0 0
4174           0 0 0 0 0 0 0 0 0 0
4175           0 0 0 0 0 0 0 0 0 0
4176           0 0 0 0 0 0 0 0 0 0
4177           0 0 0 0
4178         }
4179
4180         <ParamDouble."adFree">
4181         {
4182           <Precision> 6
4183           0.000000 0.000000 0.000000 0.000000 0.000000 0.000000 0.000000 0.000000
                0.000000 0.000000
```

```
4184            0.000000  0.000000  -0.760000  140.000000  1.000000  1.000000
4185          }
4186
4187          <ParamString."tFree">
4188          {
4189            "N4_417_VB15A_CV3DRADUTE_NIELSOD0 (Patch 0.2.2)"
4190          }
4191
4192          <ParamDouble."adRes">
4193          {
4194            <Precision> 6
4195            0.000000  0.000000  0.000000
4196          }
4197
4198          <ParamLong."lCSatBW">
4199          {
4200          }
4201        }
```

The number array denounced at "adFree" consists of 16 indices (counting $0, 1, 2, \ldots, 15$), that can be defined by the programmer. "sWiPMemBlock.adFree.12" (i. e. the 13th number) represents the gradient delay correction value (in microseconds) forwarded by the sequence. This value can be manually changed at will. A subsequent reconstruction of the raw data will than consider this new delay time.

The various gradient delays are handled within the sequence main file (*a_trufi_cv.cpp*):

```
6203  // TESTING
6204
6205  if( pMrProt->te()[0] < 500 )
6206  {
6207          //ICE_DELAY_TIME(m_pCVKernel->getTimeDelay());
6208          ICE_DELAY_TIME(m_pCVKernel->getTimeDelay() + 5.80); // Empiric offset value
6209          ICE_READOUT_RAMP_UP_TIME(m_pCVKernel->getRORampUpTime());
6210  }
6211  else if( pMrProt->te()[0] > 1000 )
6212  {
6213          ICE_DELAY_TIME(0.00); // Empiric value
6214          ICE_READOUT_RAMP_UP_TIME(m_pCVKernel->getRORampUpTime());
6215  }
6216  else
6217  {
6218          ICE_DELAY_TIME(2.50); // Empiric value
6219          ICE_READOUT_RAMP_UP_TIME(m_pCVKernel->getRORampUpTime());
6220  }
6221  cout << "TE    =   " << pMrProt->te()[0] << endl;              // Just for Debugging
6222  cout << "Delay =   " << pMrProt->wipMemBlock().adFree[12] << endl;
6223
6224
6225  //TESTING END
```

The protocol specific delay time is given by "getTimeDelay()". Here, the gradient delay τ was set for 3 different TE intervals:

$$\tau = \begin{cases} \text{getTimeDelay}() + 5.8 & \text{for TE} < 0.5\,\text{ms} \\ 2.5 & \text{for } 0.5\,\text{ms} \leq \text{TE} \leq 1.0\,\text{ms}\,, \\ 0.0 & \text{for TE} > 1.0\,\text{ms} \end{cases} \tag{5.1}$$

where the numerical values are entirely empirical evaluated from quantitative analysis of image blurring and visual inspection of image quality (see Sec. 6.3). The single intervals were chosen arbitrarily.

5.3.2. Implementation of a MT Spin Preparation

By default the option for MT contrast within the UTE sequence was not implemented. In order to enable the standard (SBB) MTC to the protocol UI a single line was added:

```
344  // TESTING
345  // add Magnetization Transfer Contrast
346  pSeqLim->setMTC   (SEQ::OFF, SEQ::ON); // MTC SBB (Gauss, 10ms, 1200Hz off-res.)
347  // TEST END
```

This produced a selectable checkbox on the Contrast card (Fig. 5.3(a)). However, this procedure is quite static, since important pulse parameters like frequency offset, pulse shape and duration are fixed (see Sec. 5.2). Therefore, the Sequence/Special card was expended in order to allow the user the main adjustments.
The two new parameters "MTC_OFFSET_FACTOR" and "MTC_DURATION_FACTOR" were declared in the header file *a_trufi_CV_UI.h*:

```
152  enum WIP_DOUBLE_PARAMETERS
153  {
154  //  WIP_DOUBLE_DELAY_BALANCE                    =   0,
155  WIP_DOUBLE_MTC_DURATION_FACTOR      =   10,
156  WIP_DOUBLE_MTC_OFFSET_FACTOR        =   11,
157  WIP_DELAY_TIME                      =   12, //Readout Delay and RampUpTime for UTE Ice
         Program
158  WIP_READOUT_RAMP_UP_TIME            =   13,
159  WIP_DOUBLE_FILTER_FACTOR            =   14,
160  WIP_DOUBLE_SCALE_FACTOR             =   15
161
162  };
```

The numbers indicates the WIP parameter array index. Moreover, the following changes were performed within this file:

String definition:

```
194 #define WIP_LABEL_MTC_OFFSET_FACTOR          "MT Frequency Offset"
195 #define WIP_LABEL_MTC_DURATION_FACTOR        "MT Pulse Duration"
```

Definitions to create WIP boxes at a specific location on the sequence special card:

```
202 #define WIP_CREATE_TAG_MTC_OFFSET_FACTOR  (_create< LINK_DOUBLE_TYPE >(pSeqLim,
        MR_TAG_SEQ_WIP14,  WIP_DOUBLE_MTC_OFFSET_FACTOR ) )
203 #define WIP_CREATE_TAG_MTC_DURATION_FACTOR  (_create< LINK_DOUBLE_TYPE >(pSeqLim,
        MR_TAG_SEQ_WIP13,  WIP_DOUBLE_MTC_DURATION_FACTOR ) )
```

Definitions of macros to initialize WIP boxes:

```
210 #define WIP_INIT_MTC_OFFSET_FACTOR  ((pMrProt->wipMemBlock().adFree[
        WIP_DOUBLE_MTC_OFFSET_FACTOR] ) = 500.0 )
211 #define WIP_INIT_MTC_DURATION_FACTOR  ((pMrProt->wipMemBlock().adFree[
        WIP_DOUBLE_MTC_DURATION_FACTOR] ) = 9984.0 )
```

Definitions to check WIP parameter:

```
219 #define IS_MTC_OFFSET_NOTINITIALIZED  ((pMrProt->wipMemBlock().adFree[
        WIP_DOUBLE_MTC_OFFSET_FACTOR] ) == 0.0 )
220 #define IS_MTC_DURATION_NOTINITIALIZED  ((pMrProt->wipMemBlock().adFree[
        WIP_DOUBLE_MTC_DURATION_FACTOR] ) == 0.0 )
```

Now, these definitions could be used within *a_trufi_CV_UI.cpp* (only added lines are shown):

```
8040 static const char pszLabelMOF[]  = WIP_LABEL_MTC_OFFSET_FACTOR;
8041 static const char pszLabelMDF[]  = WIP_LABEL_MTC_DURATION_FACTOR;

8095  case WIP_DOUBLE_MTC_OFFSET_FACTOR:
8096         arg_list[0] = (char*) pszLabelMOF;
8097         break;
8098  case WIP_DOUBLE_MTC_DURATION_FACTOR:
8099         arg_list[0] = (char*) pszLabelMDF;
8100         break;
```

The following defines the text behind the sequence/special card box:

```
8082 static const char pszUnitFrequency[]    = "Hz";
8083 static const char pszUnitTime[]         = "us";
8084 static const char pszUnitTime2[]        = "ms";

8095 case WIP_DOUBLE_MTC_OFFSET_FACTOR:
8096         arg_list[0] = (char*) pszUnitFrequency;
8097         break;
8098 case WIP_DOUBLE_MTC_DURATION_FACTOR:
8099         arg_list[0] = (char*) pszUnitTime;
8100         break;
```

The valid ranges of the new parameters were defined from 0 Hz to 1500 Hz in increments of 1 Hz for the frequency offset and from 0.001 ms to 19.968 ms in steps of 64 µs for the

pulse duration:

```
8130  case WIP_DOUBLE_MTC_OFFSET_FACTOR:
8131          dMin = 0; dMax = 1500; dInc = 1;
8132          break;
8133  case WIP_DOUBLE_MTC_DURATION_FACTOR:
8134          dMin = 64; dMax = 19968; dInc = 64;
8135          break;
```

Now there is a need to declare the function, which gets/sets the entered value from the box.

```
8171  case WIP_DOUBLE_MTC_OFFSET_FACTOR:
8172          dRetVal = pMrProt->wipMemBlock().adFree[lIndex];
8173          break;
8174  case WIP_DOUBLE_MTC_DURATION_FACTOR:
8175          dRetVal = pMrProt->wipMemBlock().adFree[lIndex];
8176          break;

8207  case WIP_DOUBLE_MTC_OFFSET_FACTOR:
8208          pMrProt->wipMemBlock().adFree[lIndex] = dValue;
8209          break;
8210  case WIP_DOUBLE_MTC_DURATION_FACTOR:
8211          pMrProt->wipMemBlock().adFree[lIndex] = dValue;
8212          break;
```

Next, the “tool tip” appearing while the cursor rolls over the box is configured:

```
8296  case WIP_DOUBLE_MTC_OFFSET_FACTOR:
8297          //sprintf(tLine,  "MT Offset Frequency"); strcat(tToolTip,tLine);
8298          sprintf(tLine,"\nOffset Frequency of the Magn. Transfer Pulse");  strcat(
                  tToolTip,tLine);
8299          arg_list[0] = tToolTip;
8300          lRetVal = MRI_STD_STRING;
8301          break;
8302  case WIP_DOUBLE_MTC_DURATION_FACTOR:
8303          //sprintf(tLine,  "MT Pulse Duration"); strcat(tToolTip,tLine);
8304          sprintf(tLine,"\nDuration of the Magn. Transfer Pulse");  strcat(tToolTip,tLine
                  );
8305          arg_list[0] = tToolTip;
8306          lRetVal = MRI_STD_STRING;
8307          break;
```

And finally, the WIP parameters need to be initialised and registered:

```
8755  if (IS_MTC_OFFSET_NOTINITIALIZED)
8756          {
8757                  if(pSeqLim->isContextPrepForMrProtUpdate()) {
                          WIP_INIT_MTC_OFFSET_FACTOR;} else {return false;}
8758          }
8759
8760  if (IS_MTC_DURATION_NOTINITIALIZED)
8761          {
8762                  if(pSeqLim->isContextPrepForMrProtUpdate()) {
                          WIP_INIT_MTC_DURATION_FACTOR;} else {return false;}
8763      }

9872  if (LINK_DOUBLE_TYPE* pDoubleWIP = WIP_CREATE_TAG_MTC_OFFSET_FACTOR)
9873      {
9874          pDoubleWIP ->registerGetLabelIdHandler   (WIP_DOUBLE_GetLabelId  );
```

```
9875            pDoubleWIP ->registerGetLimitsHandler    (WIP_DOUBLE_GetLimits   );
9876            pDoubleWIP ->registerGetValueHandler     (WIP_DOUBLE_GetValue    );
9877            pDoubleWIP ->registerSetValueHandler     (WIP_DOUBLE_SetValue    );
9878            pDoubleWIP ->registerGetPrecisionHandler (WIP_DOUBLE_GetPrecision);
9879            pDoubleWIP ->registerGetUnitIdHandler    (WIP_DOUBLE_GetUnitId   );
9880            pDoubleWIP ->registerGetToolTipIdHandler (WIP_DOUBLE_GetToolTipId);
9881            pDoubleWIP ->registerIsAvailableHandler  (WIP_DOUBLE_IsAvailable );
9882            }
9883
9884            if (LINK_DOUBLE_TYPE* pDoubleWIP = WIP_CREATE_TAG_MTC_DURATION_FACTOR)
9885        {
9886            pDoubleWIP ->registerGetLabelIdHandler   (WIP_DOUBLE_GetLabelId  );
9887            pDoubleWIP ->registerGetLimitsHandler    (WIP_DOUBLE_GetLimits   );
9888            pDoubleWIP ->registerGetValueHandler     (WIP_DOUBLE_GetValue    );
9889            pDoubleWIP ->registerSetValueHandler     (WIP_DOUBLE_SetValue    );
9890            pDoubleWIP ->registerGetPrecisionHandler (WIP_DOUBLE_GetPrecision);
9891            pDoubleWIP ->registerGetUnitIdHandler    (WIP_DOUBLE_GetUnitId   );
9892            pDoubleWIP ->registerGetToolTipIdHandler (WIP_DOUBLE_GetToolTipId);
9893            pDoubleWIP ->registerIsAvailableHandler  (WIP_DOUBLE_IsAvailable );
9894            }
```

The result of these modifications are shown in Figure 5.3(b). The checkbox in the Contrast card enables a preceding saturation pulse (Fig. 5.3(a)), the two new boxes in the Sequence/Special card register two values, which are stored within the WIP parameter array on index number 10 (frequency offset) and 11 (pulse duration). In order to relate these parameters with the actual MT pulse, some further changes were done within the *SBBMSat.cpp* file:

```
118 // TESTING
119 else if ( getNominalBZero() > 2.5 )
120     {
121         RF_Duration     = static_cast<long>(pMrProt->wipMemBlock().adFree[10]);
122 //      cout << "\n\n RF_Duration = " << RF_Duration << "\n\n";
123
124         setFrequencyOffset(pMrProt->wipMemBlock().adFree[11]);
125
126 //      RF_Duration     = static_cast<long>(RFP_DURATION_MSAT * 1.3);
127
128 //      setFrequencyOffset(1200);
129
130         m_lPostTime = static_cast<long>(160 + RFP_DURATION_MSAT * 0.5);
131
132
133 //      m_lPostTime = static_cast<long>(160 + pMrProt->wipMemBlock().adFree[10] * 0.5);
134     }
135 // TESTEND
```

Here, “pMrProt→wipMemBlock().adFree[10/11]” points directly on the corresponding index number of the WIP parameter array.

The MT-pulse always precedes a block of excitation pulses, which size can be defined by the user by changing the number of segments n ($n \in \mathbb{N}$). For example if $n = 8$, the number of profile excitations after a single MT-saturation pulse equals eight (see Fig. 5.4).

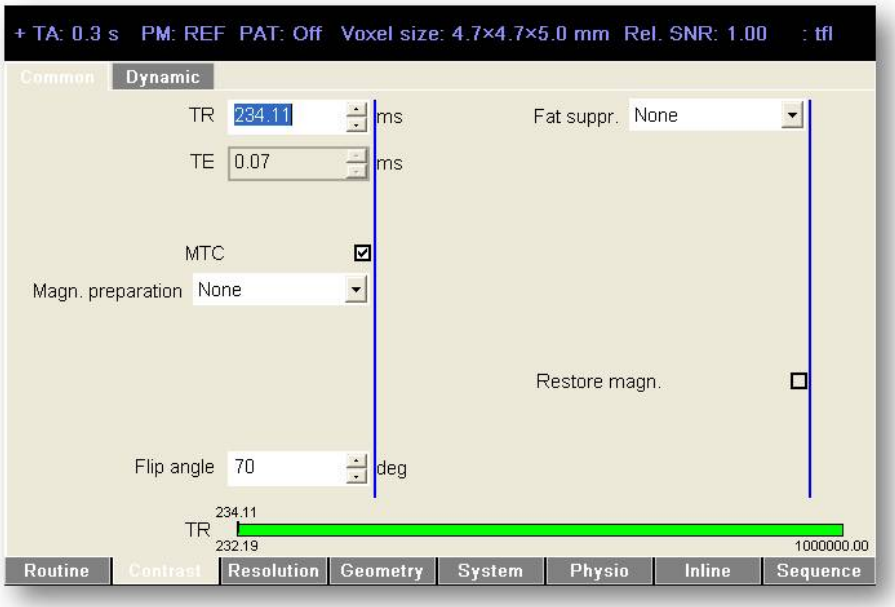

(a)

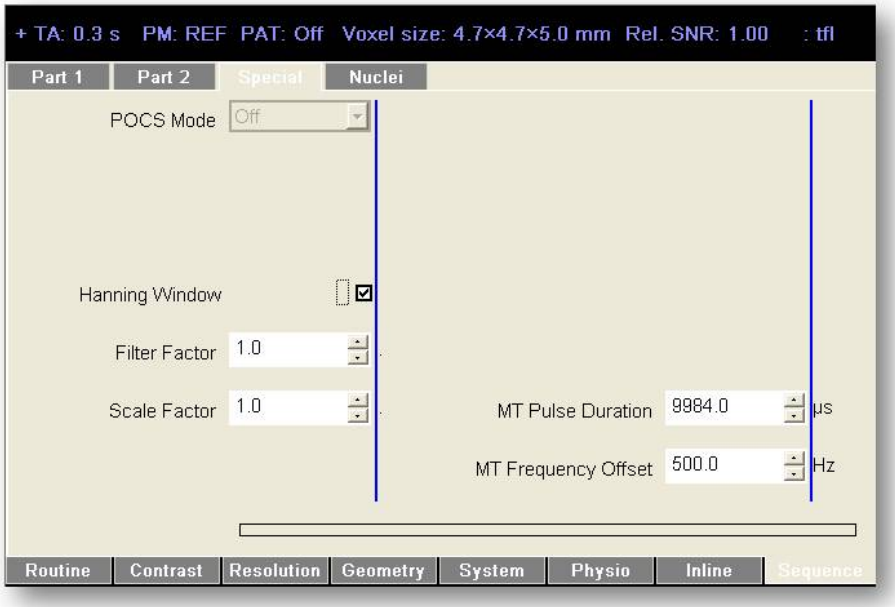

(b)

Figure 5.3.: UTE user interface: Contrast card with selectable MT Contrast (a) and Sequence/Special card with adjustable MT duration as well as frequency offset (b).

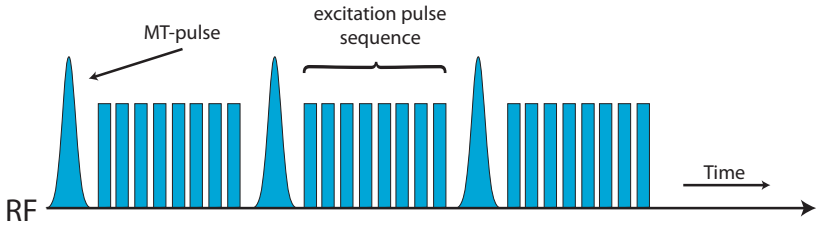

Figure 5.4.: Schematic pulse diagram. Each MT-saturation pulse can precede a number of segments n ($n \in \mathbb{N}$).

5.4. Image Processing

5.4.1. Spatial Resolution

The spatial resolution of the experimental set-up, including hard- and software, can be expressed by a quantity known as the modulation transfer function (MTF). The MTF is defined as the ratio of modulation M (or contrast) in the image to that in the object, which is a function of the spatial frequency ξ:

$$\mathrm{MTF}(\xi) = \frac{M_{img}(\xi)}{M_{obj}(\xi)}. \tag{5.2}$$

Generally, the MTF is a decreasing function of spatial frequency and normalised to one (see Fig. 5.5). As a general rule, the accessible resolution corresponds to the spatial frequency where the MTF equals 0.5, i. e. contrast is down to half. The spatial frequency in turn conforms to the reciprocal of the spatial period length.

Determining the MTF

Basically, there are two ways determining the MTF:

1. Direct contrast measurement by using a grating object of different grating periods giving the MTF value at discrete spatial frequencies.

2. Measurement of the line spread function (LSF) or the edge response. The MTF can than be found by taking the one-dimensional FFT of the LSF at continuous spatial frequencies.

The latter method was realised to determine the MTF. For this purpose, a phantom consisting of a thin glass capillary in water (Fig. 4.4(b)) was used to measure the inverse

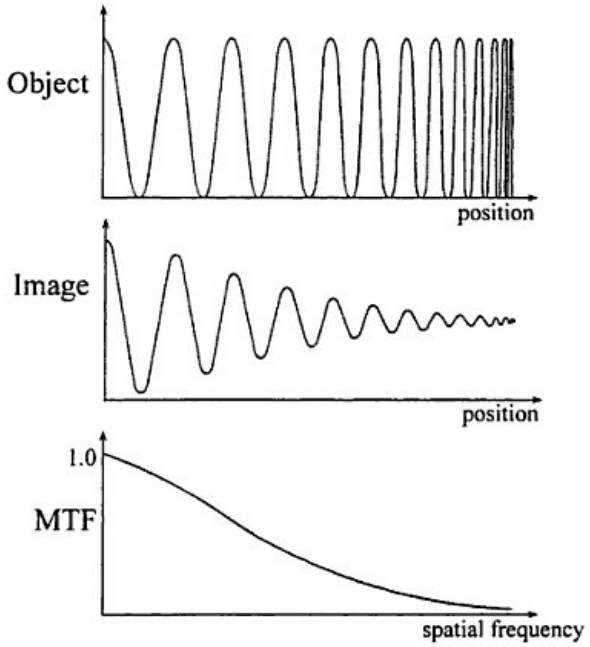

Figure 5.5.: Decreasing image modulation depth with increasing spatial frequency and corresponding modulation transfer function (MTF) (Boreman, 2001).

point spread function (PSF) approximatively.
Due to the natural line broadening of more solid materials, the achievable resolution should be reduced. Therefore the resolution phantom shown in Figure 4.4(a) was appropriated as a PSF-model providing an evaluation of spatial resolution for short-T2 materials.
The LSF could be directly obtained from the PSF by taking a single row of pixels (line profile), i. e. the pixel values along a line drawn across the center of the PSF. This was done by using the image processing program "ImageJ" (v1.43u).
The advantage of using the PSF is that it contains information in all in-plane directions and the LSF can be chosen in one specific direction arbitrarily. Since the UTE pulse sequence is a radial sequence, usually the spatial resolution was examined in a radial and a corresponding normal direction (see Fig. 5.6).
In order to allow a statistical evaluation, the line profiles were taken for seven different slices of the same measurement. Then the data, which contains distance information and signal amplitude, was manually processed within a Microsoft Excel sheet featuring signal inversion (if necessary) and offset correction. Multiple lines were obtained with global maxima at position zero, which were saved into an ASCII-formatted text file.

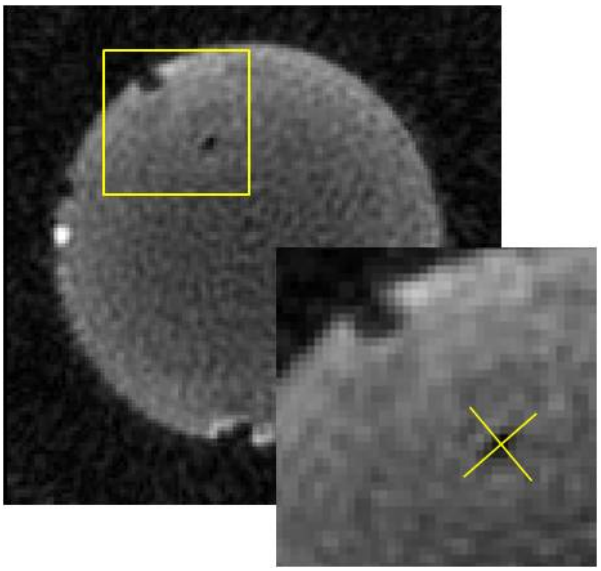

Figure 5.6.: Image processing in order to determine the MTF. The inverse PSF was measured and the LSF (line profiles) was examined in two directions: radial and normal (picture detail).

Subsequently, the data (position and 7 line profiles) could be read by a MATLAB script (m-file) for further processing.
The m-file appraises the line profiles by calculating the MTF as the Fourier transformed of the LSF. Here the correct transformation of spatial dimensions to spatial frequencies should be considered. As a lower most frequency one has

$$\nu_{min} = \frac{1}{l}, \tag{5.3}$$

where l is the length of the line profile and as a cut-off frequency (Nyquist frequency)

$$\nu_{max} = \frac{1}{2T} = \frac{n_p}{2l}, \tag{5.4}$$

where T is the interval between sampling points and n_p is the number of samples per profile.
The spatial resolution was then determined as the reciprocal value of the spatial frequency at a modulation of 50 percent. This was done for every single line profile (slice) resulting in a mean value and standard deviation.

The full m-file can be found in Appendix A.2.

A similar analysis was done additionally using a short-T2 phantom (Fig. 4.3(a)) as a knife-edge test object. Here the edge spread function (ESF) could be measured as a line profile over the edge of the object. The LSF can be derived from the ESF as the first derivative (Boreman, 2001):

$$\mathrm{LSF}(x) = \frac{d}{dx}\mathrm{ESF}(x). \tag{5.5}$$

The remaining analysis was then carried out by analogy with the discussion above.

5.4.2. Analysis of Edge Enhancement

During the analysis of quality control measurements, an objective and automated method to identify feasible edge enhancements artefacts was required. For this purpose, the Hot Melt Adhesive (HMA)-in-water phantom was used, shown in Figure 4.3(b), and a line profile was taken from the water region (Fig. 5.7(a)).

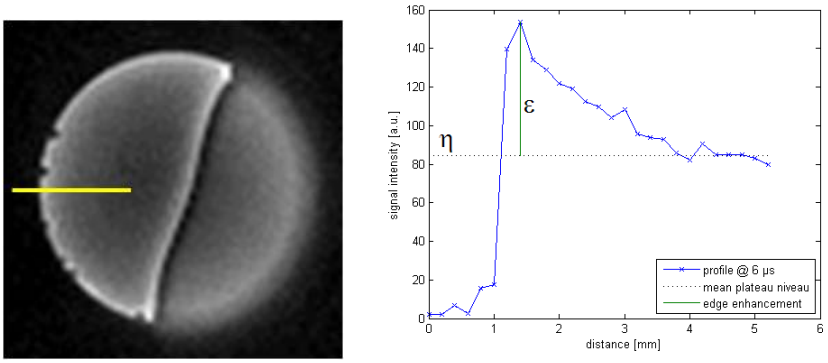

(a) (b)

Figure 5.7.: Analysis of edge enhancement: (a) A line profile from the water region. (b) Definition of the absolute signal enhancement.

In order to find a quantity of edge enhancement, a plateau niveau was defined as the average level of the homogeneous water signal η at the right end of the profile (cf. Fig. 5.7(b), dashed line). The absolute signal enhancement ϵ is consequently given by the difference of signal S_{edge} at the phantom's edge and the plateau niveau:

$$\epsilon = |S_{edge} - \eta| \tag{5.6}$$

The relative magnitude of edge enhancements was defined as the signal enhancement referred to the plateau niveau:

$$\epsilon_{rel} = \frac{\epsilon}{\eta} \tag{5.7}$$

A corresponding (exemplary) m-file can be found in Appendix A.3.

Determination of the optimal Gradient Delay Time

As discussed in Section 5.3.1, raw data could be reconstructed at different gradient delay times. In order to compare images obtained in this way regarding edge enhancement, a dedicated Matlab routine was written. The m-file listed in Appendix A.3 combines the edge enhancement detection and quantification of a data set containing line profiles from images reconstructed at different gradient delay times and the subsequent determination of an optimal delay correction. In order to do this, the routine looks for the delay time, which corresponds to a vanishing relative edge enhancement. For a more precise definition of the optimal delay time, a linear interpolation was performed between two measured points.
In the case of longer detection times ($> 0.07\,\mathrm{ms}$), due to time constraints the analysis was performed more qualitative. Here the edge enhancement was validated subjectively by eye under variation of gradient delay correction.

Part III.

Results and Discussions

Chapter 6

Quality Control

6.1. General UTE Sequence Performance

For stated reasons, some materials have such short T2s that they produce little or no detectable signal whilst the use of conventional pulse sequences like turbo spin echo (TSE). In contrast, UTE sequences gives the opportunity to visualise these materials. A phantom which clarifies the difference is the HMA-in-water phantom depicted in Figure 4.3(b) featuring a shot- and long-T2 material side-by-side.
Figure 6.1 shows a direct comparison of a TSE and UTE sequence. In contrast to the conventional TSE sequence with a detection time of about 7.8 ms on the left, the HMA is clearly visible using the UTE sequence (TE = 0.07 ms).

A method to contrast short-T2 materials is to subtract a measurement with a short detection time from a measurement with a higher detection time. Since the signal from short-T2 materials decays much faster than e. g. a bulk water signal, the resulting difference, or subtraction image only contains information about short-T2 materials. Figure 6.2 shows this method using the same phantom and for all three sectional planes. The image calculation was done using ImageJ.

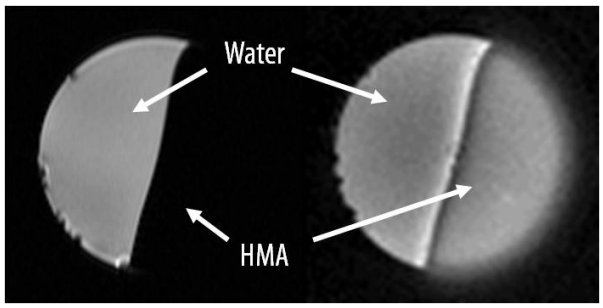

Figure 6.1.: Comparison UTE/TSE using a HMA-in-water phantom: Left: Turbo spin echo (TSE) sequence. Sequence parameters: FOV $20 \times 20\,\mathrm{mm}$, TR = 4000 ms, TE = 7.8 ms, Matrix Size = 128×64. Right: UTE sequence. FOV $20 \times 20\,\mathrm{mm}$, TR = 254 ms, TE = 0.07 ms, $\alpha = 5°$, BW = $558\,\mathrm{Hz\,px^{-1}}$, $N = 64$, $N_{proj} = 40000$. Gradient delay optimised.

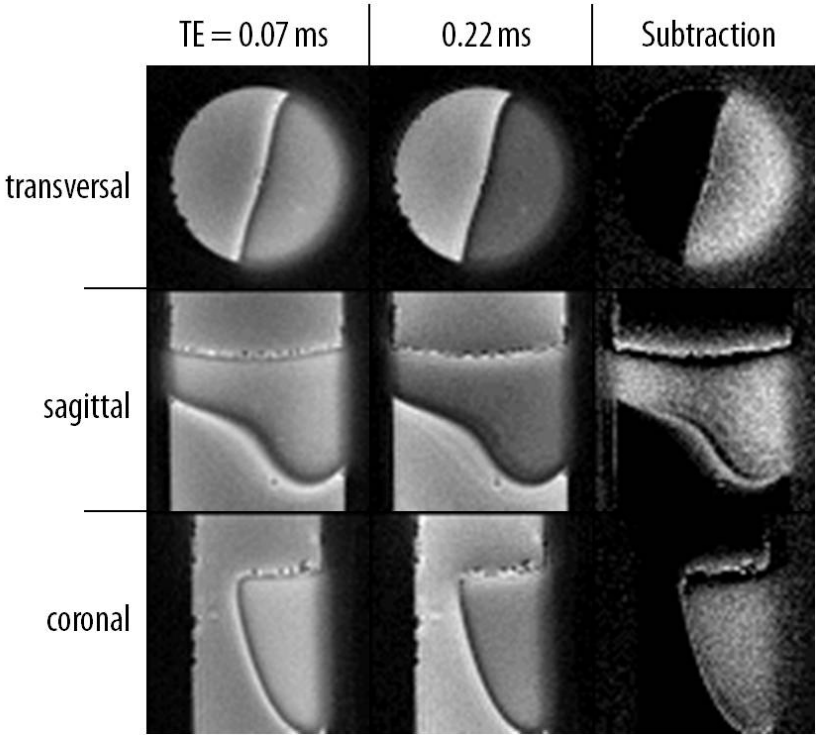

Figure 6.2.: UTE measurement using a HMA-in-water phantom: The measurement was done for all three sectional planes (transversal, sagittal and coronal) and with two different detection times TE (0.07 ms and 0.22 ms). The third column represents the subtraction image ($\mathrm{TE}_{0.07\,\mathrm{ms}}$ minus $\mathrm{TE}_{0.22\,\mathrm{ms}}$). Remaining parameters identical with Figure 6.1.

6.2. Investigations on Image Blurring and Edge Enhancement

Image Blurring

First measurements using the *CVUTE_417** sequence showed a remarkable image blurring relative to common TSE obtained images. There are several possible causes for this phenomenon, which in parts come into effect simultaneously.

First of all, there is a significant correlation to the density of sampled data, i. e. the number of samples per profile N relative to the number of total profiles N_{proj}.
Figure 6.3 shows six measurements of an agar-phantom featuring different base resolutions while the radial views are constant ($N_{proj} = 4096$). It can be seen, that the image blurring increases with base resolution significantly.

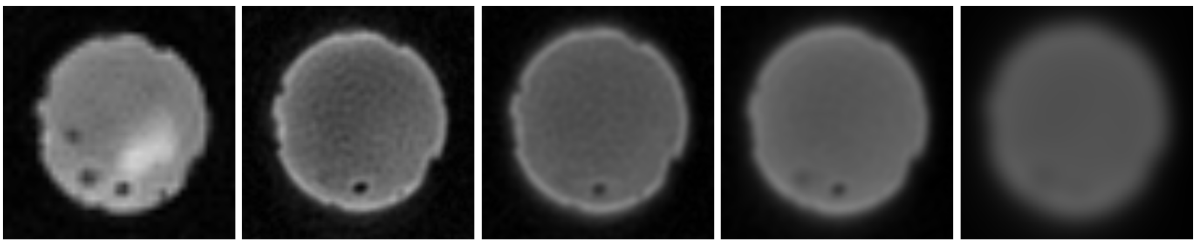

Figure 6.3.: Image quality as a function of base resolution N demonstrated on a agar-phantom. While the number of radial views is constant ($N_{proj} = 4096$) the image blurring increases with N (64-512). FOV: $24 \times 24\,\mathrm{mm}$, TR = 262 ms, TE = 0.07 ms, $\alpha = 5°$, BW = $558\,\mathrm{Hz\,px^{-1}}$.

According to the Nyquist-Shannon sampling theorem, it can be shown (Boada et al., 1997), that sampling efficiency in three dimensional radial imaging is optimal if

$$N_{proj} = 4\pi \cdot L^2 k_{max}^2 = 4\pi \cdot N^2, \tag{6.1}$$

* This sequence is a further developed Siemens WIP package and somewhat more advanced than the later obtained UTE source code. However, the results regarding this, more recent version should be comparable with the older one.

where L is size of the Field of View (FOV) and k_{max} the maximum spatial frequency. This estimate is based on the Nyquist condition stating that the distance between adjacent sample points in k-space should be equal to the inverse size of the FOV.

An important issue of radial sequences is that data is acquired more dense in the center of k-space. As a consequence, without compensation this leads to a significant image blurring, since low spatial frequencies become highly overweighted. However, the pre-compensation of undersampling at outer k-space, or oversampling at inner k-space respectively, is actually done in the sequence. Here, every data point is multiplied by a density compensation function (rho-filter), which is similar to a high-pass filter. Nevertheless, these density compensation could be suboptimal in some cases (Nielles-Vallespin et al., 2009; Nielles-Vallespin, 2004).

Another reason, which can induce blurring is the process of regridding. At larger matrix sizes, i. e. larger base resolution, the relative distances at the outer k-space lead to a higher probability of interpolation errors resulting in a loss of spatial information at abrupt spatial changes in the image, such as edges and fine details generally.
The same principle is shown in Figure 6.4. Here, the base resolution is held constant while the number of profiles is varied. At a reduced number of profiles, the typical radial streaking artefacts appear, which are due to an angular undersampling in radial imaging (Scheffler and Hennig, 1998; Peters et al., 2000).
An agar-phantom is sampled with $N = 64$ and $N = 128$ at three different numbers of radial views. The figure on the right shows the signal intensity of a line profile drawn over the edge of the phantom for every measurement. Beside an intense edge enhancement, one can perceive an increased blurring at the fewest profile number. This is more pronounced for the higher base resolution. Moreover, there is nearly no distinction in blurring between the mediate and high number of radial views.

A general issue of radial sequence, which contribute to image blurring, is the relatively strong liability to off-resonance effects like chemical shifts, B_0 inhomogeneities and magnetic susceptibility (Smith and Nayak, 2010). This problem is depicted in Figure 6.5 showing a homogeneous agarose-phantom. Figure 6.5(a) is sampled at the precise resonance frequency, while Figure 6.5(b) is frequency shifted by 1.3 kHz off-resonant. This frequency offset results in k-space trajectory errors and a misinterpretation of spatial

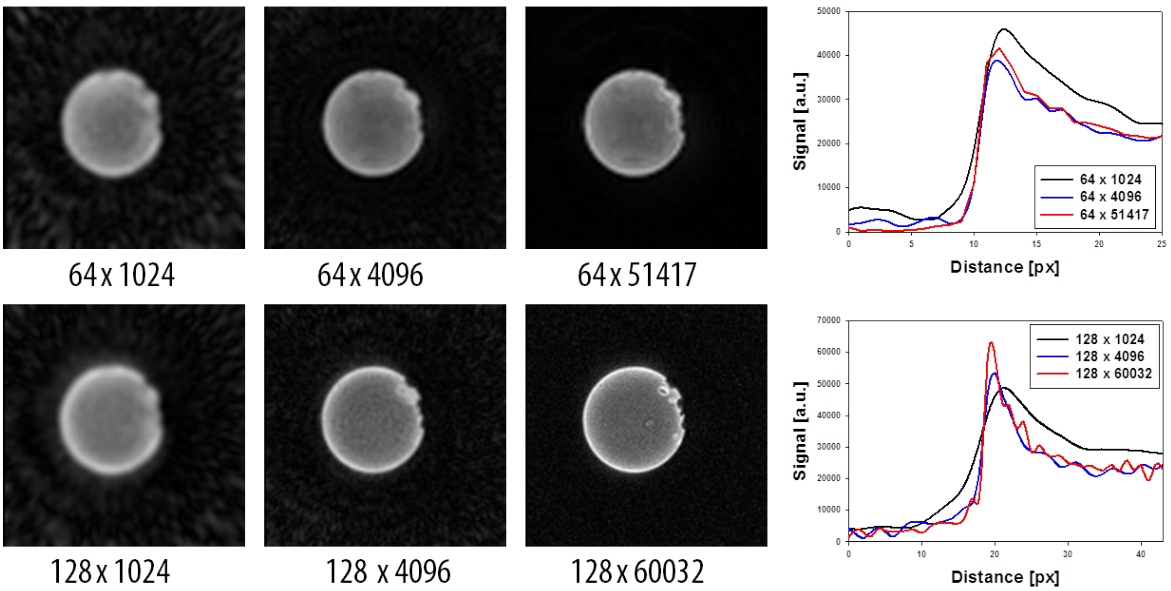

Figure 6.4.: Agar-phantom sampled with $N = 64$ (top) and $N = 128$ (bottom) at three different numbers of radial views increasing from left to right. The plot on the right shows the signal intensity of a line profile drawn over the edge of the phantom for every measurement. FOV: $24 \times 24\,\mathrm{mm}$, TR $= 262\,\mathrm{ms}$, TE $= 0.07\,\mathrm{ms}$, $\alpha = 5°$, BW $= 128\,\mathrm{Hz\,px^{-1}}$.

positions in the image reconstruction, since every single profile is shifted systematically by a certain value. The sample in Figure 6.5 can be interpreted as the image PSF representing the image convolution kernel. A resonance frequency offset therefore leads to an image blurring.

In addition, the repetition time TR should be ideally set to the shortest possible value. As mentioned in Section 4.3 within the time interval TR a certain number of RF excitations and profile acquisitions are performed (64 by default). Due to small flip angles and rapid repetition, the magnetisation reaches a steady state after an uncertain number of excitation pulses. Too long chosen TRs lead to a dead time added by the sequence before further profiles are measured. Within this dead time the magnetisation will relax and destroy the steady state. The next profiles, which are necessary to reproduce the steady state will contribute with a lower signal intensity. Probably this imbalance of profile signal intensity may lead to a reduced image quality.

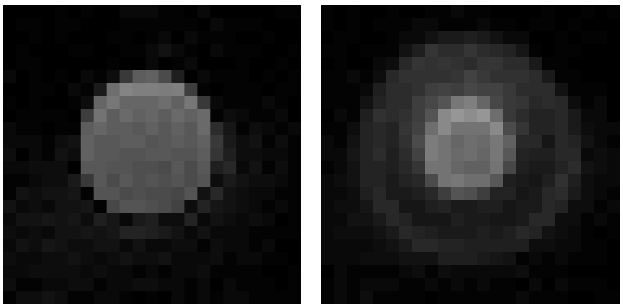

(a) (b)

Figure 6.5.: Image Blurring due to a resonance frequency offset. (a): Agarose-phantom at the precise resonance frequency (cropped image). (b): Off-resonance artefact due to an inadequate frequency adjustment ($\Delta = 1.3\,\mathrm{kHz}$).

Aside from that, the properties of the sample itself can essentially contribute to image quality. Materials with a majority of short-T2 components are characterised by a broadened line width. This requires a receiver bandwidth per pixel (BW) of at least this line width in order to resolve finer structures. Furthermore, materials with very short T2s could decay extremely rapidly during the acquisition window (Nielles-Vallespin et al., 2007). Since typically the k-space is sampled from lower to higher frequencies, the signal might have already been weakened at outer k-space regions. This in turn corresponds to an enhanced image blurring. Here, a higher BW is advantageous, too, since it is in-

versely proportional to the sampling rate and therefore to the acquisition time window.

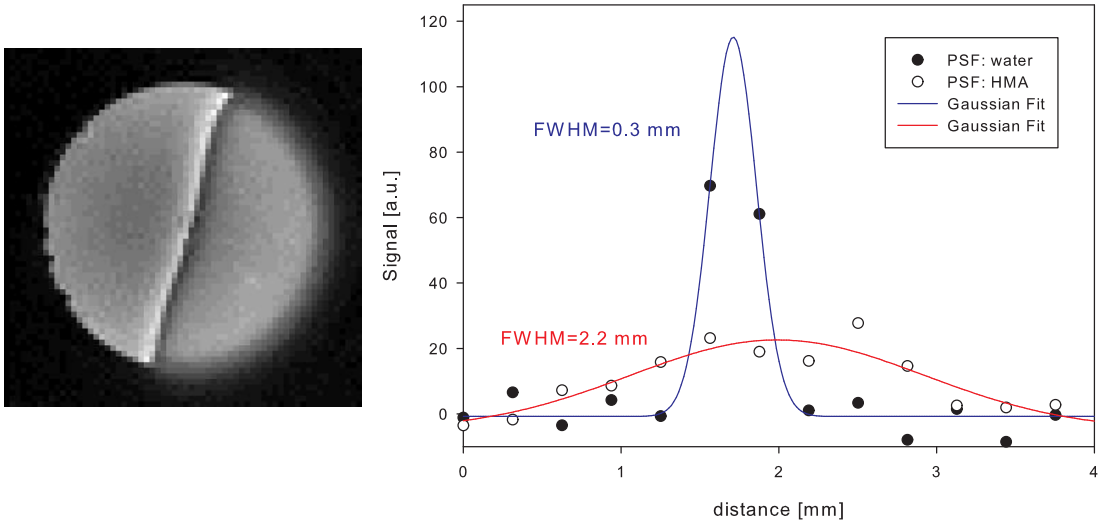

(a) (b)

Figure 6.6.: Image blurring also depends on material properties. (a): Transversal slice of a phantom containing a hot melt adhesive (right) and water (left). The blurring is significantly stronger on the HMA-side. FOV: $25 \times 25\,\text{mm}$, TE $= 0.07\,\text{ms}$, $N = 64$, $N_{proj} = 40000$, BW $= 558\,\text{Hz}\,\text{px}^{-1}$. (b): LSF of both materials evaluated by taking the first derivative of the edge spread function (ESF). The data is fitted by a Gaussian function. The full width at half maximum (FWHM) of the curve is a measure for image blurring.

Figure 6.6(a) shows a transversal slice of the already familiar phantom containing a hot melt adhesive (HMA) and water (Fig. 4.3(b)). The difference in blurring appearing in the respective material can be seen clearly. In order to quantify this effect, the LSF was evaluated by taking the first derivative of the edge spread function (ESF) (Equ. 5.5). The result is plotted in Figure 6.6(b). Here, the data is fitted by a Gaussian function and the full width at half maximum (FWHM) is calculated based on this fit. The data shows a significant broader LSF for the HMA material ($\text{FWHM}_{HMA} = 2.2\,\text{mm}$) than for water ($\text{FWHM}_{H_2O} = 0.3\,\text{mm}$).

The reason for this blurring is primarily attributed to the very short-T2 material in combination with insufficient strong gradients. Figure 6.7 shows a frequency spectrum of a pure HMA phantom*. The line is broadened to approximately 586 Hz (FWHM,

* Same material, but no surrounding water (Fig. 4.3(a)).

obtained by STEAM measurement). The receiver BW during this measurement was only 558 Hz px^{-1} providing a deficient frequency resolution and thus additional image blurring. Moreover, the rapid decay of signal, which can be estimated to be

$$\text{FWHM} = \frac{1}{T2*} \qquad \Rightarrow \qquad T2* \approx 1.7\,\text{ms}, \tag{6.2}$$

and the available acquisition window governed by the BW, is on the same scale. Other measurements on this phantom with decreasing detection times result in even shorter T2*s in the order of 0.2 ms (cf. Appendix A.4). In other words, a significant fraction of signal is already decayed while sampling the outer k-space. This loss of information leads to further blurring.

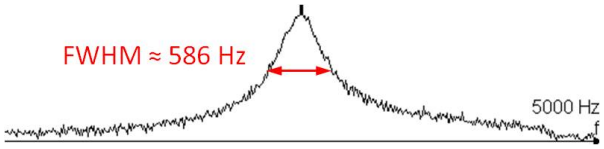

Figure 6.7.: Frequency spectrum of a pure HMA phantom obtained by STEAM measurement. The line is broadened to approximately 586 Hz (FWHM).

The image blurring can also be affected by hardware imperfections. Since this 3D radial sequence is highly sensitive to gradient performance, effects like pre-emphasis, cross-coupling and eddy currents, as well as time switching delays could have a large influence on image quality. All these effects lead to spatial deviations in the magnetic gradient field, or to actual gradients which are shifted in time from the requested ones. Basically gradient delays can be corrected before image reconstruction by an addition of a certain compensatory gradient prephaser previous to read-out gradient (cf. Peters et al., 2003). However, in order to achieve shortest detection times this is not an option for UTE sequences. For that reason gradient delay correction is done during image reconstruction.

Edge Enhancement

Beside blurring, another negative impact on image quality is the conspicuous edge enhancement. Herein, it is apparent that signal from the inner part of the sample is shifted outwards leading to a hypointense edge region and a hypotensive centre.

It turned out that this artefact is due to an insufficient gradient performance (espe-

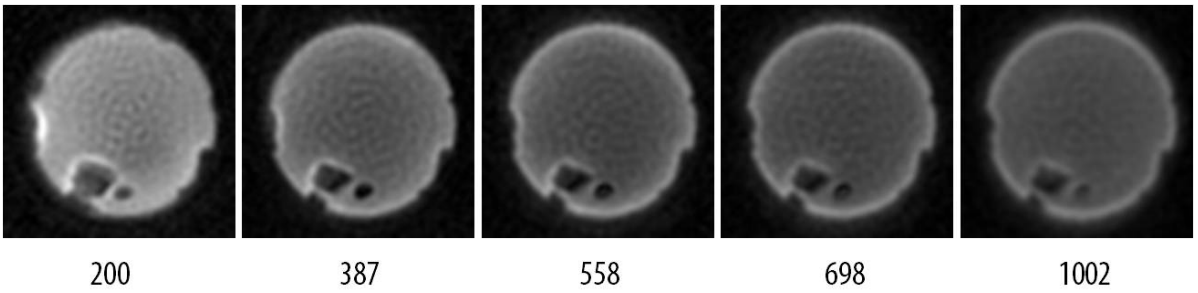

Figure 6.8.: Edge enhancement measurement at different receiver bandwidths increasing from left to right (values in $\left[\mathrm{Hz\,px^{-1}}\right]$). Agar-phantom. FOV: $24 \times 24\,\mathrm{mm}$, TR $= 262\,\mathrm{ms}$, TE $= 0.07\,\mathrm{ms}$, $\alpha = 5°$, $N = 128$, $N_{proj} = 4096$.

cially in time domain). Thus, it should also depend on gradient strength. Figure 6.8 shows a series of measurements on an agar-phantom with different receiver bandwidths increasing from left to right. The edge enhancement was evaluated as described in Section 5.4.2. The single line profiles are listed in Figure 6.9. The obtained relative edge enhancement as a function of bandwidth is plotted at the bottom right. Thus, edge enhancement increases with BW until a maximum value of $558\,\mathrm{Hz\,px^{-1}}$ is reached. This can be explained by a general decline of gradient performance, since the extent of the above mentioned gradient effects depends on the gradient strength. However, obviously the enhancement decreases with very high BWs. There is, thus, reason to presume that here the image blurring dominates.

Edge enhancement as a gradient effect is also evident from the following measurement: Figure 6.10 shows three agarose-gels. The volume resonator including all samples in Fig. 6.10(b) was rotated through approximately 90° relative to the gradient system configuration in Fig. 6.10(a) (the cross indicates the rotating axis). The colour mapped signal intensity shows an explicit dependence of edge enhancement on the direction of the gradient. The enhancement seems to appear only center-out in a distinguished direction (here x-direction).
This in turn means that also the correction of gradient delay should be set differently for the three orthogonal gradients. However, to my knowledge the ICE programming environment only provides a single delay parameter, which effects on all three gradients equally.

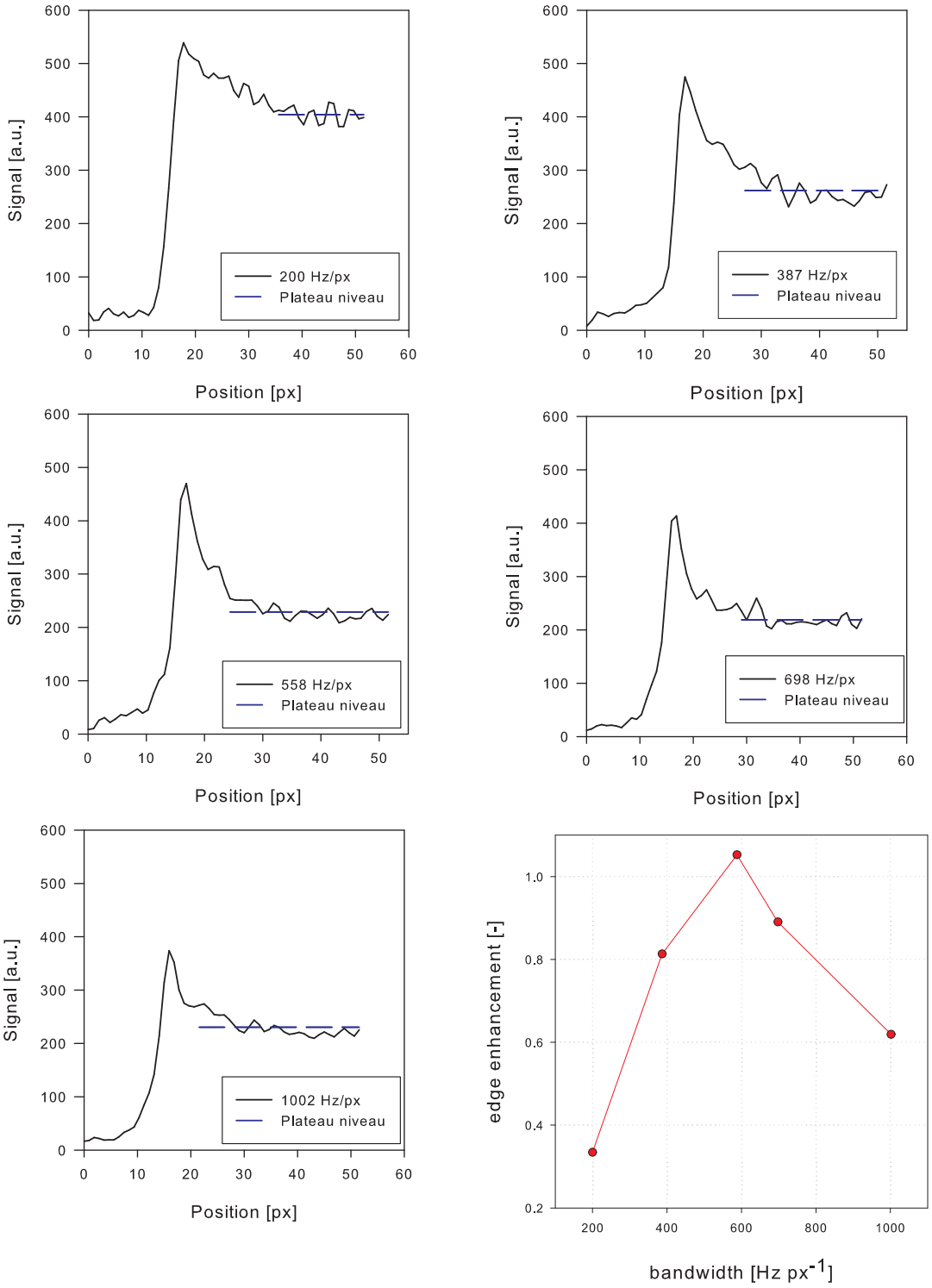

Figure 6.9.: Analysis regarding edge enhancement: Single line profiles for 5 measurements with various BWs. The blue dashed line indicates the selected plateau niveau. The relative edge enhancement as a function of bandwidth is plotted at the bottom right.

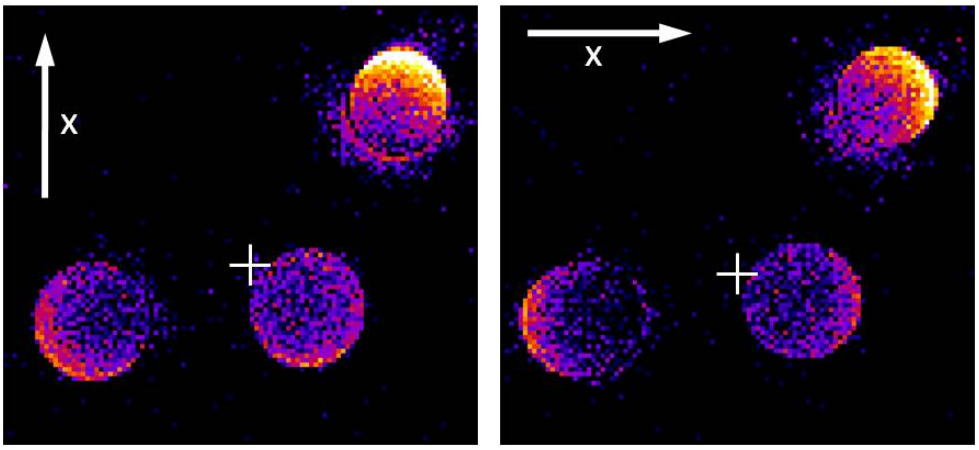

(a) (b)

Figure 6.10.: Edge enhancement in dependence on the gradient direction: The volume resonator including all samples in (b) was rotated through approximately 90° relative to the gradient system configuration in (a). The cross indicates the rotating point (centre line of resonator). Three agarose-phantoms. FOV: $40 \times 40\,\mathrm{mm}$, TR = 251 ms, TE = 0.07 ms, BW = $558\,\mathrm{Hz\,px^{-1}}$, $\alpha = 5°$, $N = 128$, $N_{proj} = 60032$, 2 signal averages.

6.3. Optimisation of Gradient Delay Correction

In order to minimise the edge enhancement, the method discussed in Section 5.3.1 was applied. Figure 6.11 shows a single measurement on the HMA-in-water phantom. The raw data was subsequently reconstructed (*icesimu*) allowing for 8 distinct gradient delay correction times ranging from $-0.76\,\mu s$ to $14\,\mu s$. Since the gradient delay value was systemically assumed to be too low by the "getTimeDelay()" function of the sequence, the subsequent reconstruction was therefore performed consistently at higher values. The smallest delay time (here, $-0.76\,\mu s$) is than typically the default value in the first place.

The analysis of the edge enhancement at a BW of $558\,\mathrm{Hz\,px^{-1}}$ is shown in Figure 6.12. Here the relative enhancement could be minimised for a gradient delay correction of $4.5398\,\mu s$. Because of the direct correlation between enhancement and gradient strength, this value could not be implemented into the sequence as a hard value. Therefore the measurement and analysis was repeated for multiple bandwidths ranging from $200 - 1000\,\mathrm{Hz\,px^{-1}}$. The result together with the "getTimeDelay()" function is shown in Figure 6.13. Apparently, the values of the gradient delay correction are simply shifted by an offset factor.

In order to implement the delay time dynamically, these offset factor τ was defined as

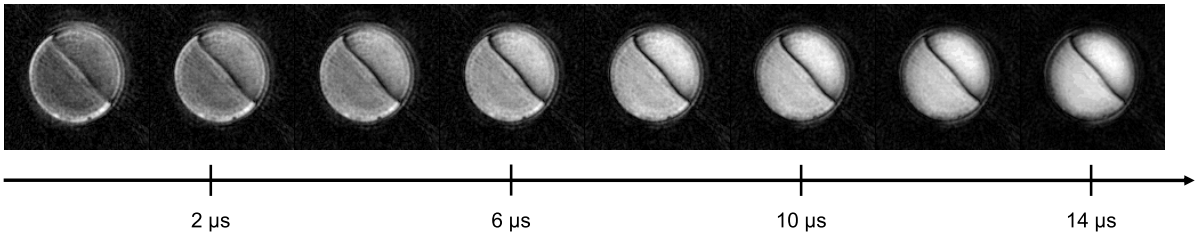

Figure 6.11.: Single measurement on the HMA-in-water phantom. The raw data was subsequently reconstructed at 8 distinct gradient delay correction times ranging from $-0.76\,\mu s$ to $14\,\mu s$. Here the relative enhancement could be minimised for a gradient delay correction of $4.5398\,\mu s$.

the average value of the three highest* evaluated bandwidths:

$$\tau = \frac{1}{3}\sum_{i=1}^{3}\tau_i. \tag{6.3}$$

The result is a gradient delay correction offset of $5.8\,\mu s$. This value was implemented into the sequence for a TE time less than $0.5\,ms$ (cf. Sec. 5.3.1). It was found that for longer time intervals the optimal delay correction is almost constant under variation of BW. Within the interval $0.5\,ms \leq TE \leq 1.0\,ms$ the delay correction was set to $2.5\,\mu s$, while for longer TEs the correction was figured out to be zero.
After the successful implementation of these delay corrections into the pulse sequence, the image quality could be improved significantly.

* Significant edge enhancement artefacts appears most likely at high bandwidth.

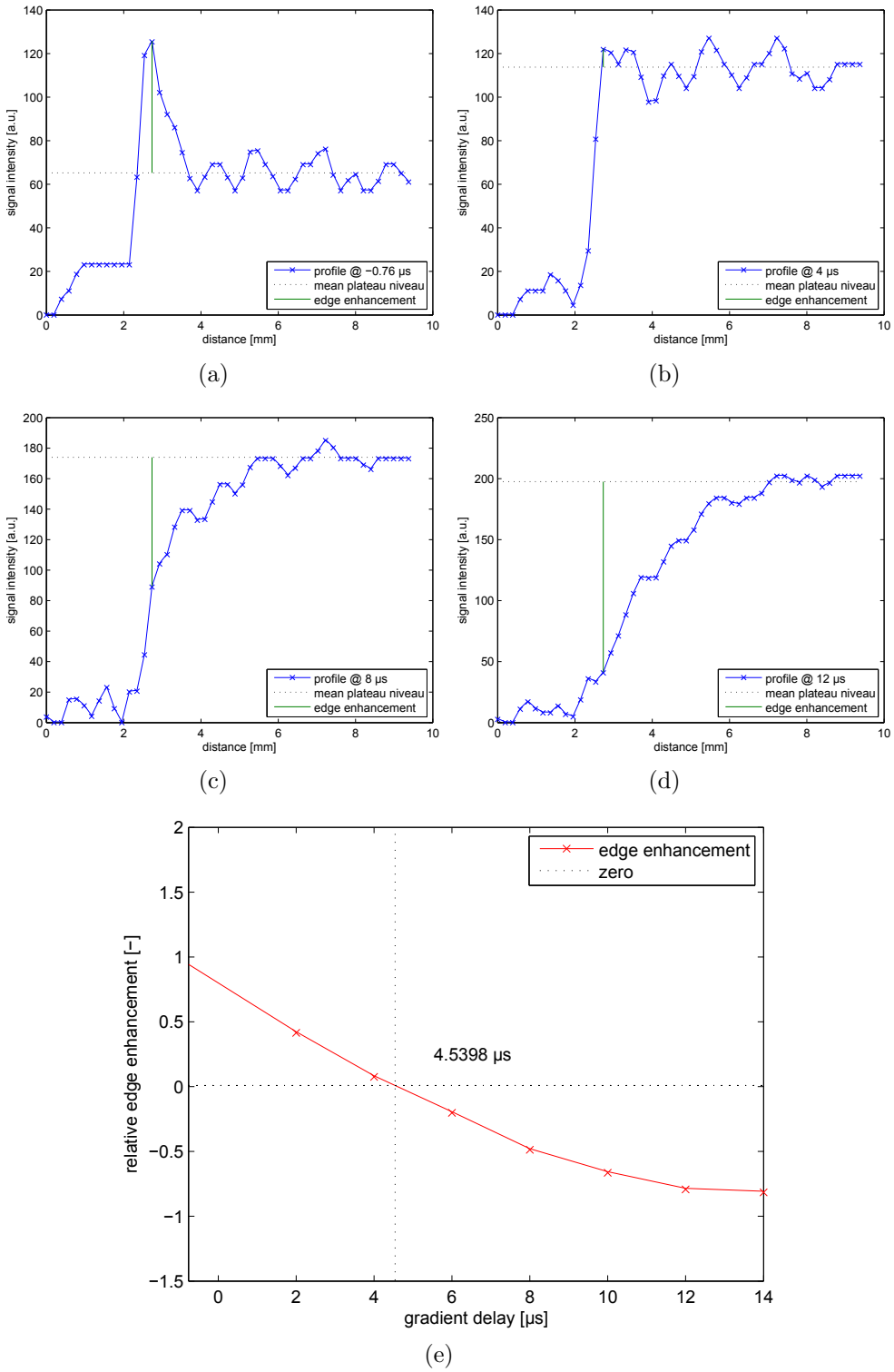

Figure 6.12.: Optimal gradient delay correction: Determination of edge enhancement from line profiles for different correction times ranging from $-0.76\,\mu s$ to $14\,\mu s$ (a-d). Optimal correction time is found by linear interpolation (d). The procedure was repeated for multiple bandwidths ranging from $200 - 1000\,Hz\,px^{-1}$ (here $558\,Hz\,px^{-1}$).

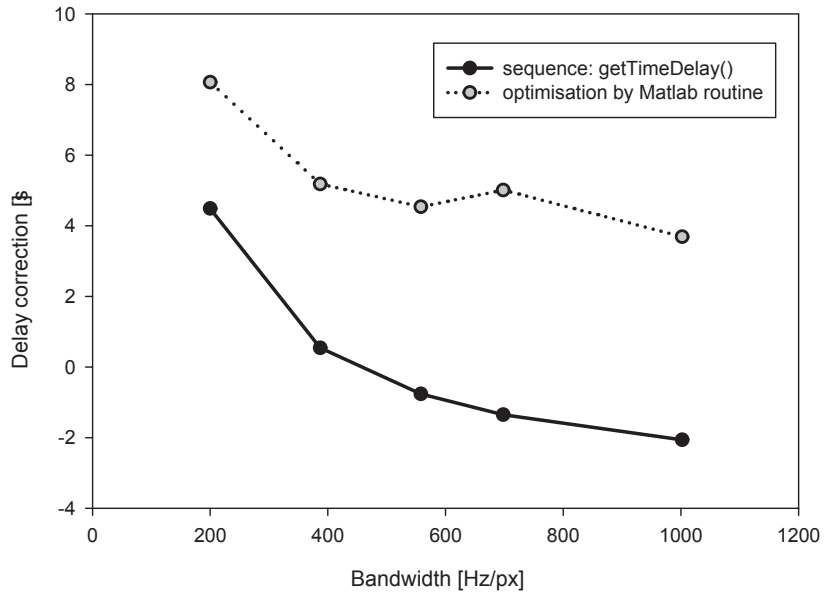

Figure 6.13.: Gradient delay correction times as a function of bandwidth: By default the sequence applies the function "getTimeDelay()" (solid line). The experimental values are systematically higher (dashed line). Apparently, the values of the optimal gradient delay correction are simply shifted by an offset factor.

6.4. UTE: Achievable Spatial Resolutions

Inverse Point Spread Function in Water

The possibilities of determining the spatial resolution in images were discussed in Section 5.4.1. First of all the resolution is limited by image blurring, which in turn depends on multiple factors (cf. Sec. 6.2). Among others, the kind of material plays an evident role. Therefore, the achievable spatial resolution was evaluated initially on a glass capillary in a water environment representing an approximated inverse PSF.
Two line profiles, in radial (blue) and normal direction (red) are shown in Figure 6.14. Due to the image reconstruction mechanism it is reasonable to discriminate these two directions. The raw data could be fitted by a Gaussian function.

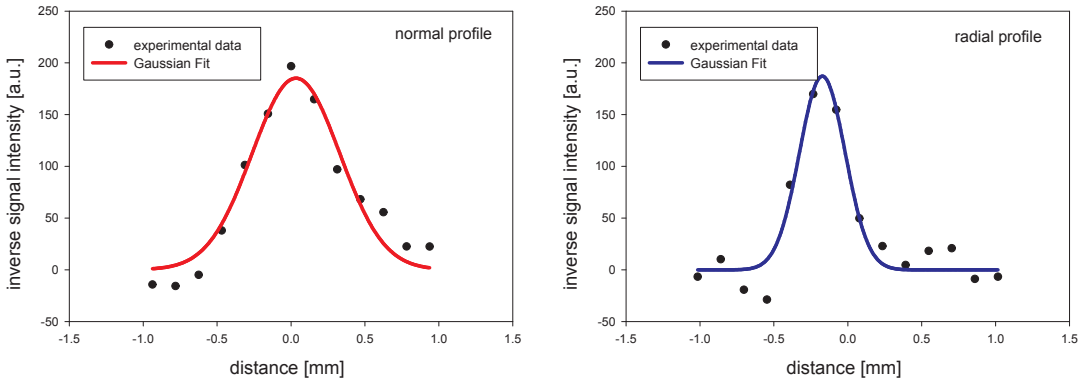

(a) (b)

(c)

Figure 6.14.: Glass capillary in water representing an approximated inverse PSF: Two line profiles, in radial (blue) and normal direction (red) were measured and fitted by a Gaussian function (a-b). The profiles were obtained from multiple transversal slices (c, cropped) in order to allow a statistical evaluation. FOV: $20 \times 20\,\text{mm}$, TR $= 450\,\text{ms}$, TE $= 0.07\,\text{ms}$, BW $= 200\,\text{Hz}\,\text{px}^{-1}$, $\alpha = 5°$, $N = 128$, $N_{proj} = 4032$.

Figure 6.15 shows the resulting modulation transfer function obtained from both, the actual "pixel-value" profile and the Gauss-fitted (filtered) profile. In contrast to the Gaussian filtered profile, the actual profile was measured and analysed seven times for different slices at same position in order to allow a statistical evaluation. The achievable spatial resolution is then given at modulation 50% (dashed line):

$$\begin{aligned} \text{Gauss filtered:} \quad & \Delta x_{g,r} = 0.904\,\text{mm} \quad \text{(radial)} \\ & \Delta x_{g,n} = 1.155\,\text{mm} \quad \text{(normal)} \end{aligned}$$

$$\begin{aligned} \text{Pixel value:} \quad & \Delta x_{r} = (1.0 \pm 0.1)\,\text{mm} \quad \text{(radial)} \\ & \Delta x_{n} = (1.2 \pm 0.2)\,\text{mm} \quad \text{(normal)} \end{aligned}$$

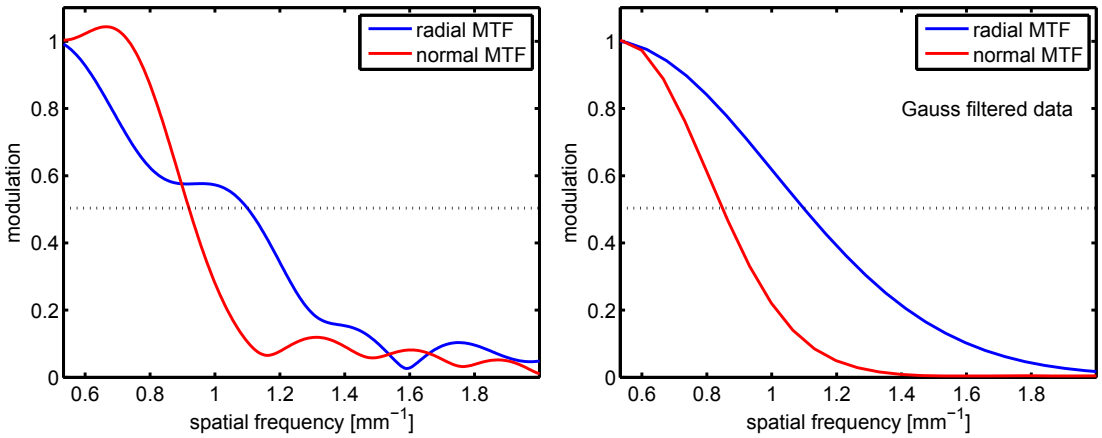

Figure 6.15.: Resulting modulation transfer function (MTF): obtained from an exemplary actual "pixel-value" profile (a) and a Gauss-fitted (filtered) profile (b). The achievable spatial resolution is then given at modulation 50% (dashed line).

Edge Response on short-T2 Material

The resolution capabilities of the sequence in respect to short-T2 materials were evaluated using the edge spread function (ESP). Figure 6.16 shows a hot melt adhesive block within a teflon holder fixed in position by a foam material and the corresponding line profile location. Based on an ESF analysis, the spatial resolution was obtained as de-

scribed in Section 5.4.1 for five different receiver bandwidths. The measurements were performed before optimal gradient delay correction and the result is shown in Figure 6.17.

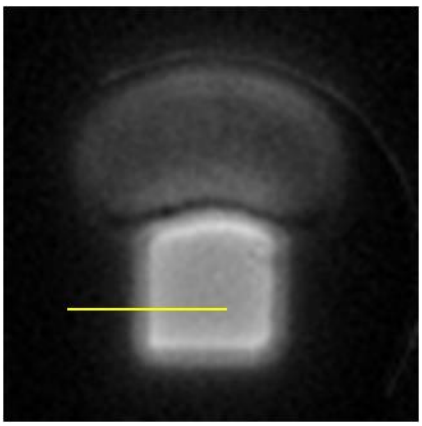

Figure 6.16.: Evaluation of the edge spread function (ESF): Hot melt adhesive block within a teflon holder fixed in position by a foam material and the corresponding line profile location. FOV: $30 \times 30\,\mathrm{mm}$, TR $= 255\,\mathrm{ms}$, TE $= 0.07\,\mathrm{ms}$, $\alpha = 7°$, $N = 128$, $N_{proj} = 9984$, BW $= 558\,\mathrm{Hz\,px^{-1}}$. The measurement was performed before optimal gradient delay correction.

It can be seen, that the spatial resolution gets better with increasing receiver bandwidth. This is probably due to the broad line width of the semi-solid material, which requires a strong frequency-splitting in order to separate finer structures. The line width of the HMA material is approximately 500 Hz (cf. Fig. 6.7).
The achievable resolution at $558\,\mathrm{Hz\,px^{-1}}$ was found to be

$$\Delta x_{558}^{ESF} = (4.1 \pm 0.2)\,\mathrm{mm}. \tag{6.4}$$

This result could be confirmed by another experiment, which measured the approximate PSF from a thin HMA filament. Therefore the phantom depicted in Figure 4.4(a) was used. A subsequent Fourier transformation of multiple line profiles and the validation of the MTF gave a resolution capacity of

$$\Delta x_{558}^{PSF} = (3.9 \pm 0.1)\,\mathrm{mm}. \tag{6.5}$$

To sum up, the achievable spatial resolution is essentially limited by the image blurring, which in turn depends on several factors. While imaging short-T2 materials, it could be shown that the smallest structures to be resolved are 4 times larger relative to long-T2

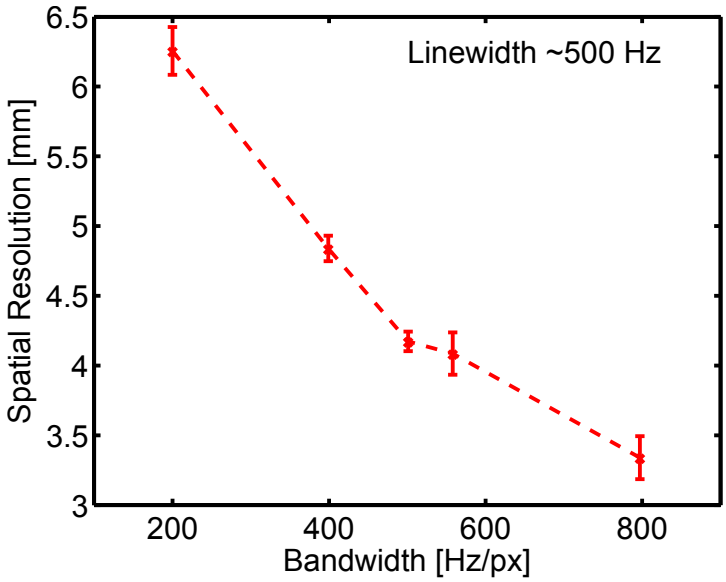

Figure 6.17.: Evaluation of ESF: Spatial resolution as a function of receiver bandwidth. The line width of the HMA material is approx. 500 Hz (cf. Fig. 6.7).

materials. However, the resolution capacity of the UTE sequence, which is in the order of 1 millimetre when using a relatively low number of profiles, is highly restricted compared to conventional TSE pulse sequences achieving resolutions of some 10 microns. On the one hand this is due to the general imaging quality of the sequence (especially while using a low number of profiles) and on the other hand, broad-line, short-T2 materials contribute to image blurring.
When these experiments were done, the maximum number of radial views was limited to 9984. As discussed in Section 6.2, this number is another crucial parameter on blurring and therefore on spatial resolution. In the course of this thesis, the limitation in radial views could be expanded by a factor of 10 (cf. Sec. 5.3.1). Purely subjectively, the resolution capacity improved simultaneously, due to the given relation (6.1) regarding the optimal number of projections (Nyquist-Shannon sampling theorem).

6.5. Evaluating UTE and TSE Sequences featuring Magnetisation Transfer Contrast

In this section the applicability and usability of the pulse sequences modified by an additional option for magnetisation transfer contrast is evaluated. Therefore, the per-

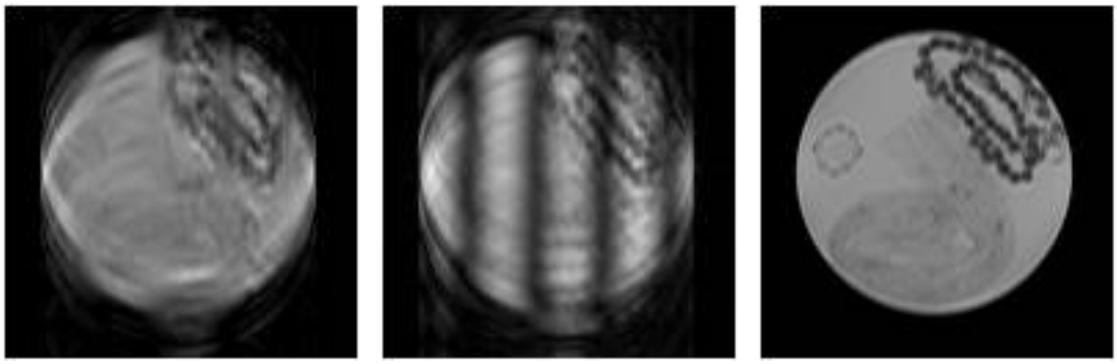

(a) (b) (c)

Figure 6.18.: Initial difficulties using the TSE+MTC sequence: (a-b): Strong artefacts after changing protocol parameters like pulse duration or detection time due to a timing error within the pulse sequence. (c): Corrected image after increasing the "duration" time increment.

formances of the TSE and UTE sequence were demonstrated on different phantoms (cf. Sec. 4.2).

6.5.1. TSE+MT

Initial measurements using the TSE+MTC sequence showed strong artefacts after changing protocol parameters like pulse duration or detection time (Fig. 6.18(a-b)). After some approaches to solve the problem by an additional spoiler gradient and a larger time gab before the RF excitation, the effect could be traced to be due to a timing error within the pulse sequence itself. This could be corrected relatively easy by increasing the "duration" time increment from 1 µs to 10 µs (Fig. 6.18(c)).

A performed MT measurement is shown in Figure 6.19. Here, the impact of different offset frequencies on image contrast in MT-weighted images is investigated. The MTC phantom consists of three materials including textiles (a,b) and a plant stem (c) (cf. Sec. 4.2). In Figure 6.19 the image to the upper left represents a density-weighted TSE image, which serves as reference. The images in the upper row differs in varying offset frequencies of a 10 ms Gaussian shaped saturation pulse. The lower row shows the corresponding difference images.

Whereas at low offset frequencies a significant amount of free protons within the sur-

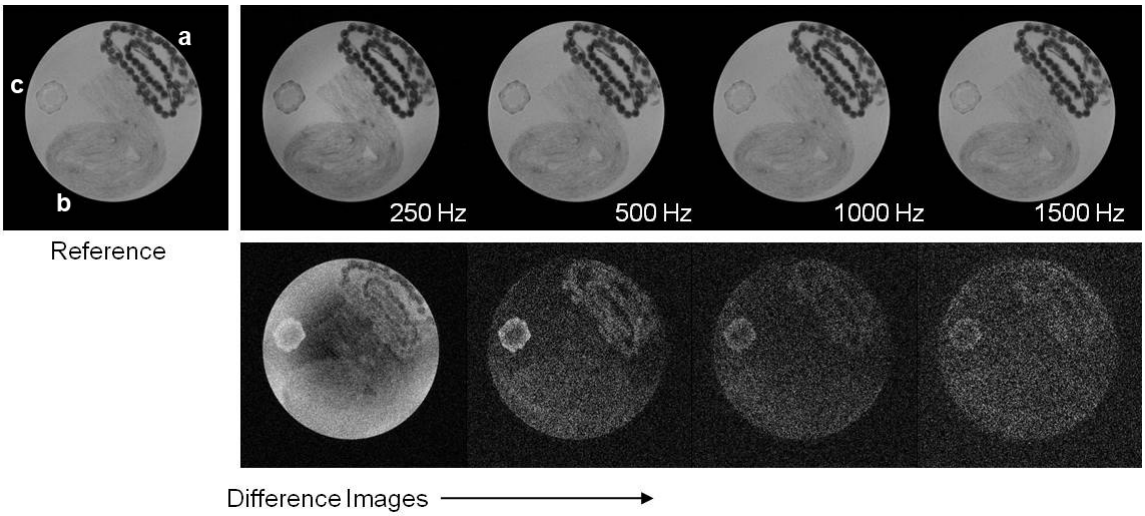

Figure 6.19.: Impact of different offset frequencies on contrast in MT-weighted images: The density-weighted TSE image in the upper left represents the reference. Varying offset frequencies of a 10 ms Gaussian shaped saturation pulse (upper row) and corresponding difference images (lower row). The MTC phantom consists of three materials including textiles (a,b) and a plant stem (c). FOV: 20×20 mm, TR = 4000 ms, TE = 13 ms, BW = 130 Hz px^{-1}, Matrix: 256×256.

rounding water gets saturated, the contrast at higher offset frequencies appears more differentiated. There is a distinct contrast especially within the plant stem. With an increasing offset frequency the contrast is reduced, while the noise continues to rise relative to the signal.
The resulting contrast within the plant stem matches the MT model concept: The center of the stem, which is composed of spongy, slightly widened parenchyma cells in the pith, appears quite dark. Usually, in place with wide, air-filled vessels. Because of this low density of cell material, the major content within this region are free (water-) protons and therefore, the expected magnetisation transfer is greatly reduced. Nevertheless, the pith is encircled by rings of xylem and phloem (cf. Lüttge et al., 2005). Here the tissue is much more dense leading to a more distinct interaction between free and bound protons. That explains the high, ringing-like signal within the stem.

Figure 6.20 shows the dependency of MT-weighted image contrast on the saturation pulse amplitude. The reference amplitude of the used 19 mm-resonator, which is defined as the pulse amplitude corresponding to a 90°-flip within 0.5 ms, is about 6 V.

The pulse amplitude was varied ranging from 3.4 V to 40 V. At very high amplitudes there is a tendency for artefacts, which are due to RF inhomogeneities. Here already small deviations in the RF field are leading to large flip angles. This explains the periodical signal loss, which correlates with the coil geometry of the resonator.
Thus, the contrast within the difference images is only physiological meaningful at intermediate saturation pulse amplitudes. The raise of signal-to-noise ratio between 3.4 V and 10 V can clearly be seen. Also the contrast becomes more distinct using higher amplitude.
The reason for that seems to be obvious: Saturation is obtained by the equalisation of both spin energy niveaus resulting in a vanishing net magnetisation. The stronger the RF (photon) field, the more transitions per unit of time can be achieved leading to a greater saturation.

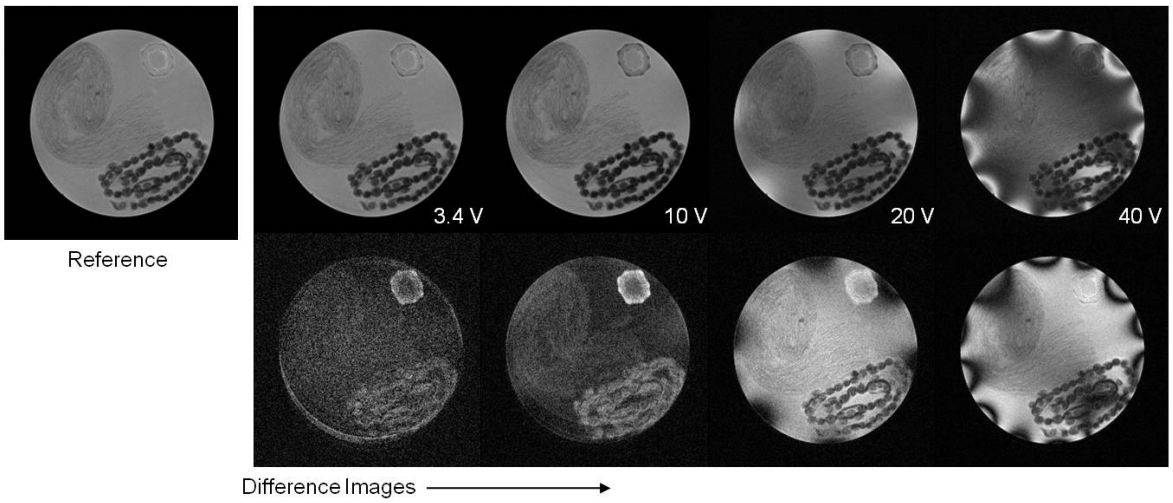

Figure 6.20.: Dependency of MT-weighted image contrast on the saturation pulse amplitude. FOV: 20×20 mm, TR = 4000 ms, TE = 13 ms, BW = 130 Hz px^{-1}, Matrix: 256×256.

6.5.2. UTE+MT on BSA phantoms

Of course, the saturation performance of an investigated sequence depends primarily on the sample. Therefore cross-linked bovine serum albumin (BSA) phantoms (cf. Sec. 4.2) were used in order to quantify the achieved signal saturation and to improve comparability of the TSE- and UTE pulse sequence.
Figure 6.21 shows a series of measurements executed on three homogeneous BSA phantoms of different BSA-to-water concentrations (0.18/0.26/0.30-wt. %) as a test of the modified UTE+MTC sequence. The relative signal intensity is shown as a function of off-resonance frequency and MT-pulse amplitude. The signal intensity was measured at four frequency offsets (600, 900, 1200 and 1500 Hz) and in each case at five different RF amplitudes ranging from 17 V to 55 V (reference amplitude 30 V).
As expected, the signal decreases with a higher RF-amplitude and lower frequency offset. Thereby, the relative signal saturation is more pronounced for higher BSA concentrations (linear dependency).

In order to evaluate the effectiveness of the signal saturation, they were compared to measurement results obtained by the TSE+MTC sequence for a single offset frequency and RF amplitude (Tab. 6.1).

BSA per weight	TSE+MTC Rel. Signal		UTE+MTC Rel. Signal	
	mean	error	mean	error
0.18	63%	±4%	73%	±18%
0.26	56%	±4%	64%	±9%
0.30	48%	±4%	58%	±15%

Table 6.1.: Comparison: MT performance of UTE and TSE sequence featuring a Gaussian-shaped saturation pulse 600 Hz off-resonant and a RF amplitude of 55 V.

The results of both sequences are in conformity within the standard error range. There are smaller relative errors for the TSE sequence which are mainly due to less (streaking) artefacts and an inherently better SNR*.
More or less this measurements can be considered as qualitative. Utilizing quantitative MT imaging methods the bound pool fraction (BPF) can be determined, which is the molar fraction of motional restricted protons within a substance (Soellinger et al.,

* $\mathrm{SNR}_{TSE} \approx 60$ versus $\mathrm{SNR}_{UTE} \approx 8$

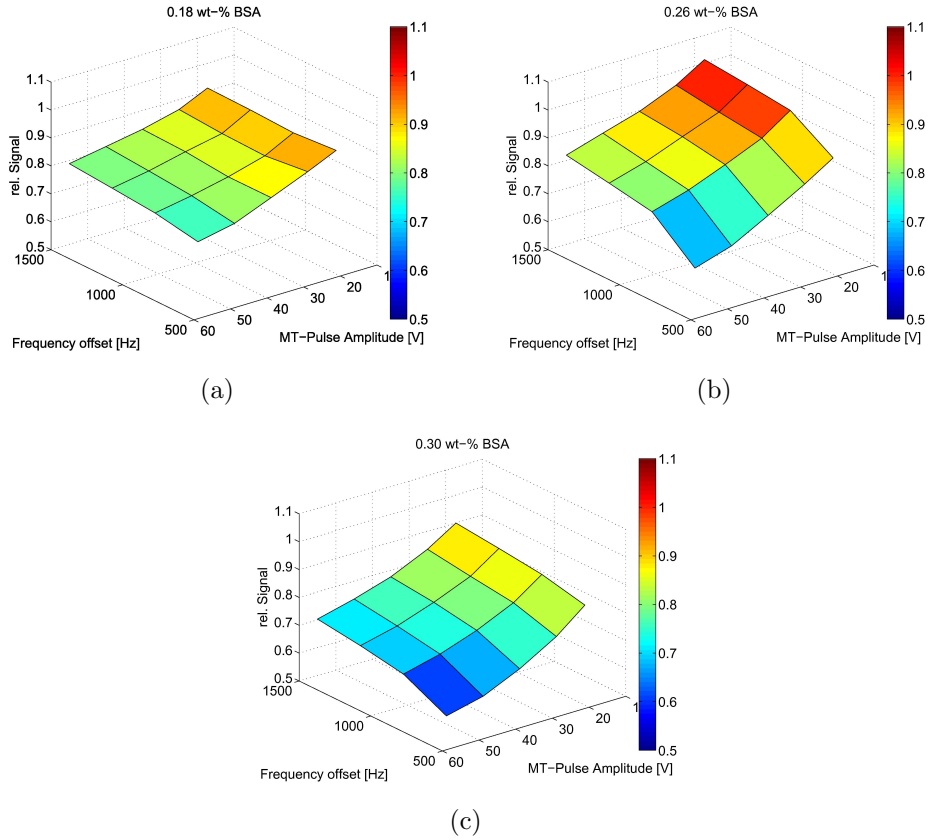

Figure 6.21.: Testing of the modified UTE+MTC sequence: Relative signal intensity as a function of off-resonance frequency and MT-pulse amplitude performed on three homogeneous BSA phantoms using different BSA-to-water concentrations (0.18 (a) / 0.26 (b) / 0.30-wt. % (c)).

2011). Here, the experiential technique is quite different. Instead of directly saturate the bounded proton spins by off-resonant excitation, Soellinger et al. labelled the magnetisation of protons associated with free water only. The signal obtained after a certain mixing time (TM) is governed by the magnetisation transfer between free and bounded spin ensembles. The quantitative BPF can then be calculated from the signal amplitude as a function of TM.
In this publication the authors used exactly the same BSA phantoms. Their results show a linear relationship between different BSA concentration and corresponding BPF values, which agree with the values shown in Table 6.1. Unfortunately a quantitative comparison is not possible due to missing detailed data.
The association of the saturated signal with an actual physical or chemical mechanism and therefore the interpretation of the obtained data is rather difficult. Sequence design and parameters in combination with short T1 times have significant effect on the amount of saturated signals (see Sec. 7.4).

Further MT measurements can be found in the next chapter dealing with the application on biological samples and which are partly overlapping with quality control results.

Chapter 7

Applications

The following investigations represent preliminary first results at the end of the diploma thesis comprising a very limited number of samples kindly made available by colleagues at the high-field MR-Center. The preliminary results are included in this thesis to demonstrate some perspectives and open questions for possible future applications of UTE and MT along with the microimaging insert on the human high-field scanner.

7.1. Achilles Tendon

The Achilles tendon is the thickest and strongest human tendon at the back of the heel. This tissue is only poorly detectable by conventional sequences due to the majority of short T2 components. Since tendons consist of almost parallel aligned bundles of collageneous fibres, it is possible to increase the MR signal by taking advantage of the magic angle effect (Du et al., 2009). However, the UTE sequence provides a more flexible application over the full range of angles.

Figure 7.1 shows an image obtained from the UTE-sequence on a human Achilles tendon* ex-vivo relatively close to the enthesis (Fig. 7.1(a)). The sample tube was placed isocentrically inside the 19 mm-resonator together with some paper wrapped around.

Using a conventional TSE sequence the Achilles tendon appears dark. Figure 7.1(b) is a transverse TSE image (TR/TE = 2000/7.5 ms) of the sample showing the tendon, its surrounding sliding fabric (paratenon) and "Kager's fat pad" (cf. Nunley, 2009). Close

* Courtesy of Mag. J. Friske and Dr. S. Leder, Medical University of Vienna.

inspection reveals, that the fascicular structure of the tendon is slightly perceptible. Here the signal could be generated by blood vessels and/or the thin endotenon tissue located between the collagen fibre bundles (cf. Robson et al., 2004). This becomes even more apparent in sagittal images (Fig. 7.2).
However, the largest part of the tendon remains dark. Figure 7.1(c) shows a UTE images featuring the shortest detection time possible (TE = 0.07 ms). Here, the tendon has a high signal providing a proton-density weighted contrast. Since this is the original version of the UTE sequence, the missing gradient delay correction leads to the characteristic edge enhancement artefact. The UTE detection time in Figure 7.1(d) is in the same range as the TSE image (TE = 7 ms) and was acquired without major time lag. A subsequent difference image (TE = 0.07 ms minus TE = 7 ms) gives a different contrast, showing hyperintense regions for tissue compartments with short T2 (Fig. 7.1(e)). The hyperintense "corona" represents an image artefact, which is due to the dependency of edge enhancement on different detection times.
Nevertheless, the greater signal available by using UTE compared to TSE is obtained at the expense of signal to noise ratio and spatial resolution.

(a)

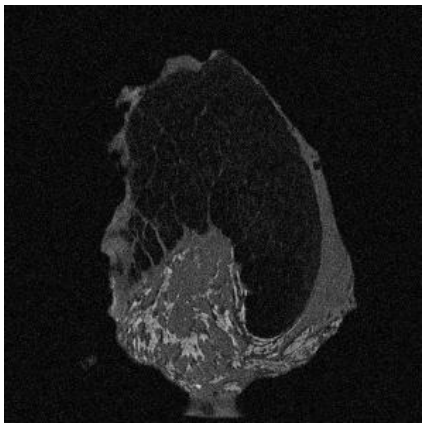

(b)

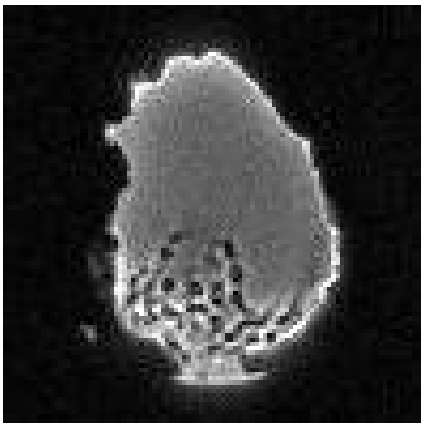

(c)

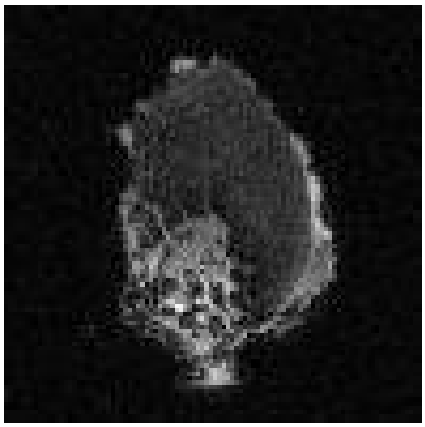

(d)

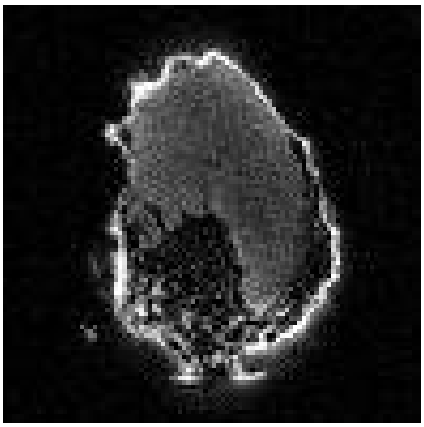

(e)

Figure 7.1.: Ex-vivo measurements on an Achilles tendon. Figures (b-e) show a transverse slice close to the enthesis (a, dashed line). (b): The tendon appears dark while using a TSE sequence (FOV: approx. $25 \times 25\,\mathrm{mm}$ cropped, TR/TE = 2000/7.5 ms, BW = $501\,\mathrm{Hz\,px^{-1}}$, Matrix: 256×256, turbo factor 3, 10 signal averages). (c): In contrast, the UTE sequence provides a high tendon signal at short detection time (TR/TE = 698/0.07 ms, BW = $558\,\mathrm{Hz\,px^{-1}}$, $\alpha = 7°$, $N = 128$, $N_{proj} = 60032$). (d): T2-weighted UTE image (TE = 7 ms), (e): The difference image (TE = 0.07 ms minus TE = 7 ms) gives a different contrast, showing hyperintense regions for tissue compartments with short T2.

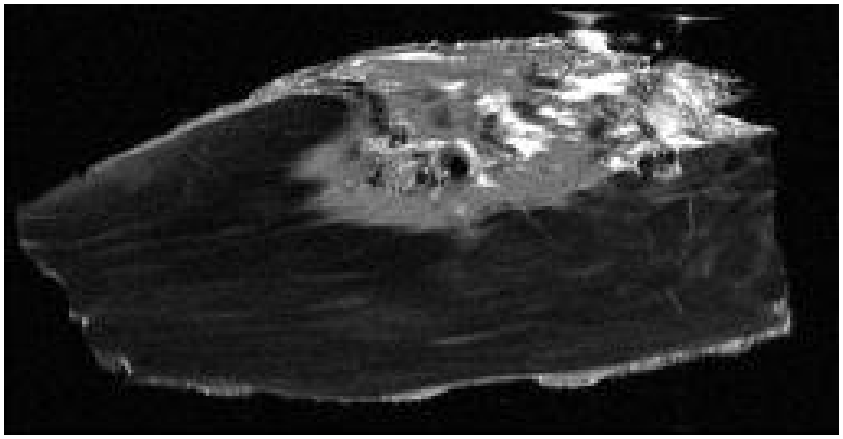

Figure 7.2.: Sagittal TSE image of an Achilles tendon ex-vivo. The fascicular structure is slightly visible as parallel stripes of high signal. This could be attributed to blood vessels and/or the thin endotenon tissue located between the collagen fibre bundles. FOV: $132 \times 67\,\mathrm{mm}$, TR $= 2000\,\mathrm{ms}$, TE $= 7.5\,\mathrm{ms}$, BW $= 501\,\mathrm{Hz\,px^{-1}}$, Matrix: 256×256, turbo factor 3 and 10 signal averages.

7.2. Cruciate Ligament

The same discussion is true for ligaments, which are very similar to tendons in their structure. Figure 7.3(a) shows a human posterior cruciate ligament (PCL). On this sample, the MT contrast applicability of the UTE (and TSE) sequence was evaluated ex-vivo.

A sagittal detail image of about $20 \times 20\,\text{mm}$ is shown in Figure 7.4. Here, the results from both sequences can be compared directly. Figure 7.4(a) represents a simple TSE measurement using a relatively short echo time (TR/TE = 2000/7 ms). In analogy with the previous discussed tendon images, the actual ligament appears quite dark (a). However, finer structures can be distinguished. The field of view shows the region of the ligament-bone interface. A small fraction of cancellous bone is probably represented by the dark spot at the lower right (b). The high signal interface line, which runs diagonally, could be the larger, and less parallel aligned collagen fibres of uncalcified cartilage, which is characterised by a greater water content (c). The hyperintense signal region on the left side seems to be fat tissue (d).

The measurement was repeated with a standard MTC saturation pulse 1.2 kHz off-resonant and an amplitude of 20 V. Figure 7.4(b) shows the MT-weighted difference image (TSE minus TSE+MTC). Here, especially regions where a bound pool of protons interacts with free protons, should be enhanced in signal. Apparently, this is true for the cartilage layer and along the fibrous ligament tissue. However, due to the complex structure of the biological sample, it is very difficult to make an educated guess on the image contrast.

Again this is confirmed by the results of the UTE measurement: Figure 7.4(c) shows the corresponding, density-weighted UTE image (TR = 270 ms, TE = 0.07 ms). It is notable that the signal is relatively homogeneous resulting in reduced contrast. The region, assumed to be related to fat tissue, appears dark in this UTE image. The MT-weighted difference image (Fig. 7.4(d)) was produced using the identical MT parameters. Apart from the poor resolution and SNR, the difference image provides a signal distribution, which is quite different from the TSE measurement. Now the ligament tissue shows a widespread enhanced signal, whereas the cartilage layer does not show a significant MT contrast. Though the same physical mechanisms is used for the contrast-weighing these observations might indicate a difference in the visualised spin pools. The UTE sequence provides additional signal from the ligament region which does not contribute

to MT contrast using the TSE sequence, i. e. is not available for saturation. Therefore, the enhanced signal in the difference image is plausible.
This result represents rather a "proof of concept" than an improved, expressive image contrast. Nevertheless, the UTE sequence offers an additional signal which opens the possibility for further contrast by spin preparation.

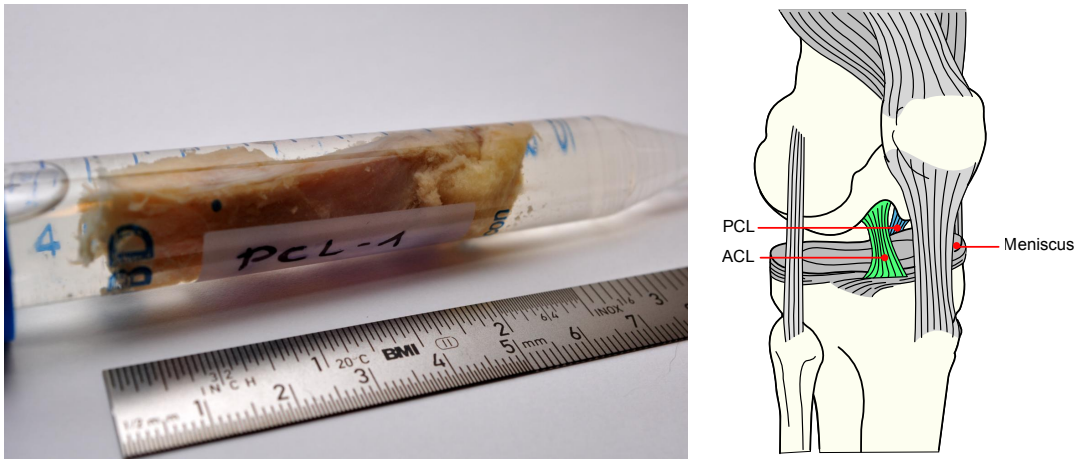

(a) (b)

Figure 7.3.: Posterior cruciate ligament (PCL) sample representing a short-T2 tissue (a). Diagram of the knee and position of the cruciate ligaments (b) (cf. Wikipedia, 2012).

A variation of MTC offset frequency in shown in Figure 7.5. The left image corresponds to the reference, which is identical with Figure 7.4(c). The series of four images to the right, represents difference images, i. e. MT-weighting. The offset frequency decreases from left to right in steps of 300 Hz initiating with 1200 Hz. The saturation pulse amplitude was kept constant at 20 V. Artefacts in MT-weighted images could not be distinguished.
Obviously, the MT contrast reaches a minimum at 900 Hz off-resonant. At this frequency the local spin saturation seems to be most unlikely and therefore the contrast in the difference image vanishes. In order to understand this result, it might be helpful to analyse the actual NMR spectrum of this sample in more details. Since this spectrum was not measured, it can only be speculated about the reason of contrast formation.
It is also conspicuous, that the images at 1200 Hz and 300 Hz off-resonant look such broadly similar. By intuition, the contrast at higher offset frequencies should be lower,

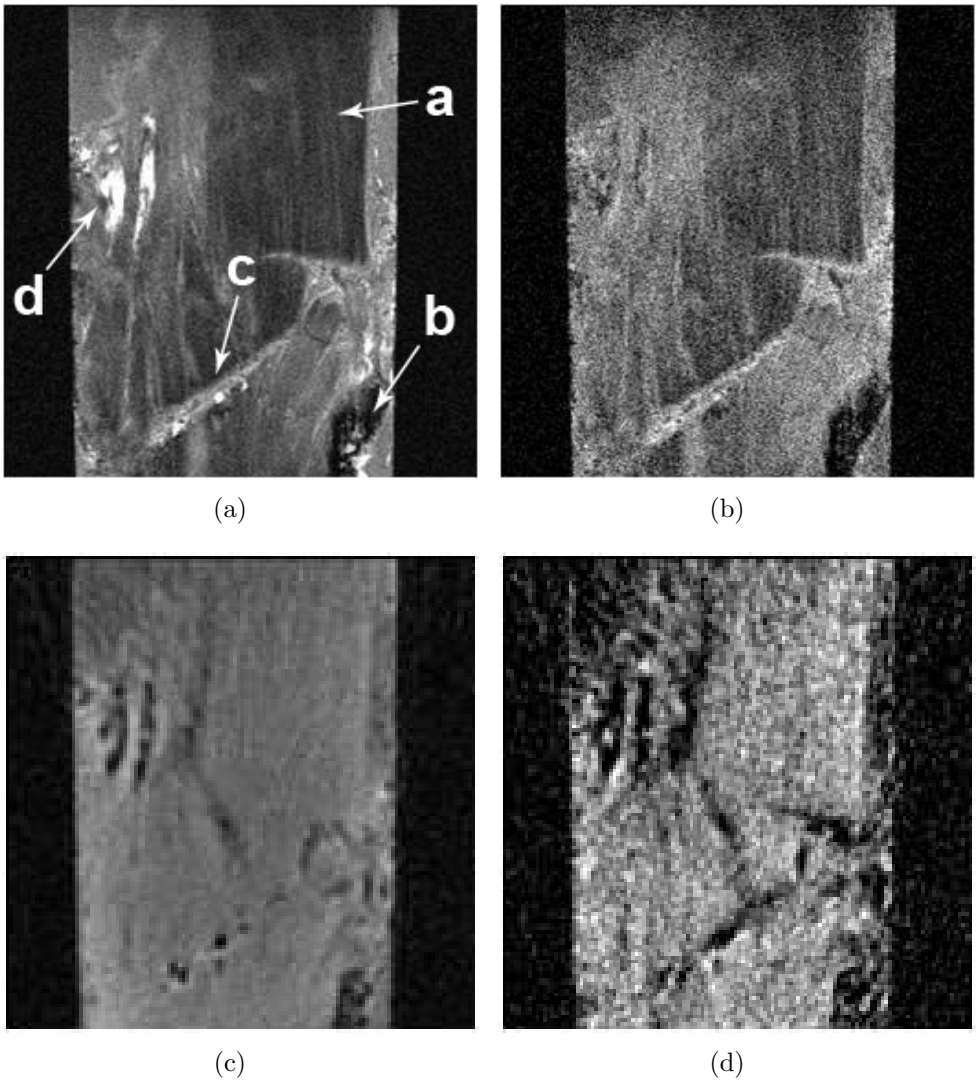

(a) (b)

(c) (d)

Figure 7.4.: Evaluating the MT contrast of the UTE sequence. Sagittal detail image of the PCL sample: (a): TSE measurement (FOV: $20 \times 20\,\mathrm{mm}$, TR = 2000 ms, TE = 7 ms, BW = $501\,\mathrm{Hz\,px^{-1}}$, Matrix: 256×256, turbo factor 3). (b): MT-weighted difference image (TSE minus TSE+MTC) using a standard MT saturation pulse (1.2 kHz, 20 V, 10 ms). (c): UTE measurement (TR/TE = 270/0.07 ms, BW = $501\,\mathrm{Hz\,px^{-1}}$, $\alpha = 7°$, $N = 128$, $N_{proj} = 9984$). (d): MT-weighted difference image (UTE minus UTE+MTC, 1.2 kHz, 20 V, 10 ms). Artefacts in MT-weighted images could not be distinguished (not shown).

because less spins should be involved in the saturation process. Seemingly, the spectrum of this complex sample looks like an intense water peak at 0 Hz and an additional peak at about 1200 Hz (approx. 4 ppm) resulting from chemical shifts. Since its duration was set to 10 ms, the bandwidth of the applied saturation pulse is less than 100 Hz. This issue highlights also a general problem of this kind of preparation pulses. Off-resonant excitation are not only sensitive to broad spectral lines but also on additional molecules separated in spectra by their chemical shift to water. This makes the interpretation of complex samples, without further information, quite difficult.

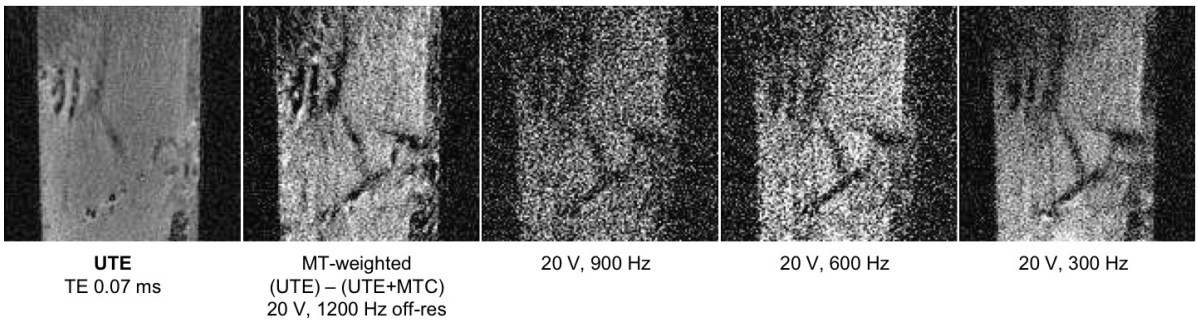

Figure 7.5.: Variation of MTC offset frequency using the UTE sequence. Left: Reference image (identical with Figure 7.4(c)). The offset frequency decreases from left to right in steps of 300 Hz initiating with 1200 Hz. The saturation pulse amplitude was kept constant at 20 V. The MT contrast reaches a minimum at 900 Hz.

7.3. Rat Backbone

A further sample is shown in Figure 7.6. This specimen is the backbone of a rat representing a paraplegia-animal-model*. At the marked position the spine was damaged due to an externally applied force.

Two coronal UTE images measured at different TEs (0.07 ms / 2.24 ms) and the corresponding difference image are shown in Figure 7.7. The stronger T2-weighting at TE = 2.24 ms affects short-T2 tissue in particular. This leads to an enhanced signal of the corresponding tissue in the difference image. Especially the bone marrow inside the vertebral bodies contrasts with the spinal channel. Edge enhancements are present in both of the differently T2-weighted images. Their difference due to varying detection

* Courtesy of Dr. P. Szomolanyi and Dr. N. Walder, Medical University of Vienna.

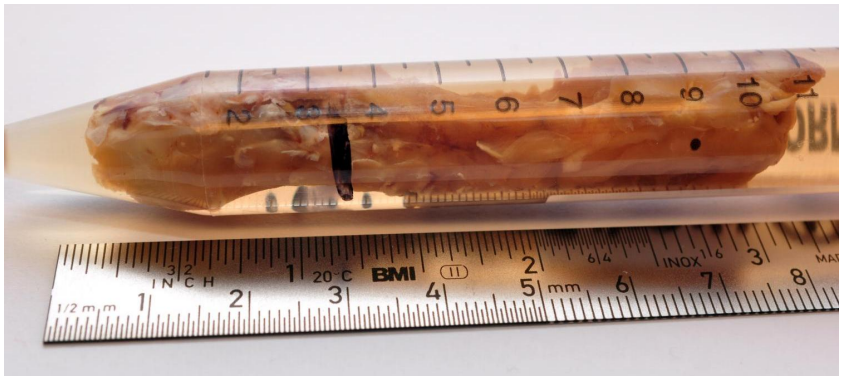

Figure 7.6.: Backbone of a rat representing a paraplegia-animal-model. At the marked position the spine is damaged due to an externally applied force.

time results in remaining artefacts at the edges in the difference image. Furthermore, any (image) instabilities like streaking artefacts lead to apparent signals in the difference image. Therefore the water surrounding the sample does not appear completely dark, although it exhibits a very long T2 time. Additional to that susceptibility effects could be another influence on contrast as well. These effects can usually arise e. g. at boundary layers or through organic iron displacement (Hall-Craggs, 2004). Images using longer detection times show higher sensitivity to susceptibility effects, which lead to a decrease of T2* within the tissue and can not be corrected in (gradient-echo) UTE imaging. The produces difference image can therefore represent a susceptibility dependent contrast (Robson et al., 2003; Gatehouse and Bydder, 2003).

A further investigation on TSE and UTE capabilities regarding MT contrast is shown in Figure 7.8. The TSE measurement, at the upper row, was repeated with the standard MT contrast option (1.2 kHz, 3.4 V, 10 ms) and the difference image was calculated. The damaged spine can be seen in the middle left side (arrow). The quite bright point appearing in the difference image could be originating from a small air bubble which might lead to susceptibility effects.

The lower row shows a similar UTE measurement. Here the offset frequency of the saturation pulse is set to 0.3 kHz while the amplitude is 25 V. The difference image shows a weak contrast for the single vertebral bodies, which may be due to a physical exchange process between a short-T2 tissue and a not detectable, very-short-T2 tissue and is not distinguishable using the TSE sequence. Here the combined UTE and MT sequence could provide additional information about the very-short T2 fraction (cf. Tyler et al.,

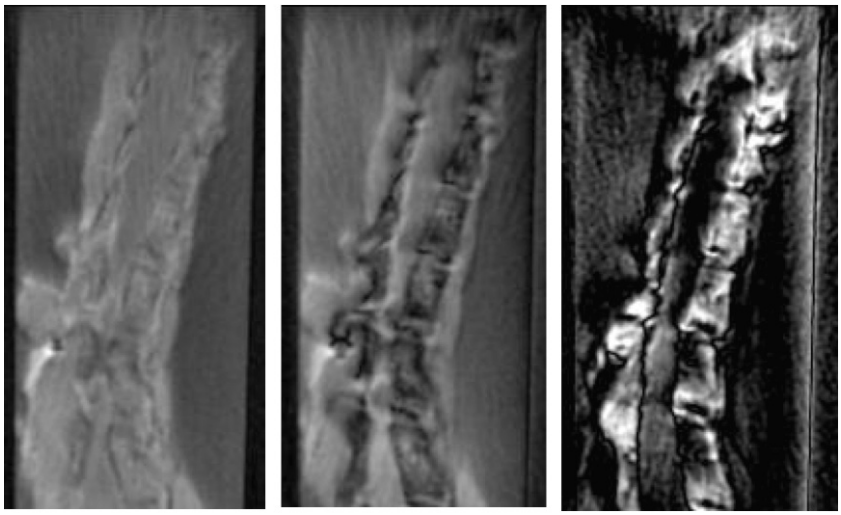

Figure 7.7.: Rat backbone sample: Coronal UTE images measured at different TEs (0.07 ms / 2.24 ms) and the corresponding difference image. The bone marrow inside the vertebral bodies gives a good contrast relative to the spinal channel. However, image artefacts and instabilities lead to apparent signals in the difference image. FOV: 28.8×28.8 mm (cropped), TR = 500 ms, BW = 558 Hz px^{-1}, $\alpha = 10°$, $N = 256$, $N_{proj} = 9984$.

2007). Unfortunately, a definite statement regarding the involved mechanisms can not be made, because of the complex biological sample and the relatively poor image quality.

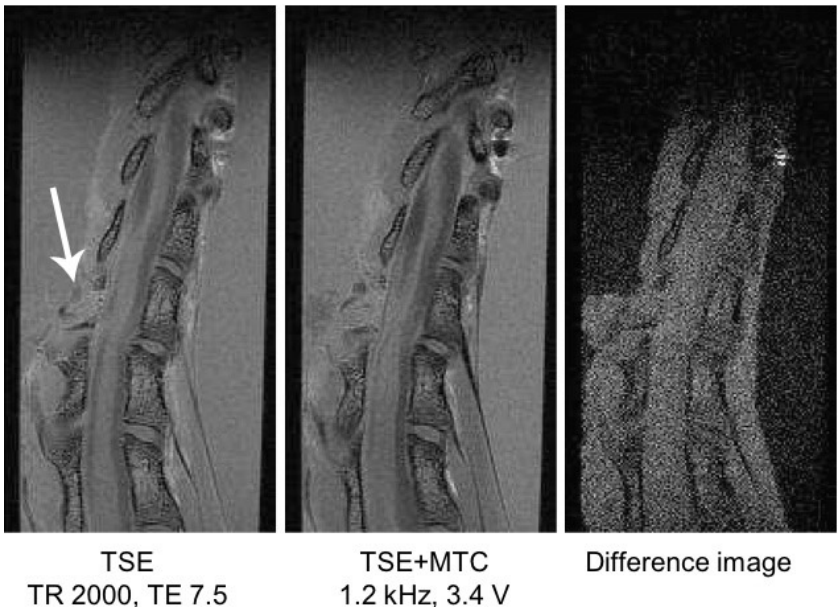

(a)

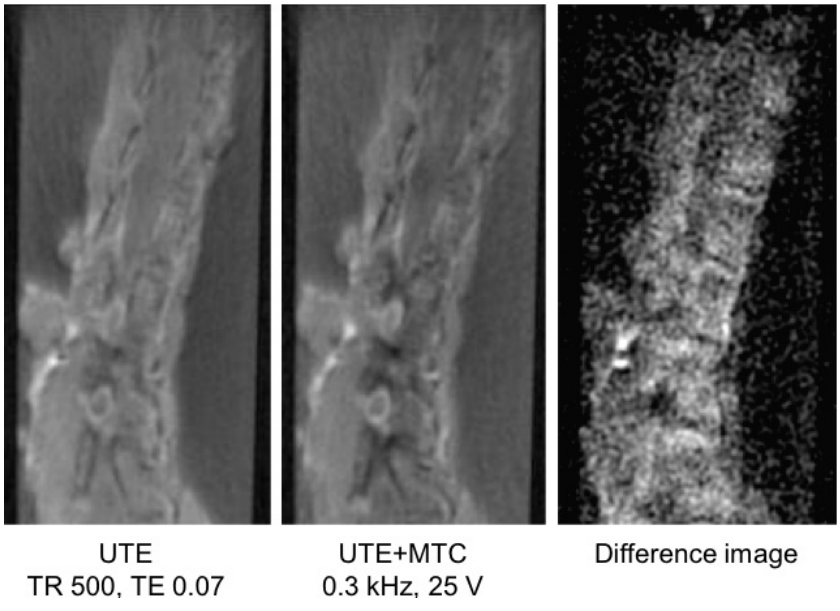

(b)

Figure 7.8.: Comparison of TSE and UTE capabilities regarding MT contrast: (a): TSE measurement with and without MT-weighting (1.2 kHz, 3.4 V), as well as the corresponding difference image (FOV: 29 × 15 mm, TR = 2000 ms, TE = 7.5 ms, BW = 501 Hz px^{-1}, Matrix: 256 × 256, turbo factor 3). (b): Similar UTE measurement. MT-weighting was obtained using a 0.3 kHz off-res. / 25 V saturation pulse (FOV: 28.8 × 28.8 mm (cropped), TR = 500 ms, BW = 558 Hz px^{-1}, $\alpha = 10°$, $N = 256$, $N_{proj} = 9984$). The damaged spine can be seen in the middle left side (arrow).

7.4. Wood and Dendrochronology

Dendrochronology is a method based on the temporal determination of tree ring formation in order to date past events or environmental conditions (cf. Taylor and Aitken, 1997). Thereby, the unique width pattern of the annual tree rings are characterised by discontinuities in the growing season. Under consideration of other external environmental factors, a continuous chronology of ring-widths can be made. A (hopefully statistically significant) visual comparison of historic wood then gives a highly accurate dating method.
The MRI provides the advantage of non-destructive visualisation of valuable historic wood. Moreover, MR microimaging can offer spatial resolutions high enough for smaller samples.

Figure 7.9 shows the measurement of about 3500 years old, ancient wood (unknown species) samples* together with a privet branch sample (*Ligustrum vulgare*) originating from a plant in 2011 for reference (indicated by the small arrow). The ancient wood represent parts of a bronze age wells. All three samples are waterlogged, while the juvenile wood is situated within water. The measurement was performed using the larger 72 mm-resonator in order to visualise all three samples simultaneously.
The first row depicts the MT experiment using the TSE sequence. It is noticeable that the ancient wood differs strongly in signal intensity resulting from different T2 relaxation times. Whereas, the single tree rings and even the radial ray parenchyma can be seen very well in the sample providing the higher signal. The darker sample shows some ringing-like discrete structures, which seemingly are tracheary elements occurring periodically (cf. Lüttge et al., 2005).
For an unknown reason the old wood samples exhibit an extremely short T1 time (about 100 ms). This has to be considered choosing the flip angle. Here, the angle was optimised for the recent wood sample, i. e. small angle, in order to obtain a non-saturated signal at all.
An interpretation of the result might be based on the assumption that a suitable saturation pulse leads to an exchange of magnetisation between the bound protons, which interact with the dense packed wood ring cells and the free water protons. This may

* Courtesy of Fürhacker & Klatz GesbR, Weiz and Dr. Grabner, University of Natural Resources and Life Sciences, Vienna.

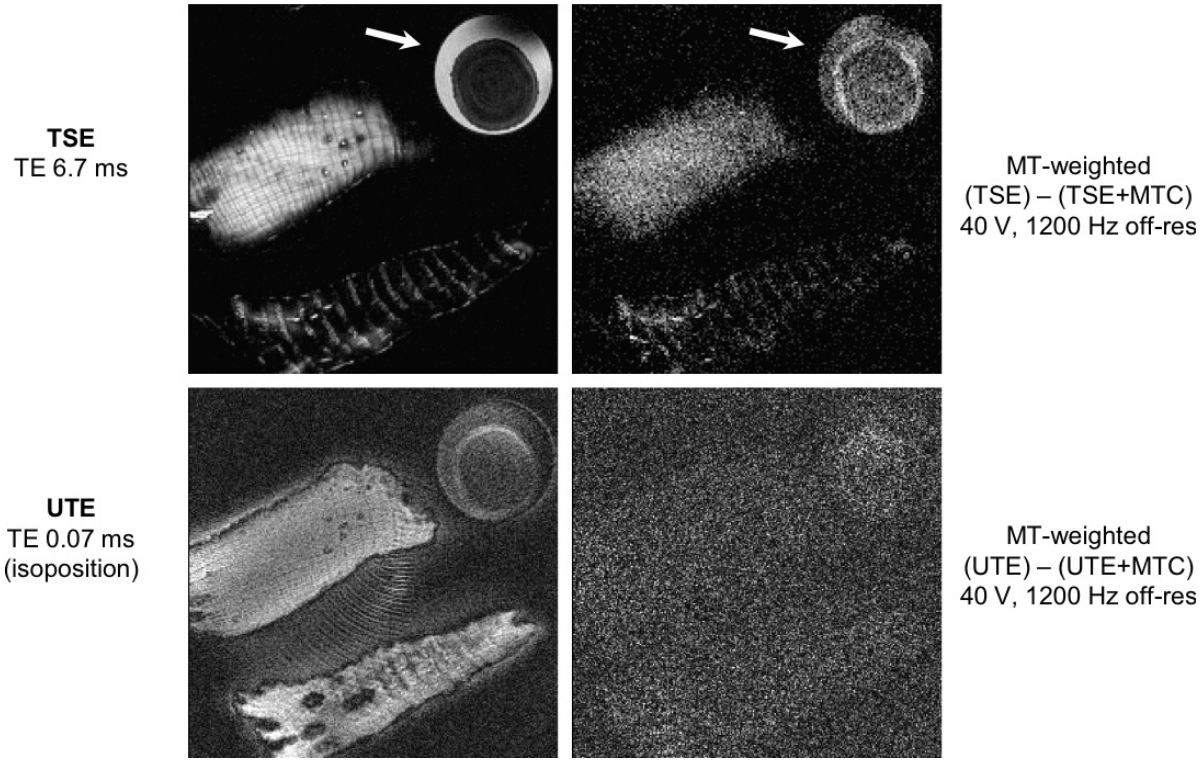

Figure 7.9.: A measurement of about 3500 years old wood samples (Courtesy of Fürhacker & Klatz GesbR, Weiz.) of unknown species together with a juvenile (2011) privet branch (*Ligustrum vulgare*) indicated by the small arrow. First row: TSE measurement and difference image (FOV: $50 \times 50\,\mathrm{mm}$, TR $= 4000\,\mathrm{ms}$, TE $= 6.7\,\mathrm{ms}$, BW $= 296\,\mathrm{Hz\,px^{-1}}$, Matrix: 192×192, turbo factor 5). Second row: UTE measurement and difference image (TR $= 366\,\mathrm{ms}$, TE $= 0.07\,\mathrm{ms}$, BW $= 296\,\mathrm{Hz\,px^{-1}}$, $\alpha = 3°$, $N = 256$, $N_{proj} = 40000$).

result in a specific MT contrast. The upper right image in Figure 7.9 shows the difference image obtained by a standard MT-weighting TSE sequence (1.2 kHz, 40 V). The MT contrast is relatively weak and provides a very low SNR. An enhanced contrast is conspicuous especially at the outer region of the juvenile wood where free water and wood are in direct contact.
The second row represents the equivalent UTE measurement. Here, both ancient wood samples provide high signal. Due to the heavy spin-density-weighting and the lower resolution, the contrast between different wood rings vanishes. Surprisingly, the difference image shows nearly no signal, but noise. This counter-intuitive result can be explained as follows: As discussed in Section 4.3, the pulse sequence is segmented into blocks of several profiles. By default this number of segment is set to 64, i. e. after every preparation pulse, 64 single profiles are acquired followed by another preparation pulse et cetera. Each preparation pulse leads to a certain saturation. Since each RF excitation is performed with small flip angles (in the order of 5°), it takes some flips until a steady state is achieved. During this time the reduced magnetisation is allowed to relax leading to a fully available magnetisation at the reached steady state and a loss of MT information. This effect is much more pronounced for samples with short T1s, which is true for the ancient wood samples. In addition, due to the small flip angle (optimisation for the juvenile wood) the full signal from the short-T1 tissue is suppressed leading to a reduced contrast in the difference image.
This hypothesis is also indicated by the experiments shown in Figure 7.10. Here, a MT measurements was performed using 64 segments (a), as default, and repeated using only 2 segments (b). The figure shows difference images at identical gray scaling of a ancient piece of wood and the juvenile privet branch. The MT pulses was chosen as follows: (a) 500 Hz off-resonant, 10 ms at 30 V, and (b) 500 Hz off-resonant, 10 ms at 5 V due to the increased cw power. It can be seen, that the MT contrast is enhanced using the reduced number of segments, i. e. more saturation pulses per profile excitation.
Hence, if short-T1 samples are investigated by MT contrast, the number of segments should be set to a small number. Since TR is adapted simultaneously, the total measurement time won't be prolonged significantly.

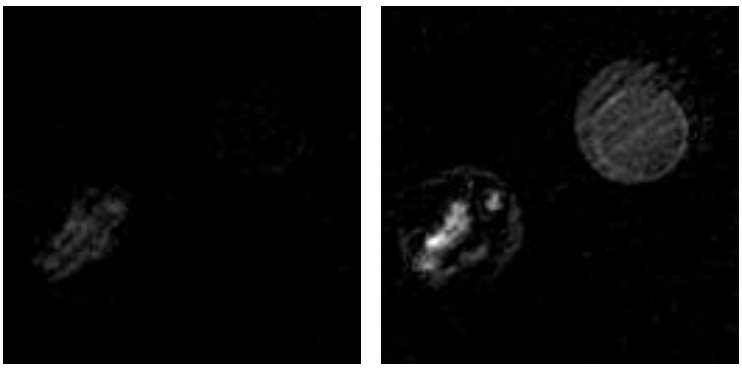

(a) (b)

Figure 7.10.: Influence of the parameter "segments" on the MT contrast using the 72 mm-resonator. Difference images at identical gray scaling of a ancient piece of wood and an juvenile privet branch at 64 segments (a) and 2 segments (b). MT-pulse parameters: (a) 500 Hz off-resonant, 10 ms at 30 V, and (b) 500 Hz off-resonant, 10 ms at 5 V. Other Parameters: (a): FOV: 44×44 mm, TR = 359 ms, TE = 0.07 ms, BW = 296 Hz px^{-1}, $\alpha = 15°$, $N = 128$, $N_{proj} = 4032$, 64 segments. (b): TR = 25 ms, 2 segments.

On the whole, the UTE sequence exhibit disadvantages compared to TSE in order to visualize wood rings. The TSE sequence offers clear advantages like sufficient contrast and a much higher spatial resolution. However, in some cases of very short-T2 materials the UTE sequence could be the only feasible tool.

Chapter 8

Summary

The purpose of this thesis was the quality control and optimisation of a UTE sequence for ultra-short detection times along with materials, which cannot be visualised by standard MRI pulse sequences. Another aim was the development of a UTE sequence featuring an additional magnetisation transfer signal-weighting. According to this, an existing (work-in-progress) sequence was modified in order to apply a preceding off-resonant saturation pulse. Moreover, it could be fundamentally improved by offering a much higher number of projections (and therefore better resolution) and the option for signal averaging. Additionally, a turbo spin echo sequence was supplemented with an analogous preparation pulse, that is fully adjustable. The sequences were specifically optimised for the use at a prototype micro-imaging insert to a high-field 7 T whole body scanner.

The imaging performance of both sequences was evaluated within the frame of quality control measurements. It could be shown that the UTE sequence, using very short detection times (< 1 ms), allows the visualisation of materials and biological tissues which are in-detectable by conventional spin echo imaging. The sequence allowed for imaging of biomaterials and plastics with very low T2 relaxation times. However, the possibility to contrast these materials selectively by the subtraction of differently T2-weighted images shows artefacts in general, which makes the image interpretation of more complex structures quite difficult.

The achievable spatial resolution of the UTE sequence depends explicitly on the sample type and different sequence parameters like the number of radial views and receiver bandwidth. Nevertheless, analyses of the modulation transfer function (MTF) show that structures significantly smaller than 1 mm do have modulations below 50 percent, which limits their detection. For soft tissue with T2s > 5 ms spin echo sequences, e. g. TSE, offer significant advantages concerning spatial resolution.

The option for MT contrast is validated on a plausible level. This was verified by semi-quantitative measurement on BSA-phantoms and comparison with a TSE sequence using standard MT. Furthermore, the influence of the "segments" parameter on the effective MT contrast was investigated. The MT model concept was supported in principle, e. g. by the image interpretation of a plant stem.

However, the currently available UTE imaging part of the pulse sequence exhibits also specific artefacts caused by an imperfect gradient timing performance. Thereby, signal frequency shifts lead to displacements of single profiles in k-space resulting in edge enhancements within the image. The delays depend dynamically on gradient strength, i. e. bandwidth, and detection time. These imperfections were minimised in good approximation by correction terms within the reconstruction process, which were obtained from systematic analyses of raw data.

Future works could follow up on these results. This includes the further correction of artefacts resulting from gradient performances. Here, the dynamic of delays as a function of bandwidth and detection time could be investigated in more detail leading to a preciser compensation. Also conceivable would be the addition of further preparation methods, like T1ρ (Berger, 2011) or on-resonant binomial pulses allowing the quantitative determination of the bound pool fraction (Soellinger et al., 2011).

Parts of this thesis have been (will be) published at the following conferences:

- C. Horn, V. Juras, S. Ropele, and A. Berg MR-microimaging on a 7T whole-body scanner featuring ultrashort detection times and magnetization transfer contrast, Proc. ISMRM 2012, Abstract No. 3582, Melbourne, Australia 05.-12.05 (2012)
- C. Horn, V. Juras A. Berg. Implementierung und QC von UTE-Sequenzen für MR-Microimaging an Gewebetypen und Kunststoffen mit sehr kurzen T2-Zeiten. Tagungsband der Jahrestagung der Deutschen-, Schweizerischen- und Österreichischen Gesellschaft für Medizinische Physik, Wien, Austria 29.09.-01.10.2011 (2011)

Appendix

Appendix

A.1. Listings “tse_mtc.cpp”

Listing A.1: Declaration of variables

```
222 //TESTING VARIABLES
223
224 //bool variables for selecting sequence type
225 bool MSat;
226
227 //variables for the MSat pulse
228 static long lRF_MSat_Duration;
229 static long lRF_MSat_Samples;
230 static long lRF_MSat_FlipAngle;
231 static long lRF_MSat_InitialPhase;
232
233 //Hard pulse Frequency Offset
234 static long lFrequency;
235
236
237 //Gaps between Real Time Events
238 static long lGapBefore_RF_MSat;
239
240 //static long lGapBetweenHardPulses;
241 static long lGapAfterHardPulse;
242
243
244 //Offset [us] between Spoil Gradient of the TSE Sequence and MSat pulse
245 static long lOffsetBeforeHardPulse = 80;
246
247 //Relative strength of Spoiler Gradient before Saturation Pulse
248 static long lSpoilBefStrength;
249
250 //Maximum Voltage / CW-Power Limit for the coil (security!)
251 static long lMaximumVoltageLimit;
252
253 static double dMaxiumCWPower;
254
255
256 long lHardPulsesTime;
```

```
257  double dEnergyOfHardPulses;
258
259  //TESTEND
```

Listing A.2: Declaration of real time events

```
352  //TESTING OBJECTS
353
354  //MSat pulse
355
356  //static sRF_PULSE_RECT          RF_MSat      ("RF_MSat");
357  //static sRF_PULSE_SINC          RF_MSat      ("RF_MSat");
358  static sRF_PULSE_GAUSS          RF_MSat      ("RF_MSat");
359
360  // Set Frequency and phase for RF pulse
361  static sFREQ_PHASE             PH_s_MSat    ("PH_s_MSat");
362  // Reset synthesizer back to base
363  static sFREQ_PHASE             PH_n_MSat    ("PH_n_MSat");
364
365
366  //TESTEND
```

Listing A.3: Calculation of the total time of the MT preparation block.

```
2834 //TESTING TIME
2835
2836   if(!MSat)
2837     {
2838     lHardPulsesTime = 0;
2839     }
2840
2841   if(MSat)
2842     {
2843     lHardPulsesTime = 0;
2844
2845     lHardPulsesTime = +lOffsetBeforeHardPulse
2846                       +lGapBefore_RF_MSat
2847                       +RF_MSat.getDuration()+lGapAfterHardPulse;
2848
2849     }
2850
2851 //TESTEND
```

Listing A.4: Calculation of the energy of the MT preparation block.

```
3070 //TESTING ENERGY
3071
3072   if(!MSat)
3073     {
3074     dEnergyOfHardPulses = 0;
3075     }
3076
3077   if(MSat)
3078     {
3079     dEnergyOfHardPulses = 0;
3080
3081     dEnergyOfHardPulses = RF_MSat.getPulseEnergyWs();
3082
3083     }
3084
3085   if (pdEnergyAllSBBs) *pdEnergyAllSBBs +=
3086   (MyTSEKernel.getEnergyPerRequest()-dEnergyBefore+dEnergyOfHardPulses)* MyTSEKernel.
         getRequestsPerMeasurement()*(pMrProt->repetitions()+1);
3087
```

```
3088    return bSuccess;
3089  }
3090
3091  //TESTEND
```

Listing A.5: Disabling of the standard-MT checkbox in the user interface.

```
4195    //pSeqLim->setMTC    (SEQ::OFF, SEQ::ON);
```

Listing A.6: Configuration of the parameter map which will be displayed in the “Special Card”.

```
4688  //TESTING PARAMETER MAP
4689
4690    BEGIN_PARAMETER_MAP(pSeqLim, 0, 0);
4691          COMPACT_BOOLS();
4692          COMPACT_SELECTIONS();
4693
4694            PARAM("Saturation Pulse", &MSat, true);
4695
4696      PARAM("Freq. Offset", "Hz", &lFrequency, 0, 3000, 10, 1500, "Frequeny Offset");
4697      PARAM("Duration", "us", &lRF_MSat_Duration, 10, 20000, 10, 10000, "Duration of the
             MSat Pulse");
4698
4699      PARAM("Flip Angle", "deg", &lRF_MSat_FlipAngle, 0, 1000, 10, 500, "Flip Angle of
             the MSat Pulse");
4700
4701      PARAM("Phase", "deg", &lRF_MSat_InitialPhase, -360, 360, 1, 0, "Initial Phase of
             the MSat Pulse");
4702
4703      PARAM("Gap before Pulse", "us", &lGapBefore_RF_MSat, 0, 50000, 1, 100, "Gap between
              Spoiler and MSat Pulse");
4704
4705      PARAM("Gap after Pulse", "us", &lGapAfterHardPulse, 0, 100000, 1, 50, "Gap after
             MSat Pulse");
4706
4707      PARAM("Spoiler Area", "\%\%", &lSpoilBefStrength, 0, 100, 1, 100, "Relative zeroth
             Moment (Area)of the Spoiler Gradient before the MSat Pulse");
4708
4709      PARAM("Max. Peak Voltage", "V", &lMaximumVoltageLimit, 0, 1000, 1, 70, "Maxiumum
             Voltage Limit for the coil");
4710
4711    //  PARAM("Max. CW-Power", "[W]", &dMaxiumCWPower, 0.0, 1000.0, 0.1, 5.0, "Max. cw
             Power");
4712
4713    END_PARAMETER_MAP;
4714
4715  //TESTEND
```

Listing A.7: Preparation of the real time events.

```
5744  //TESTING PULSE PREPARATION
5745
5746
5747  if(MSat)
5748    {
5749
5750    RF_MSat.setTypeExcitation          ();                          // Resets all moments to
           0 in Unit test
5751    RF_MSat.setDuration                (lRF_MSat_Duration);         // Most times are in
           microseconds
5752    RF_MSat.setFlipAngle               (lRF_MSat_FlipAngle);
5753    RF_MSat.setInitialPhase            (lRF_MSat_InitialPhase);     // Sets phase of pulse
           in rotating frame to 0 (+x)
```

```
5754    RF_MSat.setSamples                (lRF_MSat_Samples);        // Number of complex
            points in waveform
5755
5756            if(! RF_MSat.prepGauss(pMrProt,pSeqExpo)) return (RF_MSat.getNLSStatus());
                                                          //For Gauss Pulse Shape
5757
5758    }
5759  //TESTEND
```

Listing A.8: Calculation of the total time.

```
5765  //TESTING TIME
5766
5767    if(!MSat)
5768    {
5769    lHardPulsesTime = 0;
5770    }
5771
5772    if(MSat)
5773      {
5774      lHardPulsesTime = 0;
5775
5776      lHardPulsesTime = +lOffsetBeforeHardPulse
5777                        +lGapBefore_RF_MSat
5778                        +RF_MSat.getDuration()+lGapAfterHardPulse;
5779
5780      }
5781
5782  //TESTEND
```

Listing A.9: Prepare and Run Frequency/Phase objects and RF pulses.

```
8567  //TESTING RUN
8568
8569  //  Prepare and Run Frequency/Phase objects and RF pulses.
8570
8571  if(MSat)
8572    {
8573
8574    PH_s_MSat.prepSet  (asSLC[lSlice], RF_MSat);
8575    PH_n_MSat.prepNeg  (asSLC[lSlice], RF_MSat);
8576          PH_s_MSat.setFrequency ( lFrequency );
8577  //      PH_n_MSat.setFrequency ( 0L );
8578
8579
8580  //Running of the preparation block
8581
8582      lT=0;
8583
8584  //MSat pulse
8585
8586          if(RF_MSat.getTransmitterVoltage()>lMaximumVoltageLimit)
8587        {return SEQU_USER_ERROR_1;}
8588          else
8589           {
8590      lT+=lOffsetBeforeHardPulse+lGapBefore_RF_MSat;
8591
8592      PH_s_MSat.setStartTime(lT);
8593      PH_s_MSat.run();
8594      RF_MSat.setStartTime(lT);
8595      RF_MSat.run();
8596
8597      lT+=RF_MSat.getDuration();
8598
8599      PH_n_MSat.setStartTime(lT);
```

```
8600        PH_n_MSat.run();
8601                            }
8602      }
8603
8604    //TESTEND
```

A.2. M-file: Inverse PSF to MTF

Listing A.10: Matlab m-file: Reads ASCII-formatted line profiles and calculates the MTF and corresponding spatial resolution.

```
1   %% Auswertung von Profilen einer PSF. Kalkulation der MTF als FT der PSF
2   %% Mehrere Profile werden eingelesen und jeweils das Aufloesungsvermoegen
3   %% bei einer Modulation von 50% errechnet.
4   %% Ausgabe von Mittelwert und Standardabweichung.
5
6
7   clear all;
8   % load raw_radial2.dat;
9   load raw_normal2.dat;
10
11  % [Z,S]=size(raw_radial2);
12  [Z,S]=size(raw_normal2);
13
14  resr=zeros(1,S-1);
15
16  for i=1:S-1% Fuer jedes Profil
17
18  % fr=raw_radial2(:,i+1);
19  % xr=raw_radial2(:,1);
20
21  fr=raw_normal2(:,i+1);
22  xr=raw_normal2(:,1);
23
24  N=512;% N-Punkt DFT
25
26  Fr=abs(fft(fr,N));% MTF durch FFT
27  Fr=Fr/Fr(1);% Normierung
28
29
30  l_r=abs(max(xr))+abs(min(xr));% Laenge des Profils in mm
31  np_r=length(xr);% Anzahl der Samples
32
33  w_min=1/l;% Minimale Ortsfrequenz
34  w_max=np/(2*l);% Maximale Ortsfrequenz (Nyquist Frequenz)
35
36  W_r=linspace(w_min_r,w_max_r,N);% Ortsfrequenzspektrum fuer Plot
37
38  plot(W_r,Fr,'b'),...
39      axis([w_min_r 2 0 1.8]),...
40      xlabel('spatial frequency [mm^{-1}]'),...
41      ylabel('modulation'),...
42  %     legend('radial MTF','normal MTF')
43  waitforbuttonpress;
44
45
46  [I, Zeiler]= min(abs(Fr(:)-0.5));
47
48  resr(i)=1/W_r(Zeiler);% Aufloesungsvermoegen als Kehrwert der Frequenz
49
50  end
51
52  res_mean=mean(resr);% Bildung von Mittelwert und
```

```
53  res_stdev=std(resr);% Standardabweichung
54
55  % Ausgabe am Bildschirm
56  str = ['Das Aufloesungsvermoegen bei Modulation 50 Prozent liegt bei'];
57  disp(str)
58  str = ['(', num2str(res_mean),' +- ', num2str(res_stdev) ') mm.'];
59  disp(str)
60  str = ['(Auswertung von ' , num2str(S-1),' Profilen.)'];
61  disp(str)
```

A.3. M-file: Analysis of Edge Enhancement

Listing A.11: (Exemplary) Matlab m-file: Reads ASCII-formatted line profile for several gradient delays and finds the particular relative edge enhancement. The optimal gradient delay time is determined.

```
1   % Programm sucht nach dem optimalen Wert fuer die Gradienten Delays.
2   % Es werden 15 Profile eingelesen, ein Wert fuer die Kante des Objekts
3   % definiert und die relative Kantenanhebung im Verhaeltnis zum
4   % durchschnittlichen Plateauniveau (homogenes Wasserphantom) berechnet. Die
5   % optimale Gradienten Verzoegerung wird durch lineare Interpolation bei
6   % Kantenanhebung gleich Null ausgewertet.
7   % Darstellung der Ergebnisse im Plot und am Bildschirm.
8
9
10  clear all;
11
12  R=zeros(15,3);
13  edge_enh=zeros(8,2);
14
15  j=0;
16  FOV=125;
17  Mtx=128;
18  BW=558;
19
20  for i= 0:2:14 %
21
22      j=j+1;
23
24      % lade Datensatz
25      filename=num2str(i);
26      A=load([filename '.dat']);
27      x=A(:,1);
28      x=x*FOV/Mtx/5;
29
30      if j==1
31          i=-0.760;
32          i_min=i;
33      end
34
35      profile=A(:,2);
36
37      plateau=profile(end-15:end); % Definition des Plateaus
38      plat_mean=mean(plateau);    % Mittel ueber die letzten 7 Werte
39      plat_std=std(plateau);
40
41      kante_pos=15;                % Definition der Kante
42      kante=profile(kante_pos);   % Wert in der 8. Zeile
43
44      rel_edge_enh=(kante-plat_mean)/plat_mean;
45
46      edge_enh(j,1)=i;            % Speichern in Array
```

```
47      edge_enh(j,2)=rel_edge_enh; % relative Kantenanhebung
48
49
50      kante_plot_x=[x(kante_pos),x(kante_pos)];   % Kante im Plot
51      kante_plot_y=[plat_mean,kante];
52
53      plot(x,profile,'-x',...
54          x,plat_mean*ones(1,length(x)),':k',...
55          kante_plot_x,kante_plot_y)
56              xlabel('distance [mm]')
57              ylabel('signal intensity [a.u.]')
58              legend(['profile @ ' num2str(i) ' us'],...
59                  'mean plateau niveau',...
60                  'edge enhancement', 'Location','SouthEast');
61
62   %    pause(0.5);
63     waitforbuttonpress;
64
65
66  end
67
68  p = interp1(edge_enh(:,2),edge_enh(:,1),0);      % Nullstelle durch
69                                                   % Lineare Interpolation
70  delta_p=p-i_min;
71  nulldurchgang_x=[p,p];  % Nullstelle im Plot
72  nulldurchgang_y=[-3,3];
73
74  plot(edge_enh(:,1),edge_enh(:,2),'-xr',...
75      nulldurchgang_x,nulldurchgang_y,':k',...
76      edge_enh(:,1),zeros(j),':k')
77          axis([i_min i -1.5 2])
78          xlabel('gradient delay [us]')
79          ylabel('relative edge enhancement [-]')
80          legend('edge enhancement','zero')
81          text(p+1,0.25,[num2str(p) ' us']);
82
83  % Bildschirmausgabe
84  str1 = ['Gradient Delay = ',num2str(p), ' us (delta_t = ', num2str(delta_p), ', BW = ',
        num2str(BW),' Hz/px).'];
85  disp(str1)
86  % Ende
```

A.4. Spin-spin Relaxation Time of HMA

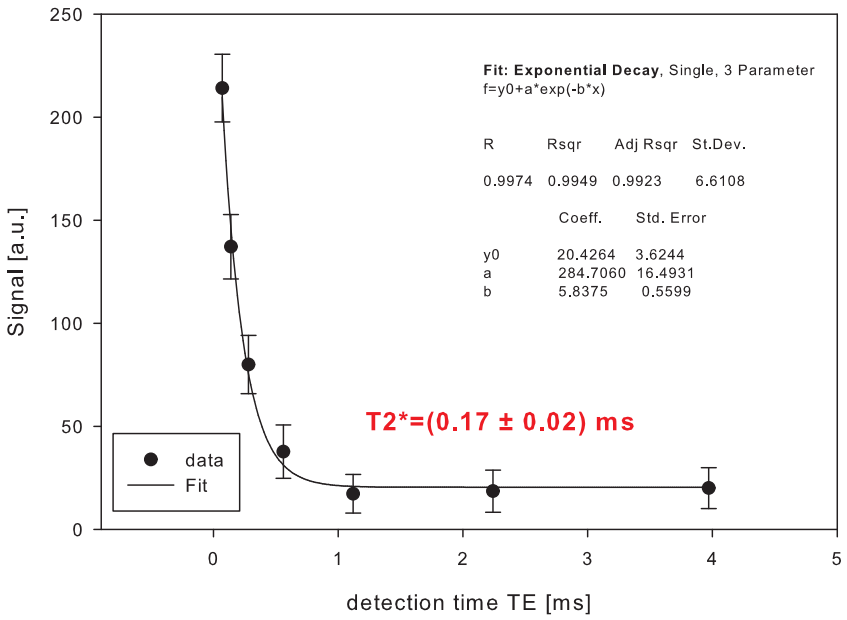

Figure A1.: Spin-spin relaxation time T2 of hot melt adhesive (HMA). Signal intensity as a function of detection time TE. The measurement data is fitted by an exponential decay function. The resulting fit parameter gives the decay constant T2.

Bibliography

Allison, W. (2006). *Fundamental Physics for Probing and Imaging*. Oxford University Press, New York.

Badurek, G. (2010). *Biological and medical applications of nuclear physics II*. Script, TU Wien.

Bakshi, R., Ariyaratana, S., Benedict, R. H., and Jacobs, L. (2001). Fluid-attenuated inversion recovery magnetic resonance imaging detects cortical and juxtacortical multiple sclerosis lesions. *Archives of neurology*, 58(5):742–8.

Berg, A., Potthast, A., and Starewicz, P. (2010). MR-Microscopy on a Human 7T-Scanner. In *ISMRM/ESMRMB Annual Meeting*, Stockholm.

Berg, A., Potthast, A., Starewicz, P., Domayer, S., and Hofstaetter, J. (2011). MR-microscopy on a human 7T MR-scanner: methodology and application to medial osteoarthritic samples of the knee (EPOS #2914). In *ECR European Congress of Radiology 2011*, Vienna.

Berger, S. (2011). *T1rho Pulse Sequence Development*. PhD thesis, Medical University of Vienna.

Bernstein, M., King, K., and Xiaohong, Z. (2004). *Handbook of MRI Pulse Sequences*. Elsevier Academic Press, Burlington.

Bloembergen, N., Purcell, E., and Pound, R. (1948). Relaxation Effects in Nuclear Magnetic Resonance Absorption. *Physical Review*, 73(7):679–712.

Boada, F. E., Christensen, J. D., Gillen, J. S., and Thulborn, K. R. (1997). Three-dimensional projection imaging with half the number of projections. *Magnetic resonance in medicine*, 37(3):470–7.

Boreman, G. D. (2001). *Modulation transfer function in optical and electro-optical systems*. SPIE Press.

Brix, G., Kolem, H., Nitz, W. R., Bock, M., and Huppertz, A. (2008). Basics of Magnetic Resonance Imaging and Magnetic Resonance Spectroscopy. In Reiser, M., Semmler, W., and Hricak, H., editors, *Magnetic Resonance Tomography*, pages 3–167. Springer Berlin Heidelberg.

Callaghan, P. T. (1991). *Principles of Nuclear Magnetic Resonance Microscopy*. Oxford University Press, New York.

Ceckler, T., Maneval, J., and Melkowits, B. (2001). Modeling magnetization transfer using a three-pool model and physically meaningful constraints on the fitting parameters. *Journal of magnetic resonance*, 151(1):9–27.

de Graaf, R. A. (2007). *In Vivo NMR Spectroscopy: Principles and Techniques*. John Wiley and Sons.

Delfaut, E. M., Beltran, J., Johnson, G., Rousseau, J., Marchandise, X., and Cotten, A. (1999). Fat suppression in MR imaging: techniques and pitfalls. *Radiographics*, 19(2):373–82.

Du, J., Pak, B. C., Znamirowski, R., Statum, S., Takahashi, A., Chung, C. B., and Bydder, G. M. (2009). Magic angle effect in magnetic resonance imaging of the Achilles tendon and enthesis. *Magnetic resonance imaging*, 27(4):557–64.

Engelhardt, R. T. and Johnson, G. A. (1996). T1rho relaxation and its application to MR histology. *Magnetic resonance in medicine*, 35(5):781–6.

Gatehouse, P. and Bydder, G. (2003). Magnetic Resonance Imaging of Short T2 Components in Tissue. *Clinical Radiology*, 58(1):1–19.

Glover, G. H. and Pauly, J. M. (1992). Projection reconstruction techniques for reduction of motion effects in MRI. *Magnetic resonance in medicine*, 28(2):275–89.

Haacke, E. M., Brown, R. W., Thompson, M. R., and Venkatesan, R. (1999). *Magnetic Resonance Imaging - Physical Principles and Sequence Design*. John Wiley and Sons, New York, 1st edition.

Hall-Craggs, M. A. (2004). Ultrashort echo time (UTE) MRI of the spine in thalassaemia. *British Journal of Radiology*, 77(914):104–110.

Henkelman, R. M., Huang, X., Xiang, Q.-S., Stanisz, G. J., Swanson, S. D., and Bronskill, M. J. (1993). Quantitative interpretation of magnetization transfer. *Magnetic Resonance in Medicine*, 29(6):759–766.

Henkelman, R. M., Stanisz, G. J., and Graham, S. J. (2001). Magnetization transfer in MRI: a review. *NMR in biomedicine*, 14(2):57–64.

Kuhn, W. (1990). NMR Microscopy—Fundamentals, Limits and Possible Applications. *Angewandte Chemie International Edition in English*, 29(1):1–19.

Kuperman, V. (2000). *Magnetic resonance imaging: physical principles and applications*. Academic Press.

Lüttge, U., Kluge, M., and Bauer, G. (2005). *Botanik*. Wiley-VCH, 5th edition.

McRobbie, D., Moore, E., and Graves, M. (2007). *MRI from picture to proton*. Cambridge University Press.

MedUniWien (2008). MUW schreibt Medizingeschichte: Erstes 7-Tesla Bild in Österreich. `http://www.meduniwien.ac.at/7tesla/news/muw-schreibt-medizingeschichte-erstes-7-tesla-bild-in-oesterreich/`, Retrieved: October, 17, 2011.

Mehta, R. C. M., Pike, G. B. M., and Enzmann, D. R. M. (1996). Magnetization Transfer Magnetic Resonance Imaging: A Clinical Review. *Topics in Magnetic Resonance Imaging*, 8(4):214–230.

Nielles-Vallespin, S. (2004). *Development and Optimisation of Radial Techniques for Sodium Magnetic Resonance Imaging*. PhD thesis, Ruprecht-Karls-Universität Heidelberg.

Nielles-Vallespin, S., Speier, P., Zenge, M., Kannengiesser, S., and Shah, S. (2009). Applications Guide: CV_3DRAD_400C. Version 400C / Patch 2.0. Siemens Health Care.

Nielles-Vallespin, S., Weber, M.-A., Bock, M., Bongers, A., Speier, P., Combs, S. E., Wöhrle, J., Lehmann-Horn, F., Essig, M., and Schad, L. R. (2007). 3D radial projection technique with ultrashort echo times for sodium MRI: clinical applications in human brain and skeletal muscle. *Magnetic resonance in medicine*, 57(1):74–81.

Nobelprize.org (2003). The Nobel Prize in Physiology or Medicine 2003. `http://www.nobelprize.org/nobel_prizes/medicine/laureates/2003/`, Retrieved: October, 19, 2011.

Nunley, J. A. (2009). *Achilles Tendon - Treatment and Rehabilitation*. Springer-Verlag, New York.

Oesterle, C., Markl, M., Strecker, R., Kraemer, F. M., and Hennig, J. (1999). Spiral reconstruction by regridding to a large rectilinear matrix: a practical solution for routine systems. *Journal of magnetic resonance imaging*, 10(1):84–92.

Parish, T. B., Fieno, D. S., Fitzgerald, S. W., and Judd, R. M. (1997). Theoretical basis for sodium and potassium MRI of the human heart at 1.5 T. *Magnetic Resonance in Medicine*, 38(4):653–661.

Peters, D. C., Derbyshire, J. A., and McVeigh, E. R. (2003). Centering the projection reconstruction trajectory: reducing gradient delay errors. *Magnetic resonance in medicine*, 50(1):1–6.

Peters, D. C., Korosec, F. R., Grist, T. M., Block, W. F., Holden, J. E., Vigen, K. K., and Mistretta, C. A. (2000). Undersampled projection reconstruction applied to MR angiography. *Magnetic resonance in medicine*, 43(1):91–101.

Rapid Biomedical GmbH (2007). Specification and Operation Instructions - 1H NMR Volume Coil V-HQ-070-00748 V01. Manual.

Rapid Biomedical GmbH (2008). Gebrauchsanweisung - MR-Volumenspule V-HLS-070-00838-001 für SIEMENS 7T MR-Systeme. Manual.

Redpath, T. W. (1998). Signal-to-noise ratio in MRI. *The British journal of radiology*, 71(847):704–7.

Robson, M., Gatehouse, P., Bydder, M., and Bydder, G. (2003). Magnetic Resonance: An Introduction to Ultrashort TE (UTE) Imaging. *Journal of Computer Assisted Tomography*, 27(6):825–846.

Robson, M. D., Benjamin, M., Gishen, P., and Bydder, G. M. (2004). Magnetic resonance imaging of the Achilles tendon using ultrashort TE (UTE) pulse sequences. *Clinical radiology*, 59(8):727–35.

Ropele, S., Enzinger, C., Seifert, T., and Fazekas, F. (2006). Measurement of short and ultrashort T2 components using progressive binomial RF saturation. *Magnetic resonance in medicine*, 56(2):265–71.

Scheffler, K. and Hennig, J. (1998). Reduced circular field-of-view imaging. *Magnetic resonance in medicine*, 40(3):474–80.

Schomberg, H. and Timmer, J. (1995). The gridding method for image reconstruction by Fourier transformation. *IEEE transactions on medical imaging*, 14(3):596–607.

Siemens AG Healthcare (2002). System Manual - Magnetom 7T Operating Instructions.

Siemens AG Healthcare (2010). Switching of RRI Gradient Coil - Operator Manual.

Smith, T. B. and Nayak, K. S. (2010). MRI artifacts and correction strategies. *Imaging in Medicine*, 2(4):445–457.

Soellinger, M., Langkammer, C., Seifert-Held, T., Fazekas, F., and Ropele, S. (2011). Fast bound pool fraction mapping using stimulated echoes. *Magnetic resonance in medicine*, 66(3):717–24.

Staff, E. and Kuijlaars, A. (1997). Distributing many points on a sphere. *The Mathematical Intelligencer*, 19(1):5–11.

Taylor, R. E. and Aitken, A. J. (1997). *Chronometric dating in archaeology (Advances in Archaeological and Museum Science)*. Springer, 1st edition.

Tyler, D. J., Robson, M. D., Henkelman, R. M., Young, I. R., and Bydder, G. M. (2007). Magnetic resonance imaging with ultrashort TE (UTE) PULSE sequences: technical considerations. *Journal of magnetic resonance imaging*, 25(2):279–89.

Vlaardingerbroek, M. T. and den Boer, J. A. (2003). *Magnetic resonance imaging: theory and practice*. Springer.

Wikipedia (2012). Anterior cruciate ligament. `en.wikipedia.org/wiki/Anterior_cruciate_ligament`, Retrieved: February, 02, 2012.

Wolff, S. D. and Balaban, R. S. (1989). Magnetization transfer contrast (MTC) and tissue water proton relaxation in vivo. *Magnetic Resonance in Medicine*, 10(1):135–144.

Zientara, G. (1995). Fast Imaging Techniques for Interventional MRI. *Interventional MR*, Ch 2:25–52.

Acknowledgements

First of all I would like to thank my supervisor, Prof. Andreas Berg, who has patiently supported me throughout my thesis with his knowledge, help and advice.

My special thanks go to Prof. Gerald Badurek for his supervision. Not least because he also aroused my interest for MRI with his unique talent to illustrate quite complex mechanisms in a simple way.

Also I would like to show my gratitude to Prof. Ewald Moser and Prof. Siegfried Trattnig, heads of the MR Centre of Excellence, for making my experimental work possible.

I am indebted to all of my colleagues, especially Joachim Friske, Vladimir Juras, Sebastian Leder, Stefan Berger and Bernhard Strasser.

This thesis would not have been possible without the WIP-UTE package source code, which was offered by Siemens (Vladimir Jellus and Lars Lauer) within the "VIACLIC" research programme (Vienna Spots of Excellence des Wiener Wissenschafts- und Technologie-Fonds (WWTF) – Vienna Advanced Imaging Center, Siegfried Trattnig and Gert Reiter). Many thanks for that.

Moreover, I am grateful to Prof. Stefan Ropele of the Medical University of Graz. He has made available his reference samples and experience regarding magnetisation transfer contrast.

Last but not least, I owe my deepest gratitude to my girlfriend Anika, who always remain steadfastly at my side. Danke!

Financial support for project material, conference visits and stipend money was offered to me within the §26 project of the Medical University of Vienna, which was funded by the "Hochschuljubiläumsfonds der Stadt Wien": Project number.: H-247/2001 8 (A. Berg).